International Review of Mechanical Engineering (IREME)

Editor-In-Chief:

Prof. Ethirajan Rathakrishnan
Department of Aerospace Engineering
Indian Institute of Technology
Kanpur - INDIA

Editorial Board:

Jeongmin Ahn	(U.S.A.)	**David Hui**	(U.S.A.)
Jan Awrejcewicz	(Poland)	**Heuy-Dong Kim**	(Korea)
Ali Cemal Benim	(Germany)	**Marta Kurutz**	(Hungary)
Stjepan Bogdan	(Croatia)	**Herbert A. Mang**	(Austria)
Andrè Bontemps	(France)	**Josua P. Meyer**	(South Africa)
Felix Chernousko	(Russia)	**Bijan Mohammadi**	(France)
Kim Choon Ng	(Singapore)	**Hans Müller-Steinhagen**	(Germany)
Olga V. Egorova	(Russia)	**Eugenio Oñate**	(Spain)
Horacio Espinosa	(U.S.A)	**Pradipta Kumar Panigrahi**	(India)
Izhak Etsion	(Israel)	**Constantine Rakopoulos**	(Greece)
Alexander N. Evgrafov	(Russia)	**Raul Suarez**	(Spain)
Torsten Fransson	(Sweden)	**David J. Timoney**	(Ireland)
Michael I. Friswell	(U.K.)	**George Tsatsaronis**	(Germany)
Nesreen Ghaddar	(Lebanon)	**Sharif Ullah**	(Japan)
Adriana Greco	(Italy)	**Hiroshi Yabuno**	(Japan)
Carl T. Herakovich	(U.S.A.)	**Tim S. Zhao**	(Hong Kong)
M. G. Higazy	(Egypt)		

The *International Review of Mechanical Engineering (IREME)* is a publication of the **Praise Worthy Prize S.r.l.**.
The Review is published monthly, appearing on the last day of every month.

Published and Printed in Italy by **Praise Worthy Prize S.r.l.**, Naples, October 31, 2018.

Copyright © 2018 Praise Worthy Prize S.r.l. - All rights reserved.

This journal and the individual contributions contained in it are protected under copyright by **Praise Worthy Prize S.r.l.** and the following terms and conditions apply to their use:
Single photocopies of single articles may be made for personal use as allowed by national copyright laws.
Permission of the Publisher and payment of a fee is required for all other photocopying, including multiple or systematic copying, copying for advertising or promotional purposes, resale and all forms of document delivery. Permission may be sought directly from **Praise Worthy Prize S.r.l.** at the e-mail address:
administration@praiseworthyprize.com

Permission of the Publisher is required to store or use electronically any material contained in this journal, including any article or part of an article. Except as outlined above, no part of this publication may be reproduced, stored in a retrieval system or transmitted in any form or by any means, electronic, mechanical, photocopying, recording or otherwise, without prior written permission of the Publisher. E-mail address permission request:
administration@praiseworthyprize.com

Responsibility for the contents rests upon the authors and not upon the **Praise Worthy Prize S.r.l.**.
Statement and opinions expressed in the articles and communications are those of the individual contributors and not the statements and opinions of **Praise Worthy Prize S.r.l.**. **Praise Worthy Prize S.r.l.** assumes no responsibility or liability for any damage or injury to persons or property arising out of the use of any materials, instructions, methods or ideas contained herein.
Praise Worthy Prize S.r.l. expressly disclaims any implied warranties of merchantability or fitness for a particular purpose. If expert assistance is required, the service of a competent professional person should be sought.

International Review of Mechanical Engineering (I.RE.M.E.), Vol. 12, N. 10
ISSN 1970 - 8734
October 2018

Condensation Heat Transfer Characteristics of Hydrofluoroolefin Refrigerant R1234YF as an R134a Alternative

Talaat A. Ibrahim[1, 2], M. A. M. Hassan[1]

Abstract – *This study conducts an experimental investigation to determine the condensation heat transfer characteristics of hydrofluoroolefin R1234yf and R134a on horizontal smooth and finned tubes. The experiments are conducted at a saturation temperature of 39°C with variable water cooling temperatures and velocities. Additionally, the effects of different fin geometries are investigated. The predicted condensation heat transfer coefficients on the smooth tube are lower than the experimental coefficients by 2.8–14.2% for R134a and 13.8–20.7% forR1234yf. The experimental results demonstrate that the heat flux increases with a decrease in the fin height or an increase in the fin pitch and thickness. Additionally, the heat flux increases as the water velocity increases or the water inlet temperature decreases. The results also show that the tube with the largest fin pitch, largest fin thickness, and smallest fin height provides the highest condensation heat flux. The condensation heat transfer coefficients of R1234yf are slightly higher than those of R134a for all of the experiments. Thus, this study concludes that R1234yf is a potentially environmentally-friendly alternative to R134a for condensation heat transfer applications.* ***Copyright © 2018 Praise Worthy Prize S.r.l. - All rights reserved.***

Keywords: *R134a Condensation, R1234yf Condensation, R134a Alternatives, R1234yf, Horizontal Finned Tubes*

Nomenclature

A	Surface area	m^2
C	Specific heat at a constant pressure	kJ/(kg K)
d	Diameter	m
g	Gravitational acceleration	m/s^2
h	Heat transfer coefficient	$W/(m^2K)$
h_{fg}	Heat of evaporation	kJ/kg
H	Fin height	mm
HTC	Heat Transfer Coefficient	$W/(m^2K)$
k	Thermal conductivity	W/(mK)
L	Effective tube length	m
LMTD	Logarithmic Mean Temperature Difference	K
$\dot{m}$	Mass flow rate	kg/s
p	Pressure	kPa
q	Heat flux	W/m^2
Q	Rate of heat transfer	W
r	Pipe radius	mm
S	Fin pitch	mm
t	Fin thickness	mm
T	Temperature	°C
U	Overall heat transfer coefficient	$W/(m^2K)$
v	Velocity	m/s
Dimensionless		
HTER	Heat Transfer Enhancement Ratio	
N	Number of fins	
Nu	Nusselt number	
Pr	Prandtl number	
Re	Reynolds number	

Greek letters		
Δ	Difference	-
μ	Dynamic viscosity	kg/(m s)
P	Density	kg/m^3
Subscripts		
b	Fin base	
f	Fin	
i	Inside	
l	Liquid	
o	Outside	
s	Surface	
sat	Saturation	
t	Total	
uf	Un-finned	
w	Water	
wi	Water at the inlet	
wo	Water at the outlet	

I. Introduction

Industrial refrigeration and HVAC systems have recently gained attention of researchers and continue to be a topic of interest in the research community. Central air-conditioning systems and indoor air quality are essential issues in modern society, especially when compared to the vast amounts of air pollution produced in the 19th century. In refrigeration systems, heat exchangers are a main component, and thus, the improvement of the heat exchanger is necessary to

https://doi.org/10.15866/ireme.v12i10.16096

enhance the performance of the component and the overall system. To attain increased performance, accurate data of the condensation heat transfer characteristics are essential for designing the condensers for refrigeration systems [1]. Several previous works have studied the condensation heat transfer characteristics of various refrigerants. Seara et al. [2] conducted experimental and theoretical studies to investigate the condensation characteristics of an ammonia–water mixture on a horizontal smooth tube. The theoretical results showed that the mass transfer of the ammonia vapor phase had a pronounced effect on the heat and mass transfer coefficients, thus, impacting the overall condensation heat transfer coefficients (HTCs).

Jung et al. [3] quantified the condensation HTCs for various flammable refrigerants on a smooth tube with an outside diameter of 19 mm at a condensation temperature of 39°C. The results for the flammable refrigerants did not indicate any unusual behaviors. The authors reported increased HTCs for R32 and dimethyl ether of approximately28–44% when compared to R22owing to their favorable thermophysical properties; propylene and butane indicated similar HTCs to those of R22. However, propane and iso-butane presented lower HTCs than those ofR22 by 9%. Generally, fins are implemented outside of the condenser tubes to improve the rate of heat transfer.

Kumar et al. [4] experimentally investigated the HTC during the condensation of steam over a smooth tube.

The authors reported data for two types of configurations: spine integral-fin tubes and circular integral-fin tubes. The spine integral-fin tubes and circular integral-fin tubes enhanced the condensation HTCs by factors of 3.2 and 2.5, respectively.

Additionally, Kumar et al. [5] predicted the condensation HTCs of water and R134a on single horizontal fin tubes at different operating parameters. Further research was conducted by Kumar et al. [6] to experimentally investigate the effects on the R134a condensation HTCs generated by different fin configurations and different types of horizontal circular integral-fin tubes. The results revealed that the integral-fin tube with a fin height of 0.45mm provided the greatest HTC improvement when compared to the HTCs obtained from the Nusselt model for a smooth tube. Briggs and Rose [7] modeled the condensation heat transfer on horizontal integral fin tubes to predict the optimum fin thickness, height, and spacing. The study indicated that the best fin thickness is dependent upon the fluid and fin material. Recently, Reif et al. [8] studied the condensation HTCs of pure components (non-refrigerant materials) on horizontal low-finned tubes. The authors found that the outer condensation HTCs of the low-finned tubes were 3-8 times higher than that of a smooth tube. They attributed the improvement of the HTCs to two factors: (1) the increased surface area of the finned tubes compared to the smooth tubes and (2) the drainage of the condensate on the low-finned tubes due to a surface tension induced pressure gradient. In addition, they developed a theoretical model to calculate the outer condensation HTCs using dimensionless numbers for the non-refrigerant components. Further research was conducted pertaining to the condensation on horizontal low-finned tubes to gain additional understanding. Kang et al. [9] investigated an experimental correlation for falling film condensation with an uncertainty of ±5% during the condensation of R134a on low-finned and Turbo-C tubes. The heat transfer of the Turbo-C tubes demonstrated an HTC increase of 3–4 times that of the theoretical Nusselt number correlation; moreover, this increase was more effective in the high-wall subcooling temperature region.

Buechner et al. [10] studied the condensation of two binary mixtures, n-pentane/iso-octane and isopropanol/water, with free convection on a horizontal tube. The authors developed a model and verified their findings through comparisons with a common model found in literature and their own experimental results; deviations of less than ±20% were found from these comparisons. The condensation HTCs over tube bundles have also been experimentally reported. Karlsson and Vamling [11] conducted detailed calculations pertaining to the condensation of a binary zeotropic mixture over a tube bank. The authors studied the combined effects of the mass transfer resistances in the liquid and vapor phases. They found that the heat fluxes reduced by 20% and 50% due to a decrease in the vapor phase resistance and an increase in the vapor velocity, respectively. These effects were attributed to the mass transfer resistance of the heavy volatile component and a temperature reduction of the phase interface. Similarly, Honda et al. [12]-[14] studied the effects generated by different tube geometries on the condensation HTCs in a tube bundle.

This study found that the R123 mixture has significantly lower HTC compared to that of the R134a mixture for all of the tube geometries. These studies concluded that the difference was pronounced for lower temperatures and lower mass velocities. The authors attributed these behaviors to the diffusive transport resistance closest to the gas-liquid interface in the vapor film. The refrigerants mentioned in the previous discussion have some undesirable characteristics, one of which is the greenhouse effect. These adverse effects have been addressed through the use of alternative refrigerants in conventional vapor-compression systems.

Brown et al. [15] investigated the thermal properties, heat transfer performance, and pressure drop performance of hydrofluoroolefins (HFOs), which have been used in chemistry applications. HFOs are much like traditional hydrofluorocarbons (HFCs), as they are composed of hydrogen, fluorine, and carbon. R1234yf has recently become the refrigerant of choice for car manufacturers, as nearly fifty vehicle models have adopted this new refrigerant [16]. Moreover, HFOs are found in a number of applications. HFO-1234yf (R1234yf) has been chosen to replace R134a in refrigeration and heat pump technology. HFO-1234ze(E) and HFO-1233zd(E) are used in chillers [17], and HFO-1336mzz has been suggested for use in high-temperature heat pump applications [18]. Unlike R134a, R1234yf has desirable environmental traits owing to its reduced impact on global warming. This is a common feature of other HFOs, a number of which have been integrated into technology over the past 100 years. The global warming contribution of HFOs is not greater than that of CO_2, mainly due to the short lifetime of HFOs, which ranges within a few weeks. The condensation HTCs and pressure drop of R1234yf were explored within a minichannel [19]. The study proved that both R134a and R1234yf have comparable HTCs by condensation for lower quantities of vapor and single phase liquid as well. Park et al. [20] investigated the condensation HTCs of HFC134a andR1234yf on three tube's configurations.

Those were: plain, low-finned, and Turbo-C tubes. They concluded similar condensation HTCs for both R1234yf and R134a for all experiments. Recently, same authors developed the performances of R1234yf, R1234ze, and R134a in an aluminum multi-minichannel heat sink [21]. The above review reveals that there is a shortage of information pertaining to the condensation heat transfer of R1234yf on the outside of a tube.

Therefore, the current work focuses on the following three objectives: (1) quantifying the condensation HTC of R1234yf on horizontal smooth and finned tubes over a wide range of operating parameters, (2) investigating the effects of the coolant temperature, velocity, and tube geometry (fin thickness, pitch, and height) on the condensation heat transfer characteristics of R1234yf, and (3) comparing the condensation heat transfer characteristics of R1234yf and R134a. To achieve these objectives, an experimental test facility was constructed, and the required measuring devices were installed. The experiments were conducted using two refrigerants, R1234yf and R134a, at a saturation temperature of 39°C with variable water cooling temperatures and velocities.

II. Experimental Facility and Data Reduction

II.1. Experimental Facility

An experimental test facility that was constructed to evaluate the condensation heat transfer characteristics on horizontal smooth and finned tubes is presented in Fig. 1.

However, a photo of this test rig is provided in Fig. 2 [22]. The test rig consists of two main paths (the refrigerant and cooling water paths) and the measuring devices. The refrigerant path consists of a stainless steel boiler and a test section, which represents the water-cooled condenser. The boiler is equipped with three 1.6kW electric heaters that are controlled using three 2.0kVA variable voltage devices. For the purposes of charging and evacuation, two valves are constructed on the boiler, represented by V_1 and V_2 in Fig. 1. In order to prevent back flow, a non-return valve (V_4) is installed on the refrigerant liquid tube. Two temperature-wells are inserted inside the boiler to measure the vapor and liquid temperatures. The test section includes a shell-and-tube heat exchanger, which represents the condenser, as shown in Fig. 3. The cooling water flows through two similar tubes, whereas, the refrigerant flows through the shell, forming a counter flow.

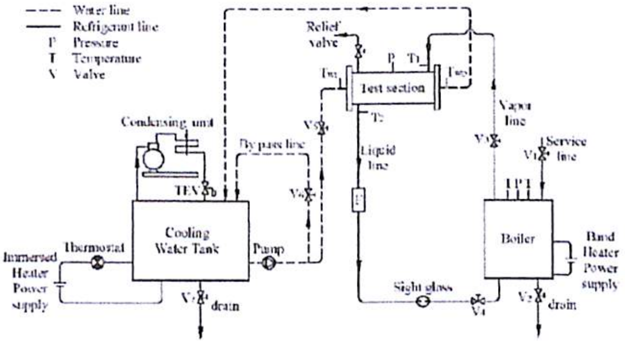

Fig. 1. Schematic diagram of the experimental apparatus

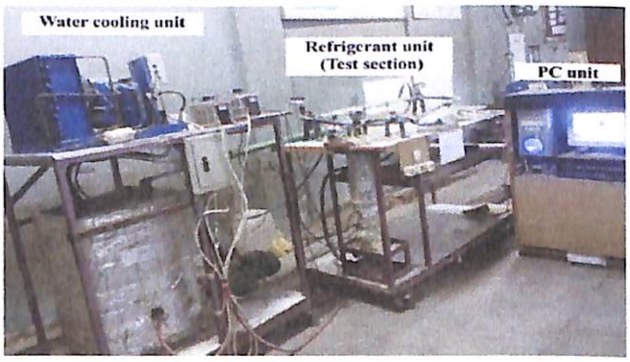

Fig. 2. Photo of the experimental test rig

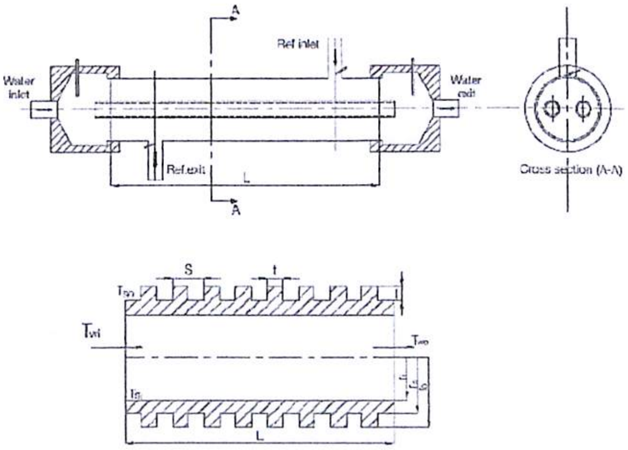

Fig. 3. Detailed of the test rig

The inner tubes are smooth or finned and are made of copper with an 11-mm inner diameter and 268-mm effective length. The specifications are depicted in Fig. 3 and are tabulated in Table I. The outer tube (shell) is made from brass with the same length. The vapor and liquid lines of the refrigerant, which connect the condenser and boiler, are made of copper with an inner diameter of 9.7 mm. A pressure measuring device is connected to the condenser at a mid-length position in order to obtain the condenser pressure.

TABLE I
CONFIGURATIONS OF SMOOTH AND FINNED TUBES UNDER INVESTIGATION (L=268mm AND d_i=11mm FOR ALL CASES)

Tube ID	Shape	S (mm)	H (mm)	t (mm)	A_t/A_{smooth}	d_b (mm)
Tube A	Triangle	1.0	0.5	0.0	1.37	15.5
Tube B	Trapezoidal	1.5	0.5	0.5	1.25	15.5
Tube C	Trapezoidal	2.0	0.5	1.0	1.19	15.5
Tube D	Trapezoidal	2.0	0.75	0.5	1.26	15.0
Tube E	Triangle	2.0	1.0	0.0	1.33	14.5
Smooth tube	-	-	-	-	1.00	16.5

For safety purposes, a relief valve and pressure-stat monitor are installed in the test section. If the test section pressure exceeds the design limit, the relief valve opens to release the pressure, and simultaneously, the electric heaters automatically shut off. The boiler, test section, and piping are thermally insulated. The coolant path, which is shown on the left side of Fig. 1, is used to provide cooling water to the test section at different conditions, which, in turn, cools the refrigerant until it reaches the point of condensation. The cooling water path consists of a water tank with a capacity of 250 L and a circulating water pump.

The cooling water flow rate is regulated by two control valves, represented by V_5 and V_6 in Fig. 1, on the main water line and by-pass line, respectively. The water tank is equipped with a cooling coil of 3.0 kW cooling capacity for the refrigeration unit and two electric heaters with a capacity of 4.0 kW in order to precisely control the cooling water temperature.

The refrigerant path, including the test section, boiler, and associated piping, is insulated with asbestos; however, the coolant path, including all of the associated piping and the water tank, is insulated by glass wool. The locations of the measuring devices for all of the investigated parameters, including the temperature, pressure, and flow rate, are displayed in Fig. 1. Type-K thermocouples are calibrated and used to measure the inlet and exit temperatures of the test section for the refrigerant and cooling water. Additionally, the inner and outer surface insulation temperatures are measured to compute the heat loss. The accuracy of the temperature measuring devices is within ±0.1°C. Pressure transducers are calibrated and mounted on the boiler and condenser to measure the vapor pressures. The accuracy of the pressure transducers is within ±0.01 bar. The mass flow rate of the cooling water is collected using a digital balance during a defined period. A 16-bit data acquisition system is used to gather the data from the thermocouples and pressure transducers that are mounted on the experimental test rig.

The refrigerant path and the associated accessories are tested for leakage, evacuated for 24 h, and charged with refrigerant. Additionally, a pre-determined quantity of refrigerant is charged into the boiler. The saturation temperature and pressure for the refrigerant are measured and recorded. However, to verify the accuracy of the measuring devices, the measured temperature is compared to the temperature of the corresponding measured pressure to ensure that non-condensable gasses are not present in the refrigerant path.

The experiments are carried out for both refrigerants (R1234yf and R134a) over a wide range of operating conditions, as presented in Table II. In order to conduct the experiments, the cooling water is tuned to a pre-defined condition, while the water flow and boiler electric heater are adjusted to a definite saturation pressure and temperature.

The data for the temperatures, pressures, and flow rates are collected when the test rig reaches a steady-state operating condition. Additionally, the effects of superheating and subcooling are neglected.

TABLE II
EXPERIMENTAL TEST CONDITIONS

Parameters	Values
Refrigerant type	R134a and R1234YF
Coolant inlet temperature (°C)	15–30
Cooling water velocity (m/s)	0.5 . 0.8, and 1.1
Tube geometry	Table I and Fig. 3

II.2. Data Reduction

The rate of heat transfer at the waterside (Q_w) of the test section can be obtained from Eq. (1):

$$Q_w = \dot{m}_w C_w (T_{wo} - T_{wi}) \quad (1)$$

The mean heat flux (q) can be determined from Eq. (2):

$$q = Q_w / A_t \quad (2)$$

where, A_t is calculated using Eq. (3):

$$A_t = N\, A_f + A_{uf} \quad (3)$$

The overall HTC can be evaluated from Eq. (4):

$$U = Q_w / (A_t\, LMTD) \quad (4)$$

where the logarithmic mean temperature difference ($LMTD$) can be determined from Eq. (5), considering the refrigerant saturation temperature and the inlet and exit temperatures of the cooling water:

$$LMTD = \frac{(T_{sat} - T_{wo}) - (T_{sat} - T_{wi})}{\ln\left[(T_{sat} - T_{wo}) / (T_{sat} - T_{wi})\right]} \quad (5)$$

Using thermal resistance principles [22], Eq. (6) can be considered:

$$\frac{1}{A_t U} = \frac{1}{A_i h_i} + \frac{\ln(r_b/r_i)}{2\pi k L} + \frac{1}{A_t h_o} \quad (6)$$

The wall conduction resistance determined by Eq. (6) is less than 2% of the outside convection resistance in the overall HTC equation. However, the condensation HTC on a finned tube (h_o) can be obtained from Eq. (7):

$$h_o = \left[\frac{1}{U} - \frac{A_t}{A_i h_i} - \frac{A_t \ln(r_b/r_i)}{2\pi k L}\right]^{-1} \tag{7}$$

The temperature of the outside surface of test section tube (T_s) can be calculated using Eq. (8):

$$T_s = T_{s,i} + [0.5 Q_w \ln(r_b / r_i) / 2\pi k L] \tag{8}$$

where, the inner surface temperature of the test section tube (T_{si}) is determined using Eq. (9):

$$T_{s,i} = \frac{(T_{wi} + T_{wo})}{2} + \frac{Q_w}{h_i A_i} \tag{9}$$

The convection HTC of the inside tube (h_i) can be determined using Eq. (10):

$$h_i = \mathrm{Nu}\, k_w / d_i \tag{10}$$

where Nu is the Nusselt number, which can be obtained using the Dittus and Boelter equation [23], shown in Eq. (11):

$$\mathrm{Nu} = 0.023\,\mathrm{Re}^{0.8}\,\mathrm{Pr}^{0.4} \tag{11}$$

It should be noted that the thermophysical properties are obtained at the average cooling water temperature through the test section. The Moffat technique [24] for evaluating the uncertainty of the reported data is considered herein. The uncertainties of the experimental parameters, including the mass flow rate of the cooling water, heat load, overall HTC, and condensation HTC, are found to be 1.5%, 3.2%, 4.8%, and 8.5%, respectively.

III. Results and Discussion

The R134a experimental data are gathered and compared with the data found in the literature, assuming the same operating conditions achieved after the test rig reaches steady-state operation. Experiments are conducted to evaluate the condensation heat transfer characteristics forR1234yf and R134a,considering the following operating conditions:

- Saturation temperature of 39°C
- Six copper tubes (one smooth tube and five finned tubes)
- Water inlet temperatures ranging from 15°C to 30°C
- Water velocities of 0.5 m/s, 0.8 m/s, and 1.1m/s

III.1. Results for the Smooth Tube

In order to validate the experimental results, the condensation HTCs for R134a and R1234yf obtained for the smooth tube are compared with those predicted using Nusselt's equation, which is shown in Eq. (12)[22], [23].

This comparison is shown in Fig. 4, which reveals that the predicted condensation HTCs are lower than the experimental condensation HTCs by approximately 13.8–20.7% for R1234yfand 2.8–14.2% forR134a at the saturation vapor temperature of 39°C. This is in agreement with the previous work conducted by Jung et al. [25], which determined that Nusselt's equation yielded a 12% deviation for the smooth tube data when R123 and R1234yf were used as alternative refrigerants for R11 and R134a, respectively. Additionally, Nguyen and Orozco [26] noted that, by applying Nusselt's equation to the condensation of R152a, the data were found to be accurate within 15%:

$$h_{Nu} = 0.729\left[\frac{g\, \rho_l^2 k_l^3 h_{fg}}{\mu_l\, d_o\, \Delta T_{sat}}\right]^{0.25} \tag{12}$$

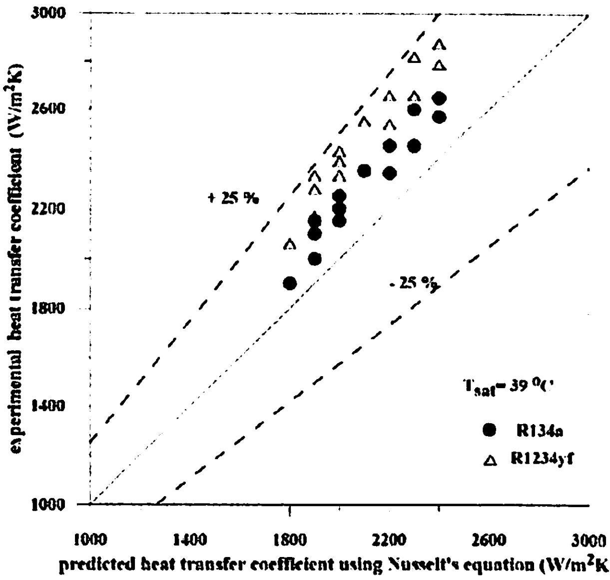

Fig. 4. Comparison of the experimental and predicted condensation HTCs using Nusselt's equation on a smooth tube

The deviation between the experimental and predicted data may be attributed to the assumption used in deriving Nusselt's equation (Eq. (12)) that the condensate film is laminar. In reality, the condensate film is wavy even for small Reynolds number values, which generates convection currents and consequently, reduces the film thickness. Considering this, the comparison proves that the current experimental data for the smooth tube are essentially accurate, and the test rig is capable of producing reliable data.

III.2. Effects of Water Velocity

Fig. 5 represents the effects on the R1234yf generated by different water velocities on the smooth tube, which demonstrates that the heat flux increases with increasing water velocity. An increase in the water velocity, in turn, increases the Reynolds number, and consequently, the convective heat transfer increases, leading to an increased heat flux. The average condensation heat flux increases by approximately 23.6% when the water velocity increases from 0.5 m/s to 1.1m/s over the applied range of inlet water temperatures. The increase in condensation heat flux as the water velocity changes from 0.5 m/s to 0.8 m/s is greater than the increase in condensation heat flux for the water velocity increase from 0.8 m/s to 1.1 m/s. In addition, as the water inlet temperature increases, the velocity has a reduced effect on the heat flux.

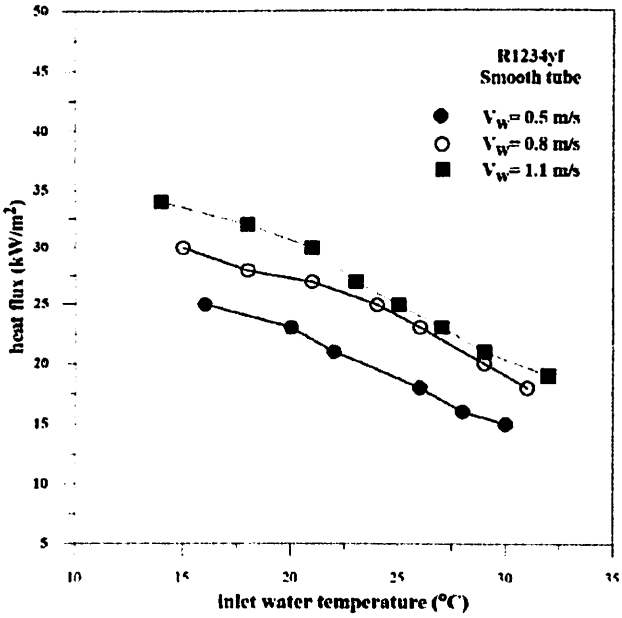

Fig. 5. Heat flux versus inlet water temperature for different water velocities

III.3. Effects of Water Inlet Temperature

The effects of various water inlet temperatures on the heat transfer characteristics of R1234yfare investigated by considering the heat flux variations produced by the smooth tubes and finned tubes, while the water inlet temperature varies from 15°C to 30°C and the saturation temperature remains constant at 39°C. The results for the smooth tube are shown in Fig. 5, and the results for the finned tubes are shown in Figs. 6 and 7. Fig. 5 presents the results of the various inlet water temperatures for the smooth tubes; at a water velocity of 0.8m/s, heat fluxes of 30.1 kW/m^2 and 18.5kW/m^2 are obtained at water temperatures of 15°C and 30°C, respectively. Thus, the average heat flux decreases by 38.5% when the water inlet temperature increases from 15°C to 30°C. At a constant water velocity, a lower water inlet temperature leads to a larger water temperature difference due to a thicker condensation film, and thus, a higher heat flux can be obtained. In general, reducing the inlet temperature of the cooling water and increasing the water velocity augments the condenser heat exchange.

Therefore, the water inlet temperature is a factor in evaluating the heat flux working range. This effect is consistent with the results from previous research conducted by Cheng and Wang [27]. Secondly, the effects of the inlet water temperatures for the finned tubes can be assessed by determining the heat flux variations with different inlet water temperatures for various fin pitches, thicknesses, and heights, as shown in Figs. 6 and 7.

The figures show the results for a constant water velocity of 0.8m/s. For all of the cases, the heat flux decreases when the water inlet temperature increases.

III.4. Effects of Fin Geometry

Five finned tubes are used to explore the effects produced by various fin geometries on the condensation heat transfer characteristics of R1234yf over finned tubes. Three tubes have a constant fin height (H) of 0.5mm with three fin pitches (S) of 1.0 mm, 1.5 mm, and 2.0 mm and corresponding fin thicknesses (t) of 0.0 mm, 0.5 mm, and 1.0mm for Tubes A, B, and C, respectively. The other three finned tubes have a fixed fin pitch of 2.0 mm with three fin heights of 0.5 mm, 0.75 mm, and 1.0mm and corresponding fin thicknesses of 1.0 mm, 0.5 mm, and 0.0mm for Tubes C, D, and E, respectively. The parameters of the tested tubes are provided in Table I and are illustrated in Fig. 3. The effects of different fin geometries are investigated with respect to the condensation heat flux and the condensation HTC. Figs. 6 and 7 present the variations of the condensation heat flux with respect to the inlet water temperature for various fin geometries. As shown in Fig. 6, the heat flux increases as the fin pitch and thickness increase. This increase may be attributed to an increase in the turbulence level. The average heat flux of R1234yf over the considered range of water temperatures at a water velocity of 0.8 m/s increases by approximately 44%when the fin pitch increases from 1 mm to 2mm and the fin thickness increases from 0.0 mm to 1.0mm. This increase is due to the combined effects caused by the fin pitch and fin thickness. Fig. 7 indicates that the heat flux increases as the fin height decreases and the fin thickness increases. For the condensation of R1234yf, the increase in the average heat fluxes are approximately 2.5% when the fin height is reduced from 1.0 mm to 0.75 mm (the fin thickness increases from 0.0 to 0.5mm) and approximately 45% when the fin height is reduced from 0.75 mm to 0.5mm (the fin thickness increases from 0.5 mm to 1.0mm). This indicates the significance of the combined effects on the condensation characteristics of R1234yf produced by the fin height and thickness. This trend is coincident with that reported by Kumar et al. [4]-[5]. Figs. 8 illustrate the condensation HTCs of R1234yf for the finned and smooth tubes as a function of the saturation temperature difference (T_{sat}–T_s) over the full range of water velocities and water inlet temperatures.

Figs. 8 show that the condensation HTC decreases as the saturation temperature difference increases. This trend can be explained by the increase in condensate film thickness generated by an increase in the saturation temperature difference. Thereby, the condensation thermal resistance increases, causing the condensation HTCs to decrease. Moreover, the condensation HTCs of R1234yfover the finned tubes are more sensitive to the saturation temperature difference than the condensation HTCs of R1234yf over the smooth tube. This is indicated by steeper lines lope for the finned tubes cases compared to the smooth tube case.

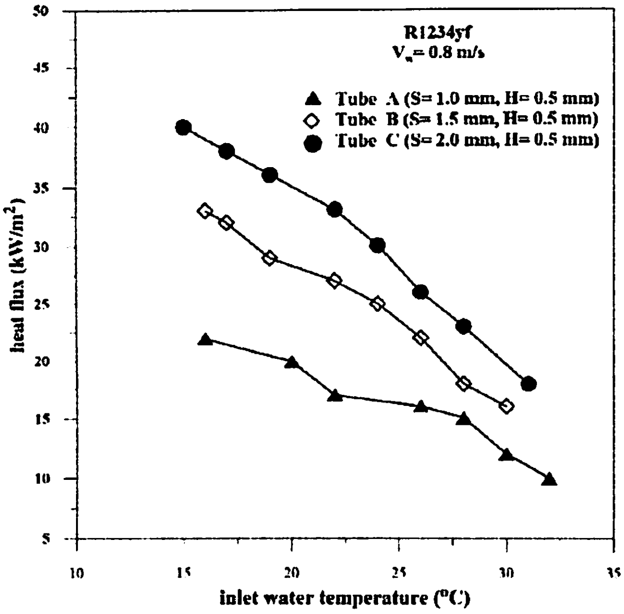

Fig. 6. Heat flux versus inlet water temperature for various fin pitches

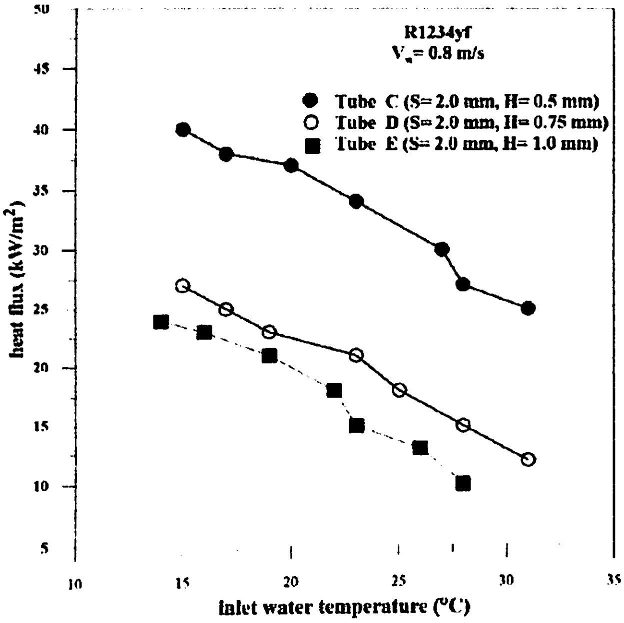

Fig. 7. Heat flux versus inlet water temperature for various fin heights

For a constant fin height, the condensation HTC increases as the fin pitch and thickness increase, as shown in Fig. 8(a). This may be explained by the considerable reduction of the thermal resistance caused by the diffusion vapor film. For R1234yf, the average heat transfer enhancement ratios (HTERs) of Tube A, Tube B, and Tube C are 1.57, 1.88, and 2.17, respectively.

Thus, the HTERs of Tube C are higher than those of Tube A and Tube B, indicating that Tube C provides the best performance. This is due to its large fin pitch and thickness, which make the condensate escape mechanism easier. It should be noted that the total area of Tube C is smaller than that of the other two tubes.

Moreover, the difference between the HTCs of Tube A and Tube B is approximately the same as the difference in HTCs between Tube B and Tube C, which demonstrates a linear relationship between the condensation HTCs and the fin pitch, as shown in Fig. 8(a).

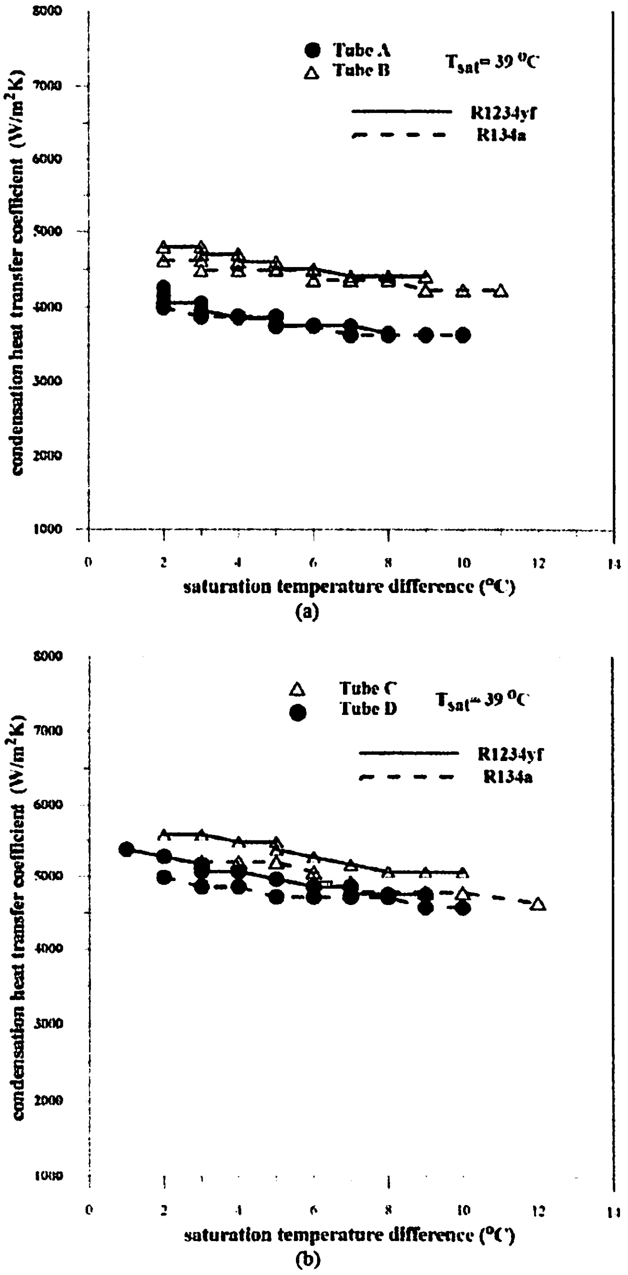

Figs. 8. Effect of fin pitch and height on the condensation HTC of R1234yf

Furthermore, the enhancement of the finned tubes is measured by the HTERs, which are defined by the average HTCs of the finned tubes divided by the average HTCs of the smooth tube under the same operating conditions.

The combined effect produced by the fin height and thickness on the condensation HTCs can be predicted by comparing the condensation HTCs for the smooth tube, TubeC, TubeD, and TubeE, as illustrated in Fig. 8(b).

As shown in Fig. 8(b), while the fin pitch is maintained as constant for a given saturation temperature difference, the R1234yf condensation HTCs increase as the fin thickness increases and the fin height decreases.

As shown in Fig. 8(b), the R1234yf HTERs for Tube C, Tube D, and Tube E are 2.17, 2.04, and 1.78, respectively. The HTERs of TubeC are larger than those of Tube D and Tube E.

This confirms that the best performance is achieved by Tube C due to the easy condensate escape mechanism caused by the increase in the fin thickness and reduction of the fin height. Furthermore, it is worth nothing that the total area of Tube C is smaller than that of Tube D and Tube E.

Additionally, the increase in the condensation HTCs as the fin thickness increases from 0.0 mm to 0.5 mm and the fin height decreases from 1.0 mm (TubeE) to 0.75mm (Tube D) is approximately twice the increase in the condensation HTCs that occur when the fin thickness increases from 0.5 mm to 1.0 mm and the fin height reduces from 0.75 mm to 0.50mm. This provides a non-linear relationship between the condensation HTCs and the fin height, as shown in Fig. (8B).

Figs. 6, 7, 8(a), and 8(b) show that Tube C (with a fin thickness of 1.0mm, fin pitch of 2.0 mm, and fin height of 0.5mm) achieves the highest condensation heat flux and condensation HTC. On the other hand, Tube A (with a fin thickness of 0.0 mm, fin pitch of 1.0 mm, and fin height of 0.5 mm) attains the lowest heat flux and condensation HTCover the considered finned tubes.

Thus, the effects generated by the fin thickness or fin pitch are more significant than the effects generated by the fin height.

In conclusion, a tube with a larger fin thickness, larger fin pitch, and smaller fin height achieves the highest heat flux and condensation HTC.

III.5. Comparison Between R1234yf and R134a

A comparison between the condensation HTCs for R1234yf and R134a over the horizontal smooth tube and finned tubes was carried out at a saturation temperature of 39°C with various water velocities and inlet water temperatures.

Figs. 9 display the comparison between the condensation HTCs for R134a and R1234yf with respect to different tube geometries. As shown in Figs. 9, for all of the tested tubes, the condensation HTCs of both R1234yf and R134a decrease as the saturation temperature differences increase.

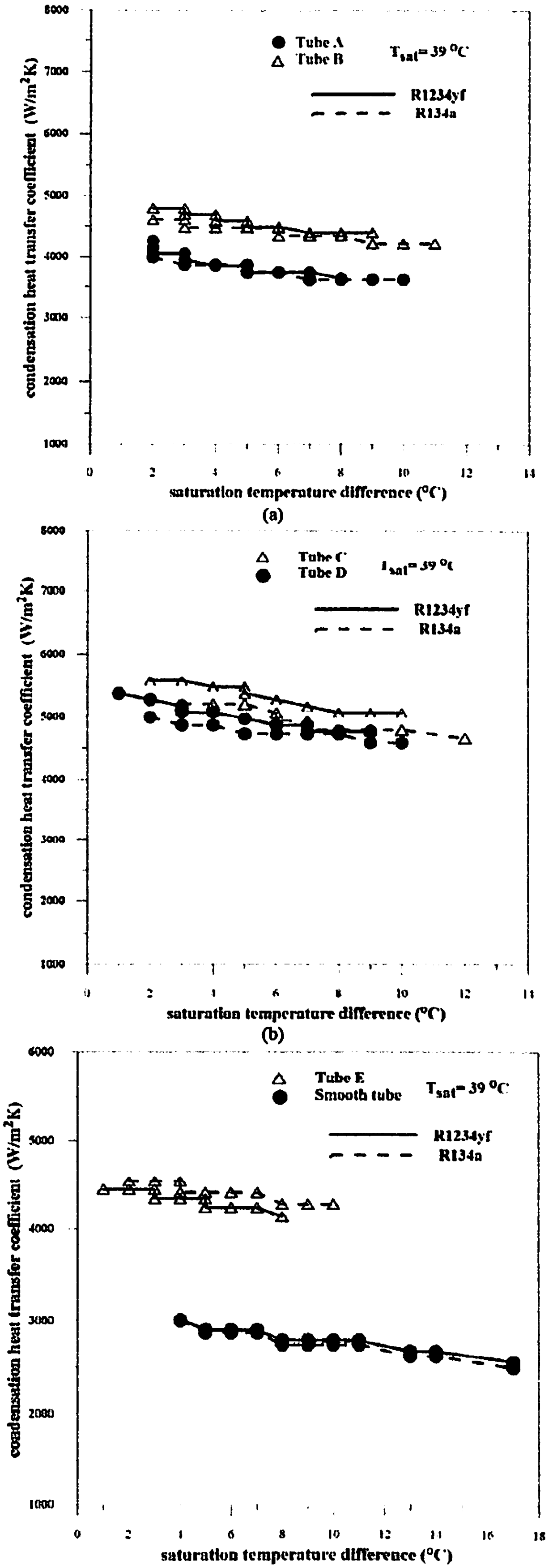

Figs. 9. Comparison between R1234yf and R1

Over the range of operating conditions, the average R1234yf condensation HTCs over Tube A, Tube B, Tube C, Tube D, Tube E, and the smooth tube are slightly greater than those of the R134a by approximately 1.6%, 1.1%, 3.1%, 3.4%, 1.1%, and 0.9%, respectively, as shown in Figs. 9(a), 9(b), and 9(c).

Thus, Tube C and Tube D yield the highest increase (approximately 3%) for the R1234yf condensation HTCs when compared to those of R134a. Moreover, Tube A and Tube E provide higher R1234yf condensation HTCs when compared to those of R134a by approximately 1.4%.

The smooth tube offers only a 0.9% increase in the R1234yf condensation HTCs when compared to those of R134a. The preceding comparison reveals that R1234yf offers slightly higher condensation heat transfer characteristics than R134a and thus, might be an environmentally-friendly solution that can be used as an alternative to R134a for condensation heat transfer applications.

Thus, the finned tubes should be redesigned to consider the heat transfer characteristics of R1234yf for its performance enhancement in practical applications.

IV. Conclusion

In this study, the condensation HTCs for the environmentally friendly refrigerant, R1234yf, which is a possible alternative to R134a, are investigated on horizontal smooth and finned tubes. The effects on the R1234yf and R134a condensation HTCs are studied at a saturated vapor temperature of 39°C for different fin geometries, including the fin pitch (1.0 mm, 1.5 mm, and 2.0 mm), fin thickness (0.0 mm, 0.5 mm, and 1.0 mm), and fin height (0.5 mm, 0.75 mm, and 1.0 mm).

Additionally, the effects on the R1234yf and R134a condensation HTCs are studied according to various water velocities (0.5 m/s, 0.8 m/s, and 1.1 m/s) and inlet water temperatures (ranging from 15°C to 30°C). Based on the reported results, the R1234yf condensation HTCs are slightly higher than those of R134a, and thus, it can be stated that R1234yf is a potential substitute for R134a.

The following conclusions are drawn:

- The average predicted condensation HTCs of R134a and R1234yf on the smooth tube, using the Nusselt equation, are lower than the obtained experimental values by approximately 8.5% and 17.25%, respectively, at similar conditions.
- The average condensation heat flux of R1234yfon the smooth tube increases by approximately 23.6% when the water velocity increases from 0.5 m/s to 1.1m/s over the investigated range of inlet water temperatures.
- The average heat flux of R1234yf over the applied range of water temperatures at a water velocity of 0.8 m/s increases by approximately 44% as the fin pitch increases from 1.0 mm to 2.0 mm and the fin thickness increases from 0.0 mm to 1.0mm.
- The tube with the largest fin thickness, largest fin pitch, and smallest fin height enhances the heat flux and condensation HTC.
- The tube with a fin thickness of 1.0mm, fin height of 0.5mm, and fin pitch of 2.0mm produces average condensation HTCs that are more than twice (2.17)those of the smooth tube and are higher than the other tested finned tubes.
- The R1234yfcondensation HTCs are slightly higher than thoseofR134a by approximately 0.9% for the smooth tube and by approximately 3.4% for the best finned-tube configuration.

Due to the importance of using the Hydrofluoroolefin refrigerant (R1234yf) as an alternative refrigerant, the authors suggested to conduct experimental runs with different aspect ratios to further quantify the effect of aspect ratios for condensation. These runs should be done with visualization tests and use these results with the existing study to create a flow patterns map. The importance of the flow pattern maps and the results of the additional tests can be used to develop more reliable correlations for condensation HTCs.

Acknowledgements

The authors thank the Deanship of Scientific Research and RSSU at King Saud University for their technical support.

References

[1] Jha, R., Haribhakta. V., Kolte. A., Shekhadar. S., Tengale. S., Tare, S.. Design and Simulation of Condensing Heat Exchanger, (2017) *International Review of Mechanical Engineering (IREME)*. 11 (7), pp. 473-480. doi: https://doi.org/10.15866/ireme.v11i7.12879

[2] J. F. Seara. J. U. Francisco. J. Sieres. Research on the Condensation of the Ammonia–Water Mixture on a Horizontal Smooth Tube. *International Journal of Refrigeration*, Vol. 310. pp. 304-314, 2008.

[3] D. Jung, S. Chaea, D. Baea. S. Ohob. Condensation Heat Transfer Coefficients of Flammable Refrigerant. *International Journal of Refrigeration*, Vol. 27. pp. 314-317. 2004.

[4] R. Kumar, H. K. Varma. B. Mohanty, K. N. Agrawal. Augmentation of Outside Tube Heat Transfer Coefficient during Condensation of Steam over Horizontal Copper Tubes. *International Communications of Heat and Mass Transfer*. Vol. 25(I). pp.81-91. 1998.

[5] R. Kumar. H. K. Varma, B. Mohanty. K. N. Agrawal. Prediction of Heat Transfer Coefficient during Condensation of Water and R-134a on Single Horizontal Integral-Fin Tubes. *International Journal of Refrigeration*. Vol.25, pp.11-126. 2002.

[6] R. Kumar. A. Gupta. S. Vishvakarma. Condensation of R134a Vapor over Single Horizontal Integral-Fin Tubes: Effect of Fin Height, *International Journal of Refrigeration*. Vol. 28. pp. 428-435. 2005.

[7] A. Briggs. J. W. Rose, Effect of Fin Efficiency on a Model for Condensation Heat Transfer on a Horizontal. Integral-Fin Tube. *International Journal of Heat and Mass Transfer*. Vol. 37(1).pp. 457-463. 1995.

[8] A. Reif. A. Büchner. S. Rehfeldt. H. Klein. Outer Heat Transfer Coefficient for Condensation of Pure Components on Single Horizontal Low-Finned Tubes. *Heat and Mass Transfer*. 2007. https://doi.org/10.1007/s00231-017-2184-3

[9] Y. T. Kang. H. Hong. Y. S. Lee. Experimental Correlation of Falling Film Condensation on Enhanced Tubes with HFC134a: Low-Fin and Turbo-C Tubes. *International Journal of*

Refrigeration, Vol. 30, pp.805-811, 2007.

[10] A. Büchner, A. Reif, S. Rehfeldt, H. Klein, Condensation of Binary Mixtures on Horizontal Tubes, *Heat and Mass Transfer*, 2017. https://doi.org/10.1007/s00231-017-2250-x

[11] T. Karlsson,L. Vamling, Surprising effects of combined vapor and liquid mass transfer resistances when condensing a mixture outside tube banks, *Int J Heat and Mass Tran* 48 (2005) 403-412.

[12] H. Honda, H. Takamatsu, N. Takada, Condensation of HCFC123 in Bundles of Horizontal Finned Tubes: Effects of Finned Geometry and Tube Arrangement, *International Journal of Refrigeration*, Vol. 19, pp.1-9, 1996.

[13] H. Honda, H. Takamatsu, N. Takada, Condensation of Downward-Flowing Zeotropic Mixture HCFC-123/HFC-134a on a Staggered Bundle of Horizontal Low-Finned Tubes, *Journal of Heat Transfer*, Vol. 121(2), pp. 405-412, 1999.

[14] H. Honda, H. Takamatsu, N. Takada, J.S. Kim, K.Usami, Condensation of Downward-Flowing HFC134a in a Staggered Bundle of Horizontal Finned Tubes Effect of Fin Geometry, *International Journal of Refrigeration*, Vol. 25, pp. 3-10, 2002.

[15] S. Brown, C. Zilio, R. Brignoli, A. Cavallini, Thermophysical Properties and Heat Transfer and Pressure Drop Performance Potentials of Hydrofluoro-Olefins, Hydrochlorofluoro-Olefins, and their blends, *HVAC&R Research*, Vol. 20(2), pp.203-220, 2014.

[16] Airedale, *Turbo Chill Free Cool*, 2015.

[17] GEA Consulting, *MHI Chooses HFO-1233zd(E) for New Centrifugal Chillers*, 2015.

[18] ECN, *R&D on Industrial Heat Pumps*, 2014.

[19] D. Del Col, D. Torresin, A. Cavallini, Heat Transfer and Pressure Drop during Condensation of the Low GWP Refrigerant R1234yf, *International Journal of Refrigeration*, Vol. 33, pp.1307-1318, 2010.

[20] K. Park, D. G. Kang, D. Jung, Condensation Heat Transfer Coefficients of R1234yf on Plain, Low Fin, and Turbo-C Tubes, *International Journal of Refrigeration*, Vol.34, pp.317-321, 2011.

[21] K. Park, D. G. Kang, D. Jung, Critical Heat Flux: Performance of R1234yf, R1234ze and R134a in an Aluminum Multi-minichannel Heat Sink at High Saturation Temperatures, *International Journal of Thermal Science*, Vol. 106, pp.1-16, 2016.

[22] Ibrahim, T. A., Hassan, M. A. M., Condensation Heat Transfer Characteristics of R22, R134a, R410A and R407C on Single Horizontal Plain and Finned Tubes, (2013) *International Review of Mechanical Engineering (IREME)*, 7 (4), pp. 664-672.

[23] F. P. Incropera, P. DeWitt, *Fundamentals of Heat and Mass Transfer*, John Wiley & Sons, New York, 2003.

[24] R. Moffat, *Describing the Uncertainties in Experimental Results, Experimental Thermal and Fluid Science*, Elsevier Science Pub. Co. Inc, New York, 1988.

[25] C. Jung, B. Kim, S. Cho, K. Song, Condensation Heat Transfer Coefficients of Enhanced Tubes with Alternative Refrigerants for CFC11 and CFC12, *International Journal of Refrigeration*, Vol. 22,pp. 548-557, 1999.

[26] T. N. Nguyen, J. A. Orozco, Condensation of R113 on Enhanced Surfaces, *ASHRAE Transactions*, Vol. 100(1), pp.736-743, 1994.

[27] W. Y. Cheng, C. C. Wang, Condensation of R410A on Enhanced Tubes, *ASHRAE Transactions*, Vol.100(1), pp.809-817, 1994.

[28] Choudhari, C., Sapali, S., Experimental Performance Analysis of Refrigerant R290 for Water Cooler Application, (2017) *International Review of Mechanical Engineering (IREME)*, 11 (6), pp. 419-425. doi:https://doi.org/10.15866/ireme.v11i6.12843

Authors' information

[1]Mechanical Power Engineering Department,
Faculty of Engineering-Mattaria, Helwan University, Cairo, Egypt.

[2]Vice Presidency for Projects, King Saud University, Riyadh,
Kingdom of Saudi Arabia.

Talaat A. Ibrahim was born in Oct. 27th, 1967, Alqalyoubia, Egypt. He received his M.Sc. in 1996 from Faculty of Engineering – Mattaria, Helwan University, Cairo, Egypt. He obtained his PhD in 2002 from Institute of Thermal Engineering, Graz University of Technology, Austria. The subject of his PhD was Thermally Activated Air Conditioning Systems. He is working as an Associate Professor at Mechanical Power Engineering Department, Faculty of Engineering-Mattaria, Helwan University, Cairo, Egypt. His research field is focused on heat and mass transfer, air conditioning systems and applications. He published several research articles in many reputed international journals and conferences. Dr. Ibrahim is currently working as an Associate Professor and Mechanical Consultant at Vice Presidency for Projects, King Saud University, Riyadh, Kingdom of Saudi Arabia as a sabbatical leave from College of Engineering, Helwan University, Egypt. He is leading teams for upgrading, design and installing HVAC and Building Management Systems with large capacities and sophisticated control.

E-mail: talaat_fayed@yahoo.com

Mohamed A. M. Hassan was born in Cairo-Egypt in Oct., 1st, 1970. From Jan. 2000 - Feb. 2004, he got his PhD in Mechanical Engineering (specialization: heat transfer and refrigeration), Mechanical Engineering Department, Technical University of Denmark, Lyngby, Denmark, 2004. The major filed of is refrigeration and heat transfer. M.A.M. Hassan is now an Associate Professor in the Department of Mechanical Power Engineering, Faculty of Engineering-Mattria- Helwan University, Egypt He is a research scientist with 23 years of research experience in the field of refrigeration and heat transfer. His current research interest is Thermal Energy and alternative refrigerants

E-mail: marmdtu@yahoo.com

Praise Worthy Prize

International Review of Mechanical Engineering (I.RE.M.E.), Vol. 12, N. 10
ISSN 1970 - 8734 *October 2018*

Random Versus Periodic Microstructures for the Thermal Conductivity of Fiber-Reinforced Composites

S. El Marzouki[1], T. Kanit[2], H. El Minor[1]

Abstract – *Periodic models are often used for the homogenization of fiber-reinforced materials. The periodic distribution of the inclusions is a simplifying assumption that fails to give a realistic representation of the actual materials which demonstrate a random arrangement of fibers. The present study is a comparison between the periodic model and the random one. An intermediate configuration was introduced in which a periodic hexagonal cell of varying size is embedded inside a microstructure of a random distribution of fibers. The results of the homogenization showed similarities between the macroscopic behavior of the random model and the intermediate models. It also highlighted the discrepancies between the effective thermal conductivities of the periodic model and the random one. Furthermore, the analysis of the thermal field maps of the three types of configurations helped determine the reason behind the difference in the macroscopic response of the random model and the periodic one based on their local behavior. Lastly, it was concluded that the periodic model should solely be used to determine the macroscopic behavior of the fiber-reinforced composites, only if no significant precision is required.* ***Copyright © 2018 Praise Worthy Prize S.r.l. - All rights reserved.***

Keywords: *Fiber-Reinforced Composites, Numerical Homogenization, Periodic Microstructures, Random Microstructures, Thermal Conductivity, Unidirectional Fibers*

Nomenclature

c	Thermal contrast
G	Macroscopic gradient of temperature
i	Relative to inclusions
m	Relative to the matrix
q	Heat flux
S	Surface
T	Temperature function
t	Periodic temperature fluctuation
x	Spatial position
λ	Thermal conductivity
∇	Gradient
$\langle \nabla T \rangle$	Spatial average
$\underline{}$	Vector

I. Introduction

Inclusions add strength to a material and generally upgrade its performance to meet the user's needs and requirements on different levels. And while they add complexity to the composite's mechanical, thermal and overall behavior, they also add complexity to the study of its behavior and the estimation of its properties. Fibers are no exception [1]-[28]. The advantages of using this type of inclusions are numerous [1] but the modeling of fiber reinforced composites remains a complex task, [2]-[4], [27][28] and entails a highly time consuming process of homogenization of the macroscopic properties.

For simplicity, composite materials, including the fiber–reinforced ones, have been studied by performing the homogenization on periodic models [5]. This method has long been used to predict the effective properties of fiber reinforced composites [6]-[8]. It consists in reducing the Representative Volume Element (RVE) to an elementary square or hexagonal cell surrounding a single inclusion.

And while it gives satisfying results, the spatial distribution and the boundary conditions remain an issue as they are not representative of the real microstructures, which display a random distribution of inclusions and different boundary conditions. Therefore, a random arrangement was opted for in some studies, [9] and [10], and a comparison of both models was carried out in others [11]-[13]. In this study, numerical homogenization operations were performed on a fiber reinforced composite with longitudinally distributed fibers. The random and the hexagonal periodic methods were both used. A third approach was also utilized. The latter is a take on the embedded cell approach, [14]-[16], which allows a more realistic representation of the boundary conditions. This method calls for the use of an intermediate model constructed with an embedded cell and an outer region constituted of randomly arranged fibers. The embedded cell consists of a varying number of inclusions arranged periodically in a hexagonal pattern at the centre of the microstructure. The reason why the embedded region is hexagonal is to allow the comparison between the local behaviours of the random and the

https://doi.org/10.15866/ireme.v12i10.13711

hexagonal periodic scheme. In fact, by changing the size of the embedded cell and therefore changing the number of inclusions it holds, it either results in a completely random microstructure, one inclusion in the inner region, or falls into the periodic scheme, an infinite number of periodically arranged inclusions. The present investigation compares the thermal behaviors of the random model and the periodic one by using three different configurations of the embedded cell model and analyzing the local response in each and every generated microstructure. It is complimentary to a similar study [13], which focused on the elastic behavior of the same fiber reinforced composite. Section II describes the different configurations, and the methods used to generate them, in addition to the overall properties of the composite. Section III presents the analysis of the mesh density and introduces the constitutive laws and the boundary conditions used to perform the numerical homogenization. Section IV discusses the results of the homogenization on a macroscopic level and in terms of local behavior. It also highlights and analyzes the differences and similarities between the different models.

II. Microstructures and Materials

II.1. Generation of Microstructures

In total, six microstructures were generated. They represent the three different types on which a comparative study will be performed.

Type 1: the random configuration, which will be labelled random. Type 2: the intermediate configurations, otherwise the embedded cell configurations. This category combines four different microstructures named H7, H19, H37 and H61. Type 3: the periodic configuration. Types 1 and 2 both consist of a surface of a square section throughout which 200 fibers were arranged in parallel. In all of these configurations, a test fiber, circled in red in Figs. 1, is placed at the center of the cross-section. Except for the random configuration, this fiber is then surrounded by a series of hexagonal outlines holding a specific number of fibers periodically distributed around the test inclusion. As shown in Figs. 1, the hexagonal regions, or embedded cells, in H7, H19, H37 and H61 respectively contain 7, 19, 37 and 61 fibers including the central one. These regions modelled while maintaining the same surface fraction as the remainder of the microstructure. The rest of the 200 fibers are randomly distributed in the surface. As for the random configuration, 199 inclusions are randomly placed around the test fiber. Type 3 is the RVE to an infinite periodic fiber reinforced material. It is a unit–cell configuration consisting of a single fiber centered in a surface of a hexagonal section.

II.2. Material Properties

The six different configurations are all intended to represent the same material; a two-phase thermal linear composite with unidirectional fibers. The surface fraction and thermal properties remain the same for the random, the periodic and the intermediate configurations. While the volume fraction is set at p=50%=0,5 for the entire study, the thermal properties, λ_i for the fibers and λ_m for the matrix, are assorted to have three different contrasts, $c_\lambda = \lambda_i / \lambda_m$ =10, 50 and 100 for an inclusion's thermal conductivity of respectively λ_i= 10W/km, 50 and 100.

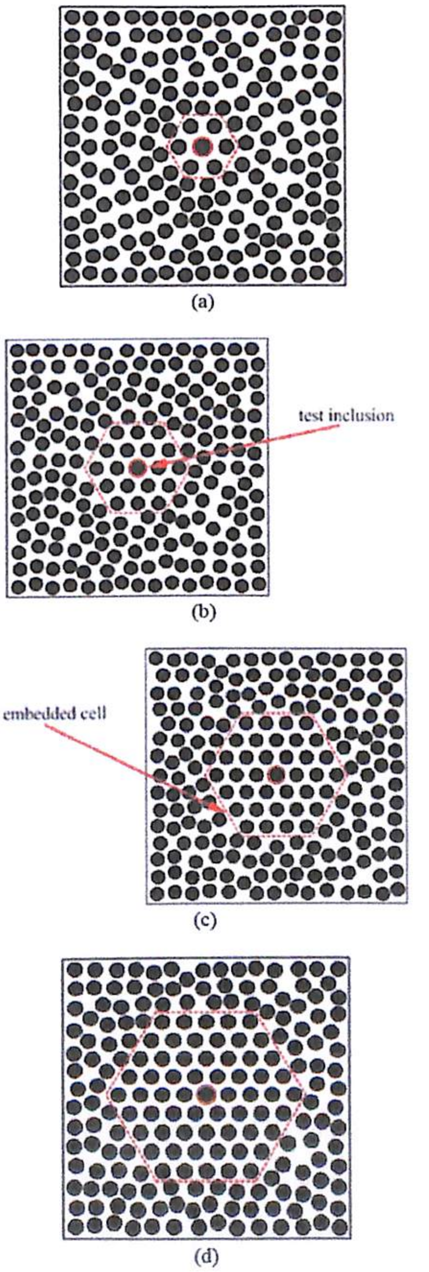

(a)

(b)

(c)

(d)

Figs. 1. The 4 different intermediate configurations (a) H7, (b) H19, (c) H37 and (c) H61

III. Numerical Homogenization

III.1. Mesh Density

For the periodic model, and as shown in Fig. 2(a), a mesh adapted to the shape of the microstructure is used.

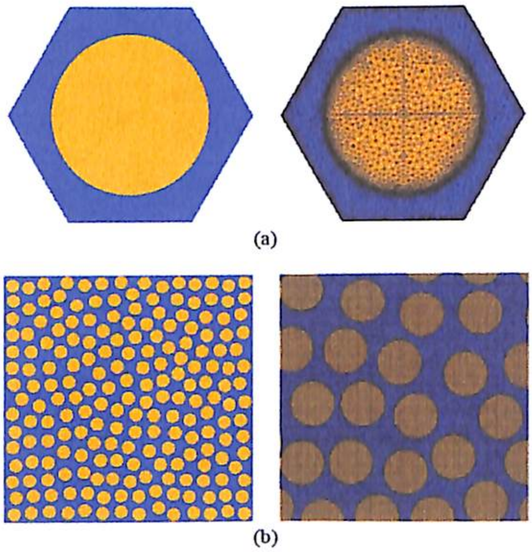
(a)

(b)

Figs. 2. Meshing of the (a) periodic model and (b) the random model

For the random distribution, a multiphase element technique is used, see Fig. 2(b). This technique was developed in [17] and extensively used in [12], [13] and [18]-[26], for the homogenization of virtual and real microstructures. Using the multi-phase element technique, an image of the microstructure is overlaid with a regular square grid, and each integration point is attributed its corresponding phase property depending on the color of the voxel underneath it. To ensure the accuracy of the results, a mesh density analysis was conducted on the multiphase element mesh to determine from which mesh density the simulation results start falling into a coherent range, regardless of the employed mesh. Several homogenization operations were carried out on the same microstructure for different mesh densities. Fig. 3 gives the variation of the macroscopic thermal conductivity according to the number of finite elements constituting the mesh. It is noticed that, from 4×10^4 elements onward, the homogenization results start becoming more consistent, showing a precision of less than 2%. For optimal results, a mesh of $2{,}5\times10^5$ finite elements was chosen. It allows a precision of less than 1,2%.

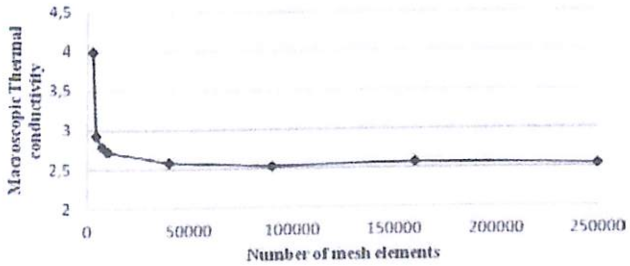

Fig. 3. Variation of the macroscopic thermal conductivity according to the number of mesh elements

III.2. Constitutive Laws and Boundary Conditions

The thermal behavior is described by Fourier's law where the heat flux vector $\underline{q}$ is a function of the thermal conductivity λ and the temperature gradient $\underline{\nabla T}$ as shown in (1):

$$\underline{q} = -\lambda \underline{\nabla T} \tag{1}$$

The numerical homogenization is carried out using two types of boundary conditions; PBC and UGT. UGT stands for Uniform Gradient of Temperature, where a temperature gradient is applied to the boundary of the surface, as expressed bellow:

$$T = \underline{G}\cdot\underline{x} \qquad \forall\underline{x} \in \partial S \tag{2}$$

$\underline{G}$ is a constant vector independent from the position x and:

$$\underline{G} = \langle\underline{\nabla T}\rangle = \frac{1}{S}\int \underline{\nabla T} dS \tag{3}$$

$\langle\underline{\nabla T}\rangle$ is the spatial average of the temperature gradient.

The macroscopic thermal flux $\underline{Q}$ is defined as the spatial average of the microscopic fluxes $\underline{q}$ along the surface as:

$$\underline{Q} = \langle\underline{q}\rangle = \frac{1}{S}\int \underline{q} dS \tag{4}$$

For the PBC, or the Periodic Boundary Conditions, a periodic temperature T is applied to the nods of the edges ∂S, which can be expressed as:

$$T = \underline{G}\cdot\underline{x} + t \qquad \forall\underline{x} \in \partial S \tag{5}$$

t is the periodic fluctuation. The thermal conductivity is computed in both cases, PBC and UGT, given a macroscopic temperature gradient $\underline{G}$=(1 1).

The homogenized thermal conductivity λ^e is therefore defined as:

$$\lambda^e = \frac{1}{2} trace(\langle\underline{q}\rangle) \tag{6}$$

IV. Results and Discussions

IV.1. Global Behavior

First, the homogenized thermal conductivityλ^e was calculated for the random configuration using both PBC and UGT, for 10 different contrasts c_λ ranging from 10 to 100.

Although the PBC computations converge faster, it is important to use the UGT as well, considering the fact that the convergence of the results of both boundary conditions means that the chosen RVE is indeed representative of the microstructure. Fig. 4 shows an analogy between the results obtained with both boundary conditions.

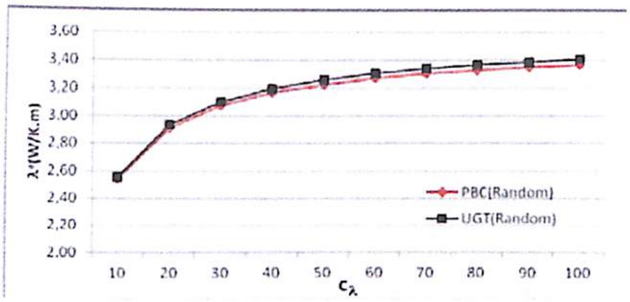

Fig. 4. The evolution of the macroscopic thermal conductivity according to contrasts

The insignificant discrepancy between the PBC and the UGT results confirms our choice of the RVE. Thus, the apparent thermal conductivity λ^a and the effective one λ^e converge. It is then possible to admit that the results of the following calculations correspond to the effective thermal conductivity λ^e. Secondly, the homogenization was performed on the remaining configurations for three different contrasts c_λ=10, 50 and 100. From this point on, only the results corresponding to the PBC will be taken into account, since both boundary conditions give approximately the same results. Table I compares the results obtained via the periodic scheme to those calculated using the analytical bounds of Hashin and Shtrikman.

TABLE I
THE EFFECTIVE THERMAL CONDUCTIVITIES λ^E [W K^{-1} m^{-1}] OF THE PERIODIC CONFIGURATIONS COMPARED TO THE HASHIN-SHTRIKMAN BOUNDS

Contrast c_λ	HS-	Periodic	HS+
10	2.38	2.39	4,19
50	2.85	2.85	17.55
100	2.92	2.93	34.22

Table II gathers the homogenized thermal conductivities λ^e of the random, periodic and intermediate configurations.

TABLE II
THE EFFECTIVE THERMAL CONDUCTIVITIES λ^E [W K^{-1} m^{-1}] OF THE DIFFERENT CONFIGURATIONS FOR DIFFERENT CONTRASTS

Contrast c_λ	Random	H7	H19	H37	H61	Periodic
10	2.54	2.55	2.56	2.54	2.56	2.39
50	3.23	3.28	3.29	3.23	3.27	2.85
100	3.37	3.43	3.45	3.38	3.41	2.93

Table III and Table IV present the deviations between the intermediate configurations H7, H19, H37 and H61 and respectively the random and the periodic configurations. They also present the deviation between the periodic model and the random one. While the data indicates a slender difference between the results of the random configuration and the results of the intermediate ones, the deviation ranging from 0,09% to as little as 2,29%, it also reveals that the thermal conductivities relative to the random and intermediate configurations are significantly higher compared to those observed in the periodic scheme. At its highest point, this deviation reaches 17,81%. It is noticed that, the higher the contrast, the higher the discrepancies between the results of the different types of microstructures.

TABLE III
DEVIATION [%] OF THE EFFECTIVE THERMAL CONDUCTIVITIES OF THE DIFFERENT CONFIGURATION RELATIVE TO THE RANDOM MODEL

Contrast c_λ	H7	H19	H37	H61	Periodic
10	0.4	0.88	0.17	0.65	−6,10
50	1.51	1.93	0.09	1.12	−11.68
100	1.89	2.29	0.3	1.29	−13.17

TABLE IV
DEVIATION [%] OF THE EFFECTIVE THERMAL CONDUCTIVITIES OF THE DIFFERENT CONFIGURATION RELATIVE TO THE PERIODIC MODEL

Contrast c_λ	H7	H19	H37	H61	Random
10	6.92	7.43	6.31	7.18	6.49
50	14.94	15.41	13.33	14.5	13.23
100	17.35	17.81	15.52	16.65	15.17

The periodic model provides reliable estimates that fall within the Hashin-Shtrikman bounds. However, even at the lowest contrast, these estimates deviate from those of the random one. Consequently, it does not depict the macroscopic behavior of the random scheme accurately.

On the other hand, the intermediate configurations give results close to those of the random one, consistently for all different contrasts. This similarity in the macroscopic behavior will be further explored and exploited in the next section.

IV.2. Local Behavior

In this Section, the comparison between the different arrangements is limited to the vicinity of the test fibers. It helps to emphasize the similarities and differences, in terms of local behavior, between the 3 configurations subjected to this study. The following analysis was conducted using the results from the homogenization process carried out for all studied contrasts. However, due to the similarities in the patterns of distribution of the local fields, only the results corresponding to a contrast of 10 will be discussed. The centre of the microstructure was chosen to be the location of the test fiber considering it is the furthest point from the boundaries of the microstructure. Fig. 5 and Fig. 6 display the local thermal field maps of the random, the periodic and the intermediate configurations.

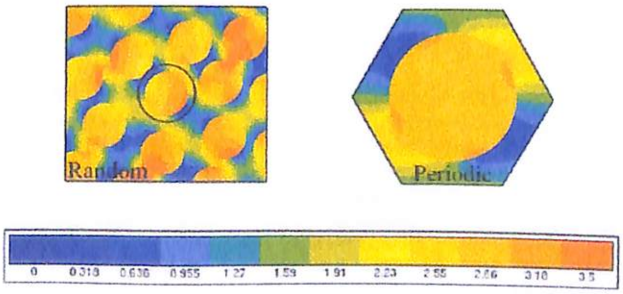

Fig. 5. Thermal field maps of the random and the periodic configurations

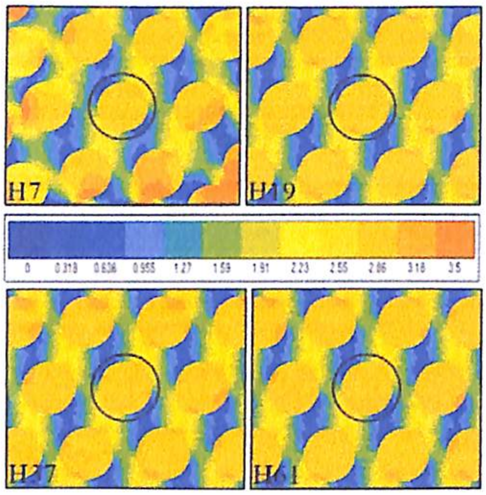

Fig. 6. Thermal field maps of the intermediate configurations

The images are centered on the test fibers surrounded with black bands. The thermal conductivity, in and around the central inclusion, reaches a maximum of 3,5 W K^{-1} m^{-1} for the random configuration, while it only reaches a maximum of 2,86 W K^{-1} m^{-1} for the H19, H37, H61 and the hexagonal configurations. A different pattern is observed in the case of H7. For the latter, the local behavior in the test fiber is the same as the one in the remaining intermediate configurations and the periodic one, but the behavior in the surrounding hexagonal ring is similar to that of the random scheme.

Upon closer examination of the random configuration, see Fig. 7, there seems to be a concentration of high tension zones with a large occurrence of the maximal value of the thermal conductivity.

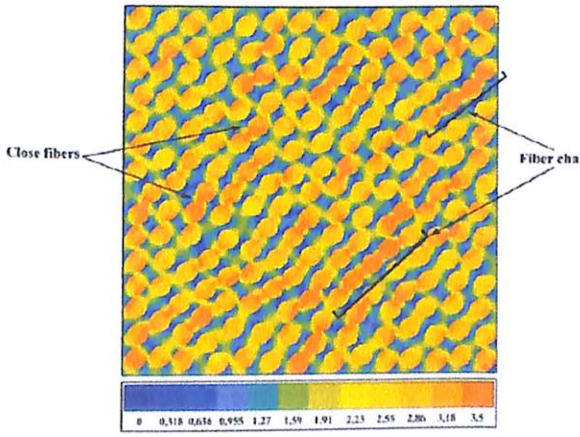

Fig. 7. Thermal field map of the random configuration

These are due to the irregular distribution of inclusions which results in the appearance of fiber chains or close fibers. In the intermediate scheme, the local behavior, in and around the test fiber, starts showing similarities to the periodic configuration with the placement of only one hexagonal outline. The periodic distribution of the inclusions widens and normalizes the fiber spacing, thus making it less likely for high tension zones to appear. Therefore, the more expanded the embedded hexagonal cell, the fewer the chances of occurrence of high property values between the fibers, which results in a lower macroscopic thermal conductivity. This explains the discrepancies between the thermal conductivity of the random configuration and the periodic one.

V. Conclusion

The comparison between the thermal behaviours of three different models of the same composite was performed. A numerical homogenization was carried out on a random, a periodic and four intermediate configurations, H7, H19, H37 and H61, of a fiber reinforced composite, and the results were analyzed from a macroscopic perspective and in terms of local behavior.

According to this study, the difference in the macroscopic thermal conductivity between the periodic configuration and the random one is around -6% for a contrast of 10 and reaches -13% for a contrast of $c_\lambda=10^2$.

This indicates that the hexagonal periodic model should only be used if a high precision in the results of homogenization for thermal properties is not required. Moreover, the intermediate configurations seem to give a more precise representation of the effective properties, with a maximum deviation of 2% from the random model. The H7, H19, H37 and H61 configurations are an intermediate form of distribution of fibers. This hybrid configuration makes it possible to compare the local behavior of the periodic and random models, and detect the source of the observed discrepancies in the effective thermal properties. On closer inspection, the local behavior in the intermediate configurations presents similarities with the random model and the periodic one.

In fact, the thermal conductivity in and around the test fibers, for the embedded cell configurations, fall into the same range as the periodic scheme, and the more expanded the periodic cell is, the more the local behavior in the outer region deviates from the local behavior observed in the random model. Consequently, while the periodic distribution facilitates the execution of the numerical homogenization, the exact same feature makes it impossible to give a highly precise representation of the effective thermal properties or to accurately portray the local behavior of the real microstructure.

References

[1] Singhal, D., Krishan, B., Shear Capacity of High Performance Steel Fiber Reinforced Concrete, (2017) *International Journal on Engineering Applications (IREA)*, 5 (3), pp. 93-101.

[2] Bey, K., Fatmi, L., Saad, S., El-Mahi, A., Effect of Different Cyclic Signals on Three-Points-Bending Behavior of a Fibreglass and Epoxy Resin Composite Materials, (2015) *International Review of Civil Engineering (IRECE)*, 6 (1), pp. 21-24.
doi: https://doi.org/10.15866/irece.v6i1.6555

[3] Mattar, I., FE Model for R.C Beams Strengthened/Retrofitted with FRP, (2015) *International Review of Civil Engineering (IRECE)*, 6 (1), pp. 10-20.
doi: https://doi.org/10.15866/irece.v6i1.6200

[4] Hashemi, S., Roach, A., A Dynamic Finite Element for Coupled Extensional-Torsional Vibration of Uniform Composite Thin-Walled Beams, (2016) *International Review of Civil Engineering (IRECE)*, 7 (4), pp. 114-124.
doi: https://doi.org/10.15866/irece.v7i4.10758

[5] R.–M. Christensen,*Mechanics of Composite Materials*, Wiley–Interscience, 1979.

[6] M. Jiang, I. Jasiuk, M. Ostoja-Starzewski, Apparent thermal conductivity of periodic two–dimensional composites, *Computational Materials Science*, Vol. 25, n. 3, pp. 329–338, 2002.

[7] M. A. A. Cavalcante, H. Khatam, M. J. Pindera, Homogenization of elastic–plastic periodic materials by FVDAM and FEM approaches - An assessment, *Composites Part B*, Vol. 42, n. 6, pp. 1713–1730, 2011.

[8] M. A. A. Cavalcante and S. P. C. Marques, Homogenization of periodic materials with viscoelastic phases using the generalized FVDAM theory, *Computational Materials Science*, Vol. 87, pp. 43–53, 2014.

[9] G. Chen, A. Bezold, C. Broeckmann, D. Weichert, On the statistical determination of strength of random heterogeneous materials, *Composite Structures*, Vol. 149, pp. 220–230, 2016.

[10] T. Leidi, G. Scocchi, L. Grossi, S. Pusterla, C. D'Angelo, J.P. Thiran and A. Ortona, Computing effective properties of random heterogeneous materials on heterogeneous parallel processors, *Computer Physics Communications*, Vol. 183, n. 11, pp. 2424–2433, 2012.

[11] D. Trias, J. Costa, J. A. Mayugo and J. E. Hurtado, Random models versus periodic models for fibre reinforced composites, *Computational Materials Science*, Vol. 38, n. 2, pp. 316–324, 2006.

[12] D. Beicha, T. Kanit, Y. Brunet, A. Imad, A. ElMoumen and Y. Khelfaoui, Effective transverse elastic properties of unidirectional fiber reinforced composites, *Mechanics of Materials*, Vol. 102, pp. 47–53, 2016.

[13] L. Bouaoune, Y. Brunet, A. El Moumen, T. Kanit and H. Mazouz, Random versus periodic microstructures for elasticity of fibers reinforced composites, *Composites Part B*, Vol. 103, pp. 68–73, 2016.

[14] M. Dong and S. Schmauder, Modelling of metal matrix composites by a self–consistent embedded cell model, *Acta Materialia*, Vol. 44, n. 6, pp. 2465–2478, 1996.

[15] M. G. Knight, L. C. Wrobel, J. L. Henshall, Micromechanical response of fibre–reinforced materials using the boundary element technique, *Composite Structures*, Vol. 62, pp. 341–352, 2003.

[16] M. Grigorovitch, E. Gal, The local response in structures using the Embedded Unit Cell Approach, *Computers and Structures*, Vol. 157, pp.189–200, 2015.

[17] N. Lippmann, T. Steinkopff, S. Schmauder and P. Gumbsch, 3D–finite–element–modelling of microstructures with the method of multiphase elements, *Computational Materials Science*, Vol. 9, pp. 28–35, 1997.

[18] T. Kanit, S. Forest, I. Galliet, V. Mounoury and D. Jeulin, Determination of the size of the representative volume element for random composites : statistical and numerical approach, *International Journal of Solids and Structures*, Vol. 40, pp. 3647–3679, 2003.

[19] T. Kanit, F. N'Guyen, S. Forest, D. Jeulin, M. Reed and S. Singleton, Apparent and effective physical properties of heterogeneous materials : representativity of samples of two materials from food industry, *Computer Methods in Applied Mechanics and Engineering*, Vol. 195, pp. 3960–3982, 2006.

[20] A. El Moumen, T. Kanit, A. Imad and H. El Minor, Effect of overlapping inclusions on effective elastic properties of composites, *Mechanics Research Communications*, Vol. 53, pp. 24–30, 2013.

[21] Y. K. Khdir, T. Kanit, F. Zaïri and M. Naït–Abdelaziz, Computational homogenization of elastic–plastic composites, *International Journal of Solids and Structures*, Vol. 50, n. 18, pp. 2829–2835, 2013.

[22] A. Benhizia, T. Kanit, T.Outtas, S. Madani and A. Imad, Computation of effective behaviour of isotropic transverse composite in non–linear problems, *Mechanics Research Communications*, Vol. 59, pp. 6–13, 2014.

[23] A. El Moumen, A. Imad, T. Kanit, E. M. Hilali and H. El Minor, A multiscale approach and microstructure design of the elastic composite behavior reinforced with natural particles, *Composites Part B*, Vol. 66, pp. 247–254, 2014.

[24] Y. Djebara, A. El Moumen, T. Kanit, S. Madani and A. Imad, 2016, Modeling of the effect of particles size, particles distribution and particles number on mechanical properties of polymer–clay nano–composites: numerical homogenization versus experimental results, *Composites Part B : Engineering*, v86, p135–142

[25] W. Kaddouri, A. El–Moumen, T. Kanit, S. Madani and A. Imad, On the effect of inclusion shape on effective thermal conductivity of heterogeneous materials, *Mechanics of Materials*, Vol. 92, pp. 28–41, 2016.

[26] M. S. Sukiman, T. Kanit, F. N'Guyen, A. Imad, A. ElMoumen and F. Erchiqui, Effective thermal and mechanical properties of randomly oriented short and long fiber composites, *Mechanics of Materials*, Vol. 107, pp. 56–70, 2017.

[27] Djeddi, F., Ghernouti, Y., Abdelaziz, Y., Experimental Investigation of FRP-Concrete Hybrid Beams, (2015) *International Review of Civil Engineering (IRECE)*, 6 (6), pp. 151-155.
doi:https://doi.org/10.15866/irece.v6i6.8187

[28] Sudarshan, N., Chandrashekar Rao, T., UHPFRC a Novel Combination Material for Blast Resistant Structures, (2017) *International Review of Civil Engineering (IRECE)*, 8 (6), pp. 277-285.
doi:https://doi.org/10.15866/irece.v8i6.12463

Authors' information

[1]Equipe de recherche Matériaux, Mécanique et Génie Civil, ENSA Agadir, Ibn Zohr University.

[2]Laboratoire de mécanique de Lille, Lille 1 University.

S. El Marzouki earned an engineering degree, in 2014, in process, energy and environmental engineering from ENSA Agadir, otherwise the National School for Applied Science, in the city of Agadirin Morocco. She is currently a doctoral candidate at the same institution, in the field ofmechanics and material science.

T. Kanit's main fields of research are Numerical Simulation in Mechanics and Mechanics of Heterogeneous Media. Dr. Kanit is an university lecturer at Université des Sciences et Technologie de Lille (Lille 1), or Lille University of Science and Technology. Dr. Kanit's research work is based at Laboratoire de Mécanique de Lille (LML), or Mechanics' Laboratory of Lille.

H. El Minor earned a doctorate in mechanics from Mohamed V university in Rabat-Morocco in 2002. Dr. El Minor is currently a professor of higher education at ENSA Agadir, or the National School for Applied Sciences of Agadir, as well as at the École Polytechnique-privée (the private polytechnic school) of Universiapolis-Agadir.

Praise Worthy Prize

International Review of Mechanical Engineering (I.RE.M.E.), Vol. 12, N. 10
ISSN 1970 - 8734 *October 2018*

Parametric Optimization of Improved Cassava Attrition Peeling Machine Using RSM Based Desirability Function

John C. Edeh, Bethrand N. Nwankwojike, Fidelis I. Abam

Abstract – *The performance of a Cassava Attrition peeling Machine was quantified and optimized using response surface methodology with mass, M_c moisture content, MC geometric mean diameter, D_g peel thickness, P_{th} of cassava tubers; number of peeling balls, n_b and peeling drum speed, N_d as factors investigated while flesh loss, peeling efficiency and throughput constitute the response variables. The experimental plan used was based on standard central composite RSM design, with a half factorial portion in which all combination of factors were at two levels. The results of the performance analyses revealed that the machine operates optimally with a throughput of 180.71kg/h, efficiency of 88.7% and 5.4% flesh loss at the determined optimal speed of the peeling drum (N_d), moisture content of the cassava(MC), mass of loaded cassava (M_c), number of peeling balls (n_b), average geometric mean diameter of the cassava tubers (D_g) and the mean peel thickness of the cassava (P_{th}) of 45rpm, 85% 82kg, 134, 48mm and 4.13mm respectively. These results improved the machine by over 60% of its throughput and 17.64% efficiency at the optimal settings of the operational parameters. The results further showed that the main effects of all the factors provided significant influence on the responses with the exception of geometric mean diameter on efficiency (hence elimination of preoperational treatment) while the factor interactions provided secondary influence. Confirmatory test of the developed RSM models revealed over 95% prediction accuracy.* ***Copyright © 2018 Praise Worthy Prize S.r.l. - All rights reserved.***

Keywords: *Attrition Peeling, Cassava Tuber, Peeling Efficiency, Response Surface Model, Throughput*

Nomenclature

RSM	Response Surface Methodology
CAPM	Cassava Attrition Peeling Machine
P_{th}	Peel thickness of the cassava, mm
D_g	Geometric mean diameter (GMD), mm
MC	Moisture content of the cassava (φ), %
n_b	Number of peeling balls
F_l	Average cassava tuber flesh loss, %
η_p	Peeling efficiency (PE), %
SE	Specific energy consumption, kJ/kg
m_{cp}	Mass of the peeled cassava
m_{pt}	Theoretical mass of peel, g
m_{pa}	Actual mass of peel, g
M_c	Mass of the loaded cassava, kg
x_1	Peeling drum speed (coded factor)
x_2	Moisture content (coded factor)
x_3	Mass of cassava (coded factor)
x_4	Number of peeling balls (coded factor)
x_5	Average geometric mean diameter (coded factor)
x_6	Peel thickness (coded factor)
a	Major diameter of tuber (Head/Proximal end), mm
b	Intermediate diameter (middle), mm
c	Minor diameter (tail/distal end), mm
M_{pc}	Weight of peel (kg) collected through the peel outlet of machine
M_{pr}	Weight of peel removed by hand after machine peeling (kg)
t	Time taken in second
P	Power consumed by the electric motor in kW
ϕ	Sphericity
DAH	Day After Harvest
T	Temperature, K
h	Humidity
n_c	Number of centre points
k	Number of factors in the design
q	Number of fractions

I. Introduction

Post-harvest processing of cassava such as harvesting, fresh tuber storage, and mechanized processing of cassava especially peeling has been established as a bottle neck in cassava production. While other cassava processing operations have been commercially mechanized successfully, peeling which entails removal of the cortex and the outer periderm layer adhering to it basically for product quality and reduction of cyanide content is yet to attain that height.

https://doi.org/10.15866/ireme.v12i10.13102

Consequently, this poses global challenge to the cassava processing sector [1]. Many innovative research works on mechanizing the peeling process were unable to exhaustively address the problem of dimensional disparities among cassava varieties which limits efficient mechanical peeling process. The existing technologies for cassava peeling can broadly be categorized as Knife edge and abrasive (attrition) cassava peeling systems. While mechanized knife peeling involves the use of single/multiple sharp edge peeling tool (knife) to remove cassava peels, abrasive (attrition) peeling exploits frictional characteristics of the rubbing surfaces to cause wear on the softer material (cassava) thereby removing the peels.

Use of abrasive drum in achieving peeling dominated most research efforts towards development of suitable peeler [2]-[8]. Articulation of good design of attrition peeler possesses high advantage of preoperational activity elimination and drastic reduction in tuber flesh loss. [9] carried out an analysis of mechanical cassava peeling using single belt systems. He also reviewed the possibilities of using an abrasive belt in cassava peeling and went further to work on achieving a constant depth of peel in the mechanical peeling of cassava in 1976 and in 1979 developed a cassava peeling machine using expanded metal lined drum and nibbling balls freely mixed with cassava to achieved peeling. This was updated to be Projects Development Agency (PRODA) model of the cassava peeling machine. [10] designed a machine that employed two parallel inclined cylinders, rotating at different speeds in the same sense, on which the cassava tubers travelled downwards under the pull of gravity. One cylinder was very rough for rotating the cassava while the other was less rough for rasping it. A free-hanging pressure device weighted each tuber onto the cylinder as it travelled down the incline. In both works there was no mention of the species of cassava used or the engineering properties that formed the basis of the design.

The problem associated with peeling in addition to morphological disparities arises from the differences in the properties of the cassava peel, which varies in thickness, texture, and strength of adhesion to the root flesh. Thus, cassava peeling machine development requires good background knowledge of some engineering properties of cassava tubers to improve on the capacities and efficiencies so as to eliminate pre-operational treatments of trimming, sorting and grading which characterises the existing peelers. Indeed the development of a technically and economically acceptable cassava peeling machine as a challenge prompted designed modification and development of a cassava attrition peeling machine which is an improved model of the existing PRODA machine. Comparative assessment after the modification of an existing cassava attrition peeler by introduction of egg shaped peeling balls, breaker baffles and inner drum surface perforations showed increased peeling efficiency, reduction in flesh loss, processing time and cost.

However, the performance testing indicated that some crop and operational parameters such as peel thickness, moisture content, geometric mean diameter, mass of cassava and machine speed affects the performance parameters identified as peeling efficiency, flesh loss, throughput capacity and specific energy consumption of the Cassava attrition peeling machine significantly. In spite of the attempts made in development of modified peeling technology, it is still desired that the machine operates with maximum efficiency and throughput at minimal flesh loss and specific energy consumption obtainable hence the need to pay much attention to optimal settings of these operational parameters for optimized responses.

Response surface methodology was therefore investigated to be suitable for an empirical optimization problem of this nature where varying input combinations relates to multiple desired levels of product characteristics. In addition, the technique involves special experimental designs/optimization tactic with small number of experimental runs to save time and cost [11], [12]. This Response surface methodology as a collection of mathematical and statistical techniques useful for the modelling and analysis of problems has the objective of optimizing the response of interest influenced by several variables [13]. Its application involves design of experiment (approximate choice of response surface design), fitting of models, selection and validation, and optimization. [14], [15] and [16] maintained that prediction equations and optimal operational parameter settings determined from response surface technique are always or nearly close to the optimal operating condition of the real system. [12] further revealed that practical interpretation of optimization results determined using RSM are not usually affected by small discrepancies due to inability of experimenter to determine the exact factor level.

There are remarkable instances of outstanding contribution of RSM. With the application of RSM, [17] were able to quantify and optimize the effect of feed rate, cutting speed cutting edge angle on the surface roughness and tangential force when turning AISI 1045 steel at 97.2% prediction while [18] had earlier developed a response surface model that functionally relates sensitivity of an airplane wing crack detector to number of turns, winding distance and wire gauge as well as determining the settings of the variables that maximizes the sensitivity from the model at above 95% prediction. Also in NIST Physics Laboratory RSM was used to determine the best setting of seven factors that maximizes somoluminscent light intensity [11] and 98% success was achieved with RSM in optimization of mechanical clothing tactile comfort [19]. Furthermore, and recently [12] quantified and optimized using response surface analysis three performance/response variables (efficiency, throughput and specific energy of consumption) of a palm nut-pulp separating machine at optimal settings of four factors (driving power, cake breaker speed, auger speed and helix angle) within 95%

Consequently, this poses global challenge to the cassava processing sector [1]. Many innovative research works on mechanizing the peeling process were unable to exhaustively address the problem of dimensional disparities among cassava varieties which limits efficient mechanical peeling process. The existing technologies for cassava peeling can broadly be categorized as Knife edge and abrasive (attrition) cassava peeling systems. While mechanized knife peeling involves the use of single/multiple sharp edge peeling tool (knife) to remove cassava peels, abrasive (attrition) peeling exploits frictional characteristics of the rubbing surfaces to cause wear on the softer material (cassava) thereby removing the peels.

Use of abrasive drum in achieving peeling dominated most research efforts towards development of suitable peeler [2]-[8]. Articulation of good design of attrition peeler possesses high advantage of preoperational activity elimination and drastic reduction in tuber flesh loss. [9] carried out an analysis of mechanical cassava peeling using single belt systems. He also reviewed the possibilities of using an abrasive belt in cassava peeling and went further to work on achieving a constant depth of peel in the mechanical peeling of cassava in 1976 and in 1979 developed a cassava peeling machine using expanded metal lined drum and nibbling balls freely mixed with cassava to achieved peeling. This was updated to be Projects Development Agency (PRODA) model of the cassava peeling machine. [10] designed a machine that employed two parallel inclined cylinders, rotating at different speeds in the same sense, on which the cassava tubers travelled downwards under the pull of gravity. One cylinder was very rough for rotating the cassava while the other was less rough for rasping it. A free-hanging pressure device weighted each tuber onto the cylinder as it travelled down the incline. In both works there was no mention of the species of cassava used or the engineering properties that formed the basis of the design.

The problem associated with peeling in addition to morphological disparities arises from the differences in the properties of the cassava peel, which varies in thickness, texture, and strength of adhesion to the root flesh. Thus, cassava peeling machine development requires good background knowledge of some engineering properties of cassava tubers to improve on the capacities and efficiencies so as to eliminate pre-operational treatments of trimming, sorting and grading which characterises the existing peelers. Indeed the development of a technically and economically acceptable cassava peeling machine as a challenge prompted designed modification and development of a cassava attrition peeling machine which is an improved model of the existing PRODA machine. Comparative assessment after the modification of an existing cassava attrition peeler by introduction of egg shaped peeling balls, breaker baffles and inner drum surface perforations showed increased peeling efficiency, reduction in flesh loss, processing time and cost.

However, the performance testing indicated that some crop and operational parameters such as peel thickness, moisture content, geometric mean diameter, mass of cassava and machine speed affects the performance parameters identified as peeling efficiency, flesh loss, throughput capacity and specific energy consumption of the Cassava attrition peeling machine significantly. In spite of the attempts made in development of modified peeling technology, it is still desired that the machine operates with maximum efficiency and throughput at minimal flesh loss and specific energy consumption obtainable hence the need to pay much attention to optimal settings of these operational parameters for optimized responses.

Response surface methodology was therefore investigated to be suitable for an empirical optimization problem of this nature where varying input combinations relates to multiple desired levels of product characteristics. In addition, the technique involves special experimental designs/optimization tactic with small number of experimental runs to save time and cost [11], [12]. This Response surface methodology as a collection of mathematical and statistical techniques useful for the modelling and analysis of problems has the objective of optimizing the response of interest influenced by several variables [13]. Its application involves design of experiment (approximate choice of response surface design), fitting of models, selection and validation, and optimization. [14], [15] and [16] maintained that prediction equations and optimal operational parameter settings determined from response surface technique are always or nearly close to the optimal operating condition of the real system. [12] further revealed that practical interpretation of optimization results determined using RSM are not usually affected by small discrepancies due to inability of experimenter to determine the exact factor level.

There are remarkable instances of outstanding contribution of RSM. With the application of RSM, [17] were able to quantify and optimize the effect of feed rate, cutting speed cutting edge angle on the surface roughness and tangential force when turning AISI 1045 steel at 97.2% prediction while [18] had earlier developed a response surface model that functionally relates sensitivity of an airplane wing crack detector to number of turns, winding distance and wire gauge as well as determining the settings of the variables that maximizes the sensitivity from the model at above 95% prediction. Also in NIST Physics Laboratory RSM was used to determine the best setting of seven factors that maximizes somolumiscent light intensity [11] and 98% success was achieved with RSM in optimization of mechanical clothing tactile comfort [19]. Furthermore, and recently [12] quantified and optimized using response surface analysis three performance/response variables (efficiency, throughput and specific energy of consumption) of a palm nut-pulp separating machine at optimal settings of four factors (driving power, cake breaker speed, auger speed and helix angle) within 95%

prediction interval. Thus, this study exploits the outstanding advantages of response surface modelling and optimization for determination of optimal operational parameter of a modified cassava attrition peeling machine.

II. Materials and Methods

The cassava attrition peeling machine shown in Figs. 1 comprises the peeling unit, discharging unit, water sprinkler mechanism, prime mover (electric motor) and peeling balls. The peeling drum chamber consist mainly of a rolled perforated aluminum plate formed into a cylindrical drum and centrally mounted through a mild steel shaft on two bearing supports. Three angular aluminum bars are welded to the inner surface of the drum. The bars are equidistantly spaced acting as breaker baffles to check centrifugal effect thereby extending sticking speed (limiting speed). The perforations (16mm hole) were made at regular interval such that its embossments enhance the frictional characteristics of the inner drum surface.

The peeling drum together with the egg shaped peeling balls provides the requisite surface characteristics and frictional properties for attrition. The drum is partially immersed in water bath/trough. A discharge plug on the trough is situated beneath the peeling drum to evacuate the peel flake and waste water.

Cassava tubers are manually introduced into the peeling drum with peeling balls through the door slit provided when the drum is stationary prior to peeling.

The peeling drum is operated at speeds less than the sticking speed of 49rpm which is achieved by coupling a variable speed reducer (variac) to the electric motor through belt and pulley mechanism. In each batch operation, cassava of known mass and biomaterial properties are loaded into the peeling drum and the combined rotary action of the cassava on the peeling drum when the machine is actuated causes peeling due to attrition. Introduction of egg shaped peeling balls ensures that every section of the loaded cassava is peeled during the mechanical agitation irrespective of its geometry.

Peeling efficiency, flesh loss, throughput, and specific energy consumption are the performance parameters of the modified cassava attrition peeling machine studied.

Where flesh loss is the amount of starchy flesh removed alongside the peels during peeling; peeling efficiency is the ratio of the total mass of peel by the machine to mass of manual peel while its throughput is the total mass of cassava peeled and discharged by the machine per unit time. Specific energy consumption of the machine is quantity of energy it used to peel a unit mass of cassava fed into it. The crop and operational parameters of the machine whose setting affect the response parameters (performance parameters) include mass of loaded cassava (M_c), average geometric mean diameter of the cassava tubers (D_g), moisture content of the cassava (MC), the mean peel thickness of the cassava (P_{th}), number of peeling balls (n_b) and speed of the peeling drum (N_d).

Their design values were 80kg, 48mm, 70%Wb, 3.5mm, 105 and 40 rpm, respectively.

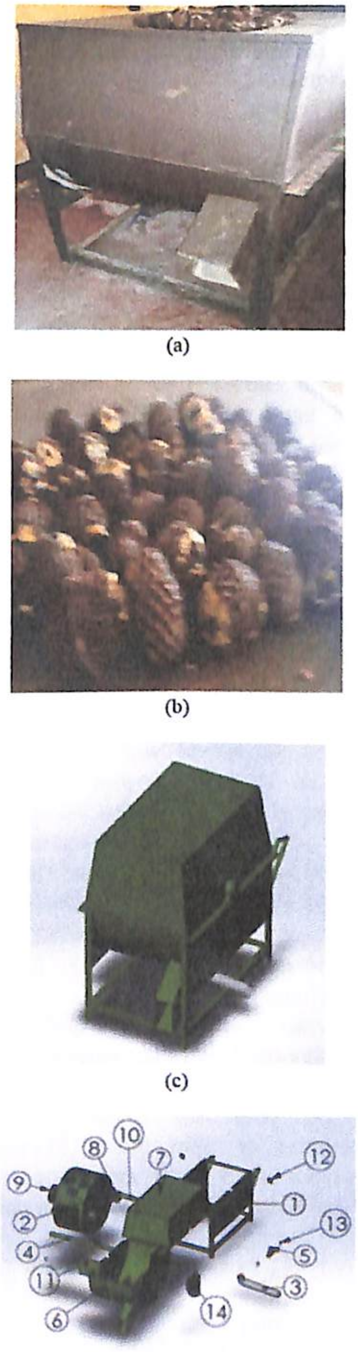

Figs. 1. (a) Modified CAPM (b) Peeling Balls, (c) Isometric View of Modified CAPM (d) Exploded view: 1. Structural Frame, 2. Peeling drum, 3. Discharge pipe, 4. Shaft, 5. Bearing, 6. Water bath(trough), 7. Covering hood, 8. Electric motor, 9. pulley, 10. Motor shaft, 11. Loading cover, 12. Hinges, 13. Bolt, 14. Discharge slit

II.1. Experimental Design/Procedure

The relationship between the performance parameters (responses) of a cassava attrition peeling machine and its operational parameters (factors) and determination of the optimal settings of the parameters was investigated using response surface analysis. This involved the design and development of the response surface experiment, model fitting, selection and optimization of the best response surface functions for the responses. The choice of the type of experimental design was based on the aim of the study, number of available variables, availability of resources, sources of data collection, time and cost implication. The response variables investigated were the flesh loss (F_l), peeling efficiency (η_p), throughput capacity (TP) and specific energy consumption (SE). The speed of the peeling drum (N_d), moisture content of the cassava (MC), mass of loaded cassava (M_c), number of peeling balls (n_b), geometric mean diameter (D_g) and peel thickness (P_{th}) coded as x_1, x_2, x_3, x_4, x_5 and x_6 respectively, constitute the factors. Where moisture content is dependent on variety [20], period of harvest and day after harvest (DAH) [1] and it is determined by Equation (1) developed from [21], [22] and [23]:

$$\varphi_c = e^{-(xt^y)}\left[\varphi_i - 0.01Ae^{Bc}\right] + 0.01Ae^{Bc} \quad (1)$$

where φ_c and φ_i are the moisture content and initial moisture content of cassava after harvest, given by [24] as:

$$\varphi_i = \frac{W_w - W_d}{W_w} \times \frac{100}{1} \quad (2)$$

W_w=weight of wet sample (g),' W_d=weight of dried sample (g):

$$x = 0.026 - 0.0045h + 0.01215T \quad (3)$$

$$y = 0.013362 + 0.194h - 0.00017h^2 + 0.009468T \quad (4)$$

T and h are air temperature and relative humidity:

$$A = 727.44h + 599.9h^2 + 475.64h^3 \quad (5)$$

$$B = -0.0143 - 0.0771h + 0.132h^2 - 0.157h^3 - 0.0731h^4 \quad (6)$$

$$c = (T + 81.64) \quad (7)$$

Geometric mean diameter (GMD), D_g is a dimensional property that takes care of the variation in the tuber thickness along the full length. It has also been investigated by Nwachukwu et al. (2015) to be a characteristic property of cassava tuber variety. Mean value of GMD accounts for the morphological disparities in cassava tuber during evaluation. For the unpeeled tubers is calculated using the formula below as seen from [25]:

$$GMD = D_g = (a \times b \times c)^{1/3} \quad (8)$$

where GMD is the Geometric mean diameter (mm), a (head) is the major diameter (mm), b (middle) is the intermediate diameter (mm), c (tail) is the minor diameter(mm). In this investigation, MINITAB (version 17) software has been used at first to generate and randomize a thirty four (34) runs with all combination of the six factors at two coded levels (+1 and -1) half factorial design layout (2^{k-q}) in which "+1"and "-1" indicate the high and low level of the factors respectively with "0" as the midpoint of the factors. The search for models that will describe the responses adequately started with fitting of linear function because of the desire to quantify the parameters with simplest possible functions.

However, the main effects plots, model adequacy measures and residual diagnostic plots displayed by the software along with the fitted linear models were used to evaluate the functions but did not approximate the true responses adequately hence a second order model was sought for. Here the initial two level half-fractional factorial designs were augmented by the addition of more centre points and axial points totalling fifty four (54) experimental runs with an axial point value of (±2.366) which allowed analysis of curvature and second order interactions of the initial two level designs. The second order response surface design table for the modified Cassava Attrition Peeling Machine for the study is given in Table I. The limits of the operational factors (Table II) been investigated were determined from experimental tests of factor variations with performance parameters. The actual high and low levels for each factor was selected based on non-variation of the responses or indicated asymptote behavior of the responses before or after some combination of the variables. In each of the tests for the determination of the actual levels for any of the factors, the other five factors were kept constatnt at their design values. Flesh loss, peeling efficiency, throughput and specific energy consumption of the machine were evaluated at each combination of the variables by feeding a known mass of cassava tubers into the machine for peeling. After each operation, the peeling time involved was taken using stop watch and the peeled cassava weighed using electronic digital balance. Equations (9)-(12) were used to compute the four performance parameters from experimental results of their variations and plotted as shown in Figs. 2-7:

$$F_l = M_c - (m_{cp} + m_{pt}) \quad (9)$$

$$\eta_p = \frac{M_{Pc}}{M_{pr} + M_{pc}} \times \frac{100}{1} \quad (10)$$

$$TP = \frac{M_c}{t} \quad (11)$$

$$SE = \frac{P\,t}{M_c} \quad (12)$$

where m_{cp} is the mass of the peeled cassava; m_{pt} is the theoretical mass of peel; M_c is the mass of the loaded cassava; t is Time taken in second and P is Power consumed by the electric motor in kW. Thereafter, the natural values of these responses were determined using the general transformation equation (13) as equations (14)-(19). Each equation relates the coded and actual values of the factors. Here x is the independent variable in natural units; X_i is the coded variable while x_{max} and x_{min} are the maximum and minimum values of the independent variables respectively:

$$X_i = \frac{x - \left(\frac{x_{max} + x_{min}}{2}\right)}{\left(\frac{x_{max} - x_{min}}{2}\right)} \quad (13)$$

$$x_1 = \frac{N_d - 30}{10} \quad (14)$$

$$x_2 = \frac{MC - 72.5}{12.5} \quad (15)$$

$$x_3 = \frac{M - 50}{15} \quad (16)$$

$$x_4 = \frac{n_b - 70}{30} \quad (17)$$

$$x_5 = \frac{D_g - 49}{19} \quad (18)$$

$$x_6 = \frac{P_{th} - 3.25}{1.25} \quad (19)$$

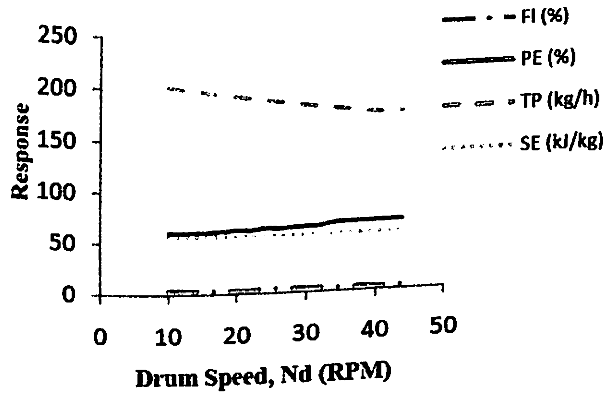

Fig. 2. Variation of speed of the drum against the Responses

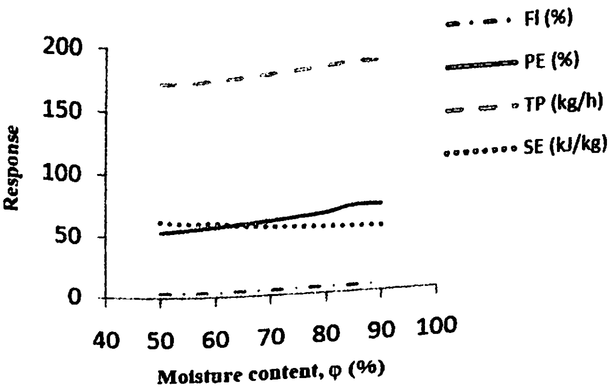

Fig. 3. Variation of Moisture Content against the Responses

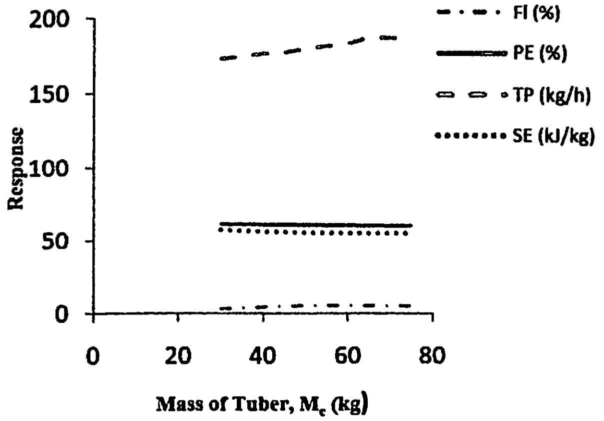

Fig. 4. Variation of Mass of cassava tubers (M_t) against the Responses

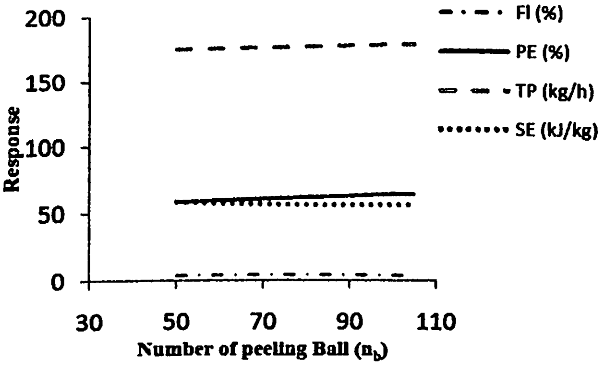

Fig. 5. Variation of Number of peeling balls (n_b) against the Responses

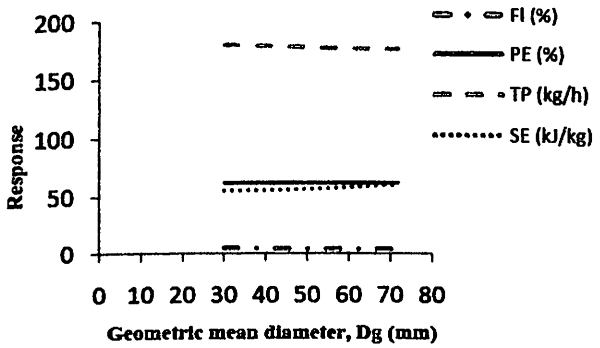

Fig. 6. Variation of GMD (d_g) against the Responses

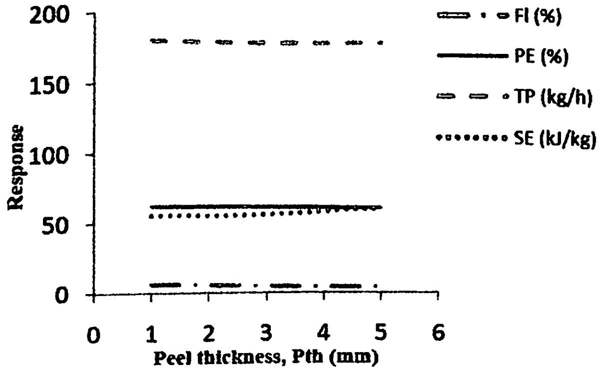

Fig. 7. Variation of Peel thickness (P_{th}) against the Responses

TABLE I
RSM DESIGN TABLE FOR THE MODIFIED CAPM STUDY

Experimental runs		coded values of factors					
StdOrder	RunOrder	x_1	x_2	x_3	x_4	x_5	x_6
16	1	1	1	-1	1	1	-1
19	2	0	0	0	0	0	0
18	3	0	0	0	0	0	0
1	4	-1	-1	-1	-1	-1	-1
13	5	-1	-1	-1	1	1	-1
5	6	-1	-1	1	1	-1	-1
4	7	1	1	-1	-1	-1	-1
9	8	-1	-1	1	-1	1	-1
8	9	1	1	1	1	-1	-1
14	10	1	-1	-1	1	1	1
11	11	-1	1	1	-1	1	1
7	12	-1	1	1	1	-1	1
17	13	0	0	0	0	0	0
12	14	1	1	1	-1	1	-1
15	15	-1	1	-1	1	1	1
10	16	1	-1	1	-1	1	1
2	17	1	-1	-1	-1	-1	1
3	18	-1	1	-1	-1	-1	1
6	19	1	-1	1	1	-1	1
20	20	0	0	0	0	0	0
49	21	0	0	0	0	-2.366	0
53	22	0	0	0	0	0	0
41	23	-2.366	0	0	0	0	0
47	24	0	0	0	-2.366	0	0
45	25	0	0	-2.366	0	0	0
42	26	2.366	0	0	0	0	0
52	27	0	0	0	0	0	2.366
48	28	0	0	0	2.366	0	0
43	29	0	-2.366	0	0	0	0
51	30	0	0	0	0	0	-2.366
44	31	0	2.366	0	0	0	0
46	32	0	0	2.366	0	0	0
50	33	0	0	0	0	2.366	0
54	34	0	0	0	0	0	0
37	35	0	0	0	0	0	0
30	36	1	-1	-1	-1	1	-1
26	37	1	-1	-1	1	-1	-1
28	38	1	1	-1	1	-1	1
21	39	-1	-1	1	-1	-1	1
31	40	-1	1	-1	-1	1	-1
25	41	-1	-1	-1	1	-1	1
40	42	0	0	0	0	0	0
38	43	0	0	0	0	0	0
35	44	-1	1	1	1	1	-1
33	45	-1	-1	1	1	1	1
39	46	0	0	0	0	0	0
36	47	1	1	1	1	1	1
27	48	-1	1	-1	1	-1	-1
22	49	1	-1	1	-1	-1	-1
34	50	1	-1	1	1	1	-1
24	51	1	1	1	-1	-1	1
32	52	1	1	-1	-1	1	1
29	53	-1	-1	-1	-1	1	1
23	54	-1	1	1	-1	-1	-1

The model adequacy measures used for the statistical verification of the fitted functions include regression analysis of model coefficients, analysis of variance (ANOVA) [28][29] and lack-of-fit tests whilst residual diagnostic plots contains normal probability plots of the residuals, histogram of residuals, dot plots of the residuals versus observation order and that of residuals versus fitted response.

The coefficient of determination, R^2 and adjusted coefficient of determination, adj-R^2 of the response models were determined to know how properly the models fitted the measured data.

TABLE II
LIMITS OF THE CASSAVA ATTRITION PEELING MACHINE OPERATIONAL PARAMETERS

S/N	Factor Description	Factor symbol		Factor Value	
		Coded	Actual	High (+1)	Low (-1)
1	Speed of Drum (rpm)	X_1	N_d	20	40
2	Cassava moisture content (%wb)	X_2	MC	60	85
3	Mass of Cassava (kg)	X_3	M_c	35	65
4	Number of peeling balls	X_4	n_b	50	100
5	Geometric mean diameter (mm)	X_5	d_g	30	68
6	Peel thickness (mm)	X_6	P_{th}	20	45

The values of R^2 lie between the zero and one (i.e. 0% $\leq R^2 \leq$ 100%) and the more the value of R^2 approaches one (1), the better the estimated model fits the data.

Residual is the difference between the respective observed responses and their model predicted values.

If a model is adequate, the points on the normal probability plots of the residuals should form a straight line.

Small departure from the line in the normal probability plot is common, but a clearly "S" shaped curve indicates bimodal distribution of the residuals.

Breaks near the middle of this graph are also indications of abnormalities in the residual distribution.

The plots of the residuals versus run order and that of residuals versus fitted response should exhibit scatter feature without any obvious pattern (i.e. structureless) while histogram of the residuals is expected to portray dumb-bell shape.

The significance of each model term was analyzed using the t -statistics. If $|T|_{cal} > T_{tab}$, then the corresponding factor or term is said to be statistically significant and T_{tab} is obtained using statistical table.

The analysis of variance was employed in testing the adequacy of the fitted models to be true approximations of the measured data.

If the calculated value of F-statistic (F_{cal}) for each of the fitted models exceed the tabulated value of F-statistic (F_{tab}) i.e $F_{cal} > F_{tab}$ and $P - val < \alpha$, the fitted models are said to be adequate approximation of the data for the performance parameters of the CAPM, however if reverse of the above statement is the case; $F_{cal} < F_{tab}$ and $P - val > \alpha$, then the models are inadequate to fit the data.

The models lack of fit test was also conducted to check the goodness of fit of the predicted models for the measured data. If the calculated value of $F - statistic\ (F_{calLOF})$ for each of the fitted models exceed the tabulated value of $F - statistic\ (F_{tabLOF})$ i.e $F_{calLOF} > F_{tabLOF}$ and $P - val < \alpha$, the fitted models are said to exhibit insignificant lack of fit for the fitted data of the performance parameters of the cassava attrition peeling machine, however if reverse of the above statement is the case; $F_{calLOF} < F_{tabLOF}$ and $P - val > \alpha$, then the models are said to exhibit significant lack of fit.

The residual analysis of the models was conducted graphically and statistical significance of each model term was tested at 95% significance level. Insignificant terms were eliminated from the models using stepwise model building approach.

The confirmation trials were conducted using the same procedure as in the determination of the factor levels.

The flesh loss, peeling efficiency, throughput and specific energy consumption of the machine were predicted based on various factor combinations of confirmation experimental plan using point prediction capability of MINTAB. When the models have been fully validated, optimal settings of all responses and factors were determined.

Optimization using the contour and surface plots were used to estimate the optimal relationship between each of the responses and any combination of the factors.

Only statistically significant terms obtained using the interaction plots were considered and the topography of each response surface plot indicates the effect each factor pair has on the response with other factors kept constant.

A multiple response optimization model was formulated using Desirability function approach. The coded solution (optimum coded factor levels) obtained were then compared with the ones obtained graphically before the actual optimal settings of the operational parameters of the machine were derived and established using the transformations.

III. Result and Discussion

The result of the experimental runs on the experimental plan for factor combination is given in Table III.

The second order model for predicting flesh loss (*Fl*), peeling efficiency (η_p), throughput capacity (*TP*) and specific energy consumption (*SE*) with the actual values of the modified cassava attrition peeling machine responses in their original/natural units are given by equations (20)-(23):

$$\begin{aligned} F_l = 5.00 &+ 0.1781N_d - 0.4549MC + 0.5389M_c \\ &- 0.0280n_b + 0.0175D_g \\ &+ 1.485P_{th} - 0.003851{N_d}^2 \\ &+ 0.002229MC^2 - 0.003170{M_c}^2 \\ &- 0.000959{n_b}^2 + 0.000522{D_g}^2 \\ &+ 0.1777{P_{th}}^2 - 0.001067N_dM_c \\ &+ 0.001079N_dD_g \\ &- 0.01850N_dP_{th} \\ &+ 0.002188MCn_b \\ &- 0.000832MC\,D_g \\ &- 0.001024M_CD_g \\ &- 0.02697M_CP_{th} \\ &+ 0.00794n_bP_{th} - 0.01208D_gP_{th} \end{aligned} \tag{20}$$

$$\begin{aligned} \eta_p = 47.28 &- 0.4546N_d + 0.0650MC + 0.0097M_c \\ &+ 0.1463n_b - 0.0370D_g \\ &+ 0.543P_{th} + 0.001292{N_d}^2 \\ &+ 0.001278MC^2 \\ &+ 0.002108N_dMC \\ &+ 0.001793MC\,D_g \\ &- 0.01405M_CP_{th} \\ &- 0.000593n_bD_g \\ &+ 0.01303n_bP_{th} \\ &- 0.001714D_gP_{th} \end{aligned} \tag{21}$$

$$\begin{aligned} TP = 222.07 &- 1.803N_d - 0.307MC + 0.6104M_c \\ &- 0.1745n_b - 0.2071D_g \\ &- 6.241P_{th} + 0.00353{N_d}^2 \\ &+ 0.002542MC^2 + 0.000605{D_g}^2 \\ &+ 0.3114{P_{th}}^2 + 0.00840N_dMC \\ &+ 0.001809N_dD_g \\ &- 0.003867MC\,M_c \\ &+ 0.003640MCn_b \\ &- 0.001105MCD_g \\ &- 0.001294M_CD_g \\ &+ 0.03067M_CP_{th} \\ &+ 0.04632D_gP_{th} \end{aligned} \tag{22}$$

$$\begin{aligned} SE = 105.87 &- 0.0805N_d - 0.4816MC \\ &- 0.1842M_c - 0.2030n_b \\ &- 0.0958D_g - 6.288P_{th} \\ &+ 0.001340{N_d}^2 + 0.003458MC^2 \\ &+ 0.001608{M_c}^2 + 0.001293{n_b}^2 \\ &+ 0.003229{D_g}^2 + 0.8032{P_{th}}^2 \\ &- 0.00528MCn_b \\ &- 0.001050MC\,D_g \\ &- 0.000592M_CD_g \\ &+ 0.00466n_bP_{th} \end{aligned} \tag{23}$$

The adequacy of the models to fit the measured operational parameter was shown by the residual plots (Figs. 12-15) and coefficient of determination (Table IV).

Test of significance of individual terms in the models carried out showed 95% significance level with the value of T_{tab} obtained using statistical tables as 2.052. Individual terms in the model statistically insignificant to the responses as $P - val > 0.05$ were eliminated from the model given rise to the model equation 20- 23.

Evaluation of the coefficient of determination and error standard deviation of these second order models (Table IV) indicates that the second order models fit the data since the values of 'R^2', '*adj-* R^2' and'*S*' met the conditions in each model as evident in table 4 and hence it was deduced that the interaction and square terms improved the adequacy of the models. Survey of main effects plot, Figs. 8-11 show that all factors had either positive or negative effect on the response variables (as indicated by the angle it makes with the horizontal) except for geometric mean diameter and peel thickness on peeling efficiency.

TABLE III
RSM TABLE FOR SECOND ORDER MODEL OF THE MACHINE

experimental runs		coded values of factors						Responses			
StdOrder	RunOrder	x_1	x_2	x_3	x_4	x_5	x_6	flesh loss	P. effy	TP	SE
16	1	1	1	-1	1	1	-1	2.79	71.8	181.5	65.2
19	2	0	0	0	0	0	0	6.195	64.5	186.5	59
18	3	0	0	0	0	0	0	5.7	64.5	184.5	58.5
1	4	-1	-1	-1	-1	-1	-1	5.16	59.7	190	64
13	5	-1	-1	-1	1	1	-1	3.5	66	186.5	67.42
5	6	-1	-1	1	1	-1	-1	7.39	66	204	61.5
4	7	1	1	-1	-1	-1	-1	1.75	63	180	63
9	8	-1	-1	1	-1	1	-1	6.8	58.5	194.5	67.7
8	9	1	1	1	1	-1	-1	6.07	71.5	195	59
14	10	1	-1	-1	1	1	1	3.85	62.1	168.5	65.6
11	11	-1	1	1	-1	1	1	4.55	66.6	200.5	63
7	12	-1	1	1	1	-1	1	10.9	76	210	58.4
17	13	0	0	0	0	0	0	6.5	64.22	187	59
12	14	1	1	1	-1	1	-1	3.25	64.52	182.8	65.5
15	15	-1	1	-1	1	1	1	7.07	76.5	195.9	63.8
10	16	1	-1	1	-1	1	1	3.9	50.89	177.2	65.74
2	17	1	-1	-1	-1	-1	1	5.1	54.5	165	62.07
3	18	-1	1	-1	-1	-1	1	7	68.2	191.5	61
6	19	1	-1	1	1	-1	1	6.6	62	179.5	60
20	20	0	0	0	0	0	0	6.5	63.82	185	59
49	21	0	0	0	0	-2.366	0	10	64.61	190	60
53	22	0	0	0	0	0	0	5.7	65	186.5	58.5
41	23	-2.366	0	0	0	0	0	6.7	70.17	208.5	60
47	24	0	0	0	-2.366	0	0	2.5	55	180	65
45	25	0	0	-2.366	0	0	0	0.1451	65	173	63
42	26	2.366	0	0	0	0	0	1.38	60.5	167.5	59.45
52	27	0	0	0	0	0	2.366	10.5	64	188	64
48	28	0	0	0	2.366	0	0	3.18	73.6	192.5	62
43	29	0	-2.366	0	0	0	0	8	53.7	179	64
51	30	0	0	0	0	0	-2.366	5	64.5	189.5	68
44	31	0	2.366	0	0	0	0	8.29	77.76	197.5	60
46	32	0	0	2.366	0	0	0	4.26	63.86	199.7	59
50	33	0	0	0	0	2.366	0	4.5	65	184.5	71
54	34	0	0	0	0	0	0	5.7	65	184.97	59
37	35	0	0	0	0	0	0	6	65	186	59.18
30	36	1	-1	-1	-1	1	-1	3.35	54.5	165	69
26	37	1	-1	-1	1	-1	-1	2.1	61.5	170	63
28	38	1	1	-1	1	-1	1	7	73.5	182	59.49
21	39	-1	-1	1	-1	-1	1	9.6	58	200	60
31	40	-1	1	-1	-1	1	-1	1.75	70	190	67.07
25	41	-1	-1	-1	1	-1	1	7.7	69	187	60.5
40	42	0	0	0	0	0	0	7	65	186.5	59
38	43	0	0	0	0	0	0	5.72	65	187.1	59.5
35	44	-1	1	1	1	1	-1	5.96	76	203.6	63
33	45	-1	-1	1	1	1	1	6.5	65	200	64
39	46	0	0	0	0	0	0	6.9	65.13	185	59
36	47	1	1	1	1	1	1	4.55	70.5	190	61
27	48	-1	1	-1	1	-1	-1	5.27	75.8	202.5	60.5
22	49	1	-1	1	-1	-1	-1	5.5	53.7	182	62.97
34	50	1	-1	1	1	1	-1	3.65	59.5	177	65.5
24	51	1	1	1	-1	-1	1	4.55	63	186	60.15
32	52	1	1	-1	-1	1	1	2.68	65	173.5	65.1
29	53	-1	-1	-1	-1	1	1	6.83	57.7	183.5	67.19
23	54	-1	1	1	-1	-1	-1	7.15	66.5	204.5	62

The implication is that peeling efficiency is not dependent on tuber sizes hence requiring no initial treatment of trimming, sorting and grading of cassava tubers prior to peeling operation which is one of the major advantages of this design over existing ones. The second order terms improved the adequacy of the models and the plots of the normal probability tend to fall in a straight line and the histogram gives the required dumb bell shape. Hence, the second order models are adequate to statistically fit the data with little outliers and reduced skewness. The plots of the model confirmatory test and residual plots shown in Figs. 12-15 indicate that the fitted functions are good fits for the machine responses (since predicted approximates actual, points align to straight line of normal probability curve, no definite pattern of scattered plot and dumbbell nature of the histogram).

TABLE IV
COEFFICIENTS OF DETERMINATION AND ERROR STANDARD DEVIATION FOR THE SECOND ORDER MODELS

Responses	S	R-sq	R-sq(adj)
F_l (kg)	0.497383	97.71	95.34
η_p(%)	0.578916	99.57	99.13
TP (kg/hr)	1.03577	99.54	99.07
SE (kJ/kg)	0.397441	99.25	98.46

These therefore, can be used for optimization of the machine with the predicted values having a percentage error of plus and minus five percent (±5%). The contour and response surface plots shown in Figs. 16-22 are used to explore and optimize the potential relationship between the two factor pair on the response.

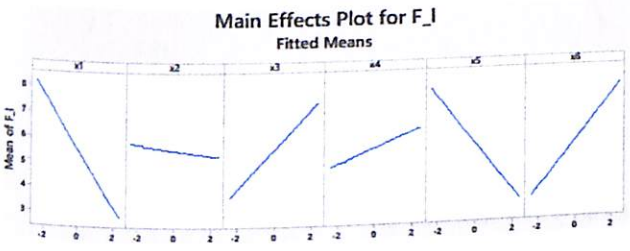

Fig. 8. Main effects Plots of the flesh loss

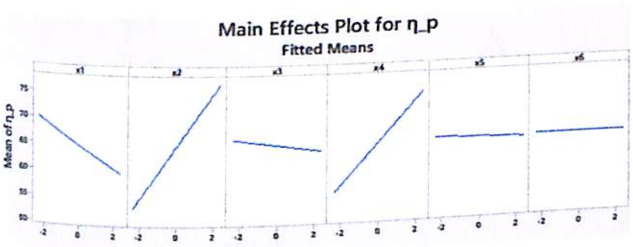

Fig. 9. Main effects plot of the peeling efficiency

The contour plots represented with contour lines provides a two dimensional view of the surface where the points that have the same response are connected to produce contour lines of constant responses. The predictors are plotted in the x- axis and y- axis while the response variable is represented in the z- axis.

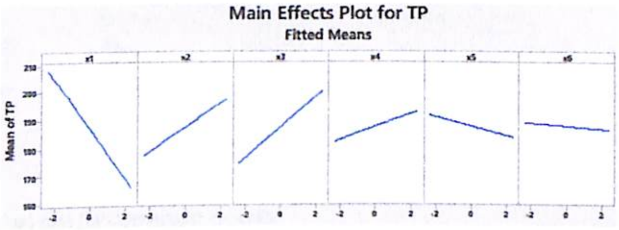

Fig. 10. Main effects plots of the throughput capacity

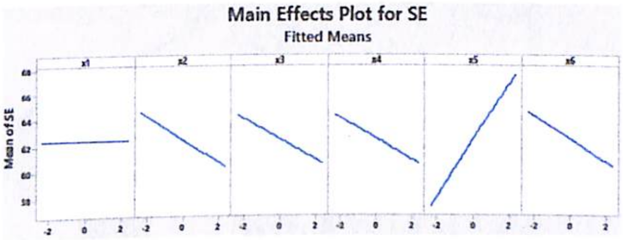

Fig. 11. Main effects plot of the specific energy consumption

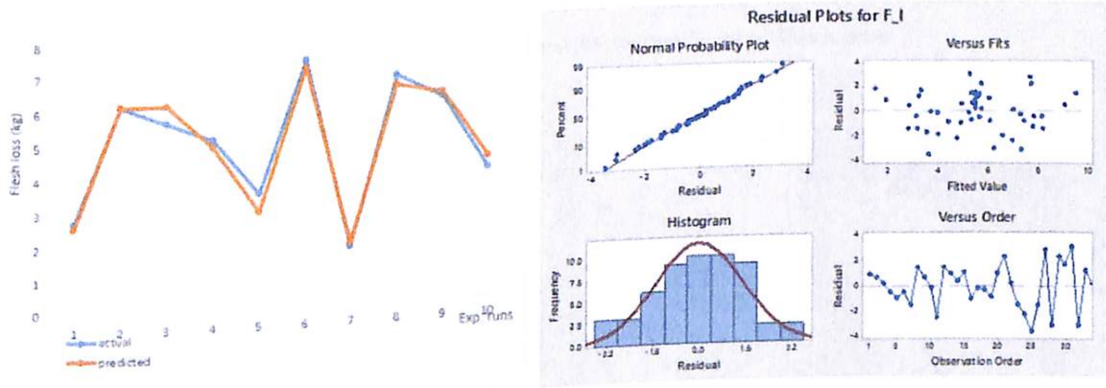

Fig. 12. Confirmatory test and Residual plot for flesh loss

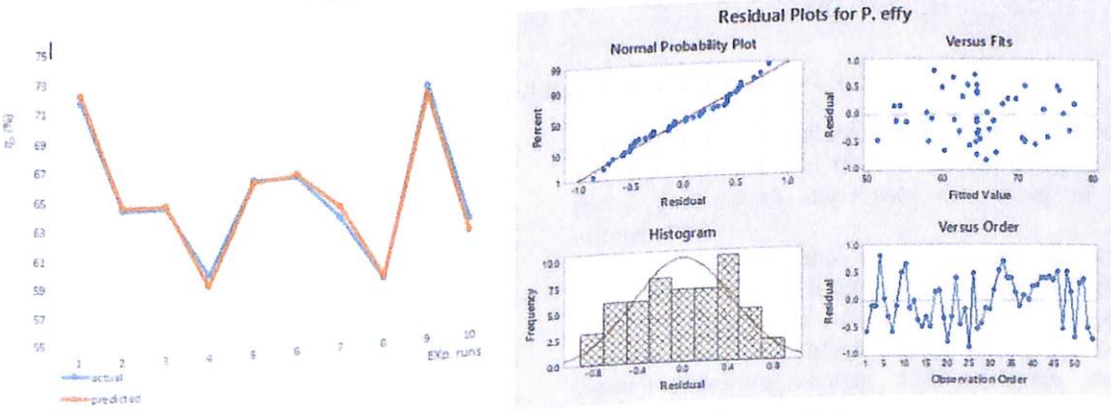

Fig. 13. Confirmatory test and Residual plot for peeling efficiency

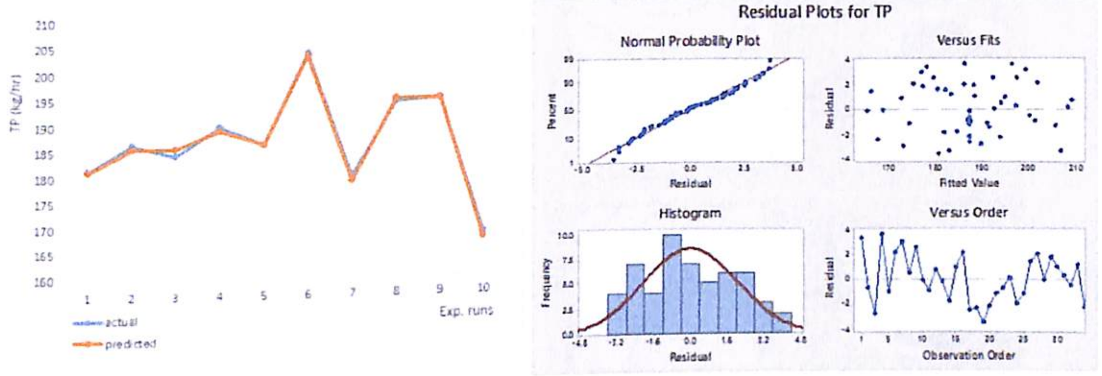

Fig. 14. Confirmatory test and Residual plot for throughput capacity

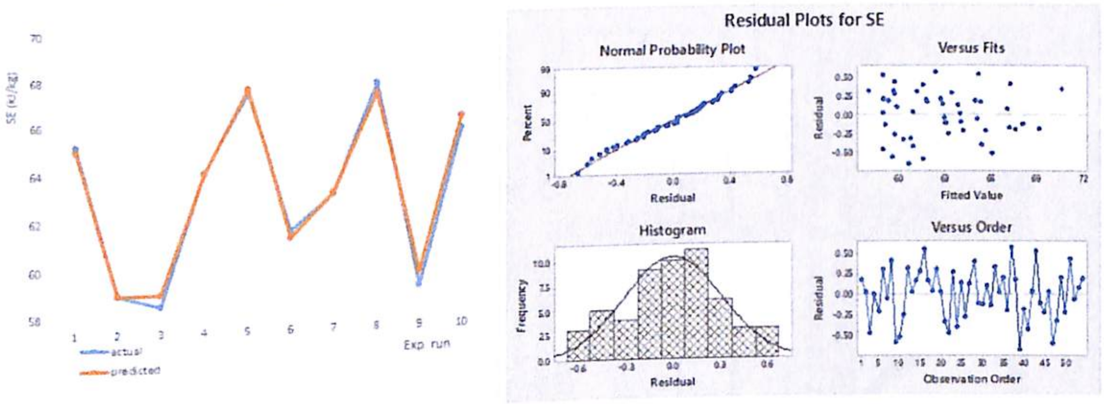

Fig. 15. Confirmatory test and Residual plot for specific energy consumption

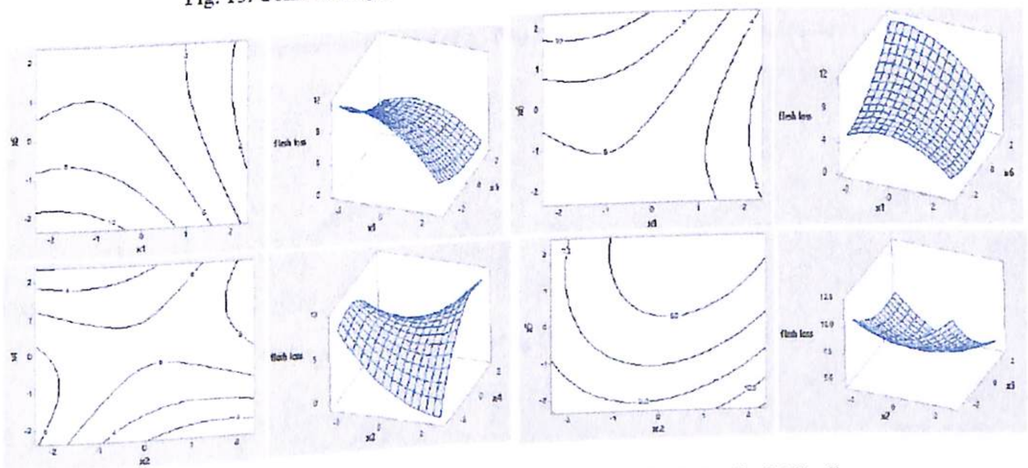

Fig. 16. Response surface plot of F_l (kg) against $x_1.x_5$; $x_1.x_6$; $x_2.x_4$; $x_2.x_5$

Contour plots are useful for establishing the response values and operating conditions that are desirable while the surface plots provides a more vivid concept of the desirable response surface than the contour plots. The desirable response is obtained at the factor pair values or range where the value of flesh loss is minimal. From Figs. 16 and 17 at factor pair of x_2,x_5 and x_5,x_6, a rising and a stationary ridge response pattern is evident, therefore desirable response of minimal flesh loss is obtained at the center point values of the cassava moisture content (x_2) and geometric mean diameter(x_5) and the minimum values of geometric mean diameter and peel thickness (x_6) respectively. Response surface plots for the various pair of predictor variables and the peeling efficiency are shown in Figs. 18 and 19. The desirable response is the factor pair which maximises the value of peeling efficiency.

A stationary response surface ridge pattern depicted with the desirable response to maximise efficiency occurred at maximum values of peeling drum speed and cassava moisture content (x_1,x_2); maximum value of cassava moisture content and minimum value of geometric mean diameter (x_2,x_5); maximum value of number of peeling balls and minimum value of geometric mean diameter (x_4,x_5); maximum values of number of peeling balls and mean peel thickness (x_4,x_6).

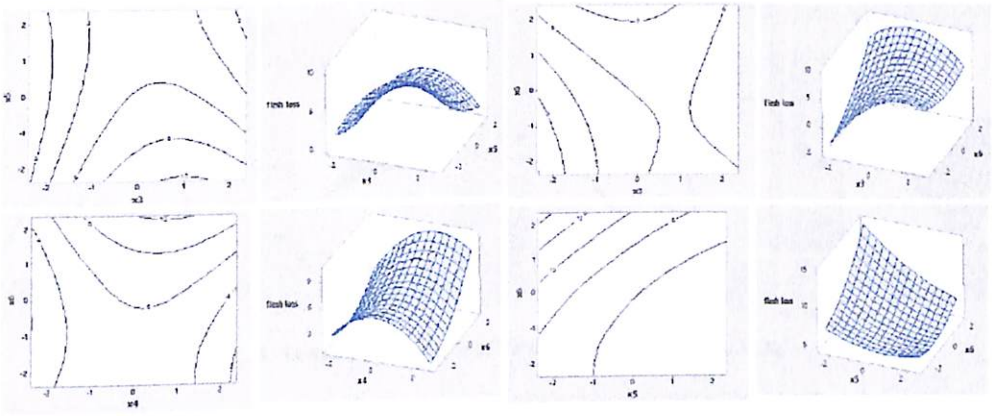

Fig. 17. Response surface plot of F_l (kg) against x_3, x_5; x_3, x_6; x_4,x_6; x_5, x_6

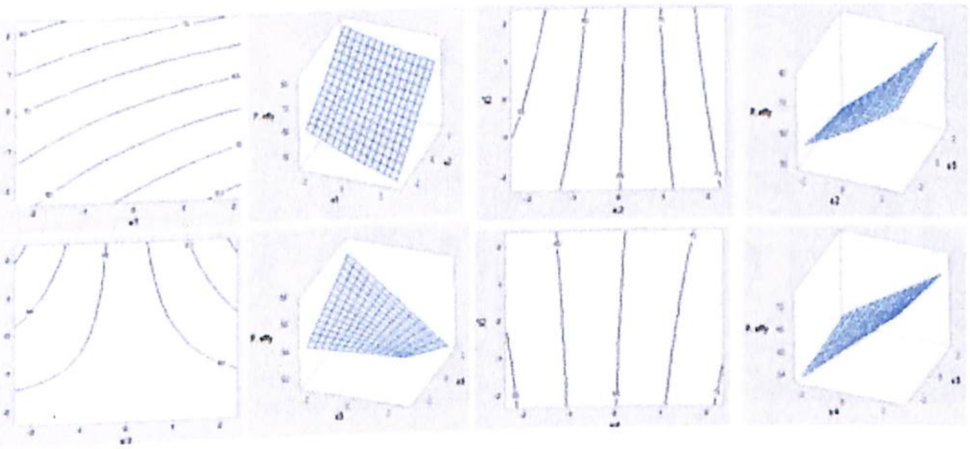

Fig. 18. Response surface plot of η_p (%) against x_1, x_2; x_2, x_5; x_3, x_6; x_4,x_5

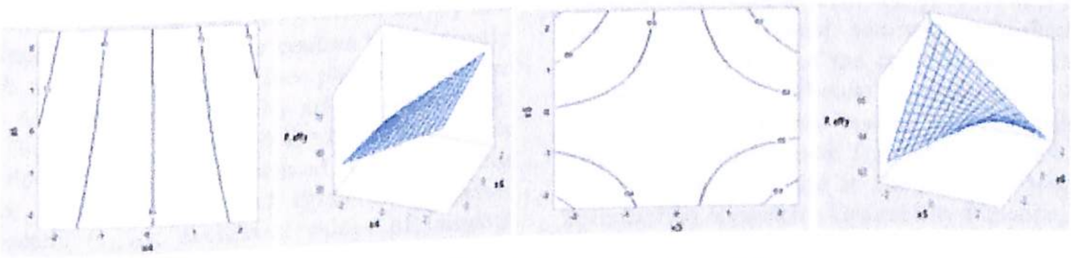

Fig. 19. Response surface plot of η_p (%) against x_4, x_6 and x_5, x_6

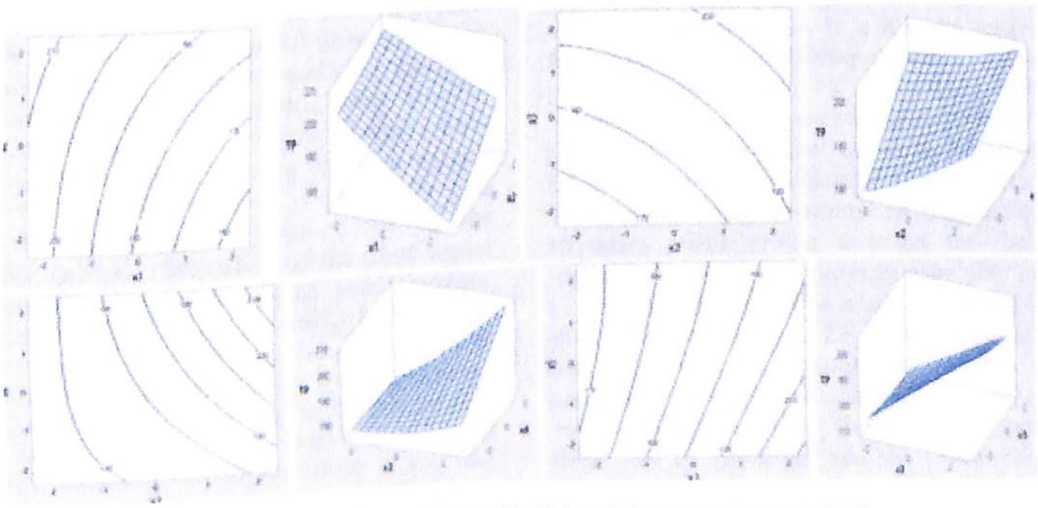

Fig. 20. Response surface plot of TP (kg/hr) against x_1,x_2; x_2, x_3; x_2, x_4; x_3,x_5

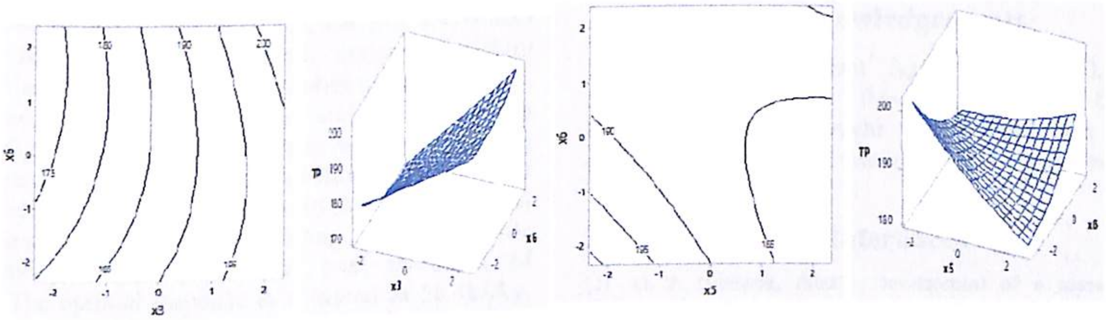

Fig. 21. Response surface plot of $TP\ (kg/hr)$ against $x_3, x_6; x_5,x_6$

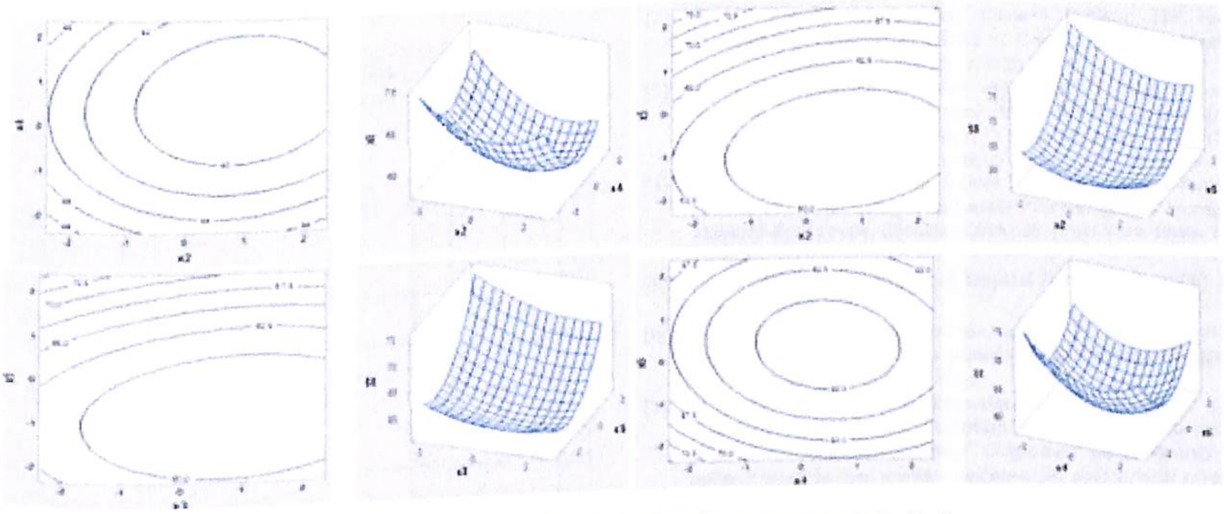

Fig. 22. Response surface plot of $SE\ (kJ/kg)$ against $x_2,x_4; x_2,x_5; x_3,x_5; x_4, x_6$

This result is consistent with the position of [7] that efficiency increases with moisture content but inversely with peel thickness. Response surface plots of predictor factor pairs and throughput capacity are shown in Figs. 20 and 21. The desirable response is the factor pair which maximizes throughput capacity obtained at the following factor pairs: maximum speed of drum and cassava moisture content (x_1,x_2); maximum values of cassava moisture content and mass of cassava (x_2,x_3); maximum values of cassava moisture content and number of peeling balls (x_2,x_4); maximum value of mass of cassava and minimum value of geometric mean diameter (x_3,x_5); maximum value of mass of cassava and peel thickness (x_3,x_6) and minimum values of geometric mean diameter and peel thickness (x_5,x_6). The response surface plots exhibited significant simple maximum response surface patterns and the desirable response is the factor pair which reduces specific energy consumption of the cassava attrition machine. Inspection of the plots depict that the values for the various factor pairs: cassava moisture content versus number of peeling balls (x_2,x_4); cassava moisture content versus geometric mean diameter (x_2,x_5); mass of cassava versus geometric mean diameter (x_3,x_5); number of peeling balls versus peel thickness (x_4,x_6) are within the center points for minimal specific energy consumption. Optimization using the response surface – contour and surface plots – is technically unreliable when there are more than one response and multiple predictors [27]. Thus it can lead to multiplicity of optimal settings established for one response. Inspection of the contour and surface graphs revealed that for a particular response, some factor pairs are in the maximum region while others indicate minimum optimal region. The indeterminate tendency of this approach gave rise to the need for more suitable optimization approach - Desirability Function Approach, which can define the optimal settings of the operational parameters for all the responses. Desirability function approach eliminates the rigors associated with most other optimization techniques. It is a multi -response multi - factor optimization technique which operates on the principle established by Derringer Harrington. It optimizes a set of responses and defines the best factor settings for a solution of a multivariate objective function. The overall objective is to minimize flesh loss and specific energy consumption and maximize peeling efficiency while setting a target for the throughput capacity. The response optimizer capability of MINITAB 17 was employed for this purpose and the optimization plot is given in Fig. 23. The value of individual desirability and the composite desirability respectively approximate to 1 which signifies that the optimization result is highly desirable. The desirability plot in Fig. 23 above can be visualized and the values of the optimal settings graphically presented. Therefore, it is seen that the cassava attrition peeling machine performed optimally at the factor settings of 1.5, 1.0, 2.1, 1.4, -0.023 and 0.7 for peeling drum speed, cassava moisture content, mass of loaded cassava, number of peeling balls, average geometric mean diameter and peel thickness respectively. In natural units the Cassava attrition peeling machine performed optimally at a peeling drum speed of 45rpm, cassava moisture content of 85°Wb, mass of loaded cassava of 81.5kg, 110 peeling balls; geometric mean diameter of 48.56mm and peel thickness of 4.13mm. The optimal response is obtained as 58.4kJ/kg, 180kg/h, 5.49% and 88.7% for the modified machine specific energy consumption, throughput capacity tuber flesh loss and peeling efficiency respectively.

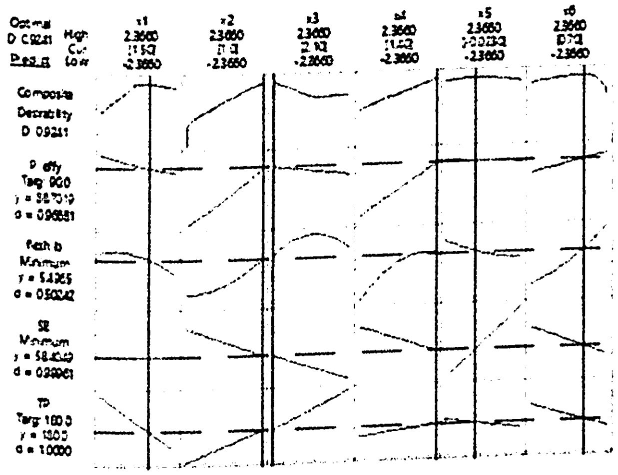

Fig. 23. Optimization plot of the CAPM performance parameters

IV. Conclusion

A modified cassava attrition peeling machine was evaluated and optimized using response surface analysis for efficient peeling with high throughput but at minimal flesh loss and specific energy consumption. Factors investigated were moisture content, M_c geometric mean diameter, D_g peel thickness, P_{th} mass of loaded cassava, peeling drum speed, N_d and number of peeling balls n_b, while efficiency, throughput, flesh loss and specific energy consumption constituted the response variables. Experimental results showed that the developed models described the performance parameter of the machine adequately at 95% prediction interval. The results also confirmed that the machine performs optimally with an efficiency of 88.7%, throughput of 180kg/hr, flesh loss of 5.49% and specific energy consumption of 58.4kJ/kg at an optimal peeling drum speed, cassava moisture content, mass of loaded cassava, number of peeling balls, geometric mean diameter and peel thickness of 45rpm, 85%Wb, 81.5kg, 110, 48mm and 48.56mm respectively in accordance with models analysis (prediction and optimization). ANOVA also revealed that the main effects of all the factors influence the four response variables significantly with the quadratic effect and factor interactions established for model adequacy and desirability.

Acknowledgements

Projects Development Agency (PRODA), Enugu, National Root Crop Research Institute (NRCRI), Umudike and Lewachi Augustine are greatly acknowledged for their material and technical supports.

References

[1] O. J. Olukunle, (2005). Development of a cassava peeling machine. *Proceedings of the International Conference on Global Food and Product Chain Dynamics, Innovations, Conflicts and strategies*, University of Hohenheim Stuttgart, Germany, 'Tropentag 2005'. pp.54.

[2] G. O. Ezekwe, Mechanizing Cassava Peeling: The Project Development Agency (PRODA) of Cassava Nibbling Machine. *PRODA Technical Reports No. 1*, 1-20, 1979.

[3] P. M. Nwokedi, Performance evaluation of cassava peeling machine. In: *Tropical root crops: Production and uses in Africa*, Terry, E.R., Doku, E.U., Arene, O.B. & Mahungu, N.M. (Eds). International Development Research Centre, 108-110, 1984

[4] E. U. Odigboh, Mechanical devices for peeling cassava roots, In: Pluncknett, D. L. (ed.), *Small-scale Processing and Storage of Tropical Root Crops*, (Boulder/Colorado, West View Press, 1979. pp. 66),

[5] IITA (International Institute of Tropical Agriculture) (2006). *IITA Annual report*, 8.

[6] B. O. Akintunde,.F. A. Oyawale, and T. Y. Tunde-Akintunde. Design and fabrication of a cassava peeling machine. *Nigerian Food Journal*, 23, pp. 1 – 8, 2005

[7] O. J. Olukunle, O. C Ademosun, A. S. Ogunlowo, A. S. Agbetoye, A. Adesina, Development of a double action cassava peeling machine. *International Conference on prosperity and poverty in globalised world: challenges for agricultural research* 2006. www.twopentag.com

[8] O. O. Oluwole and M. A. Adio, Design and construction of a batch cassava peeling machine. *Journal of Mechanical Engineering and Automation*, 3 (1). pp.16-21, 2013

[9] G. O. Ezekwe, A feature for achieving a constant depth of peel in the mechanical peeling of cassava. *Nigeria Journal of Engineering*, 1(3),174 – 181, 1976.

[10] E.U, Odigboh, A cassava peeling machine: development, design and construction, *Journal of Agricultural Engineering Research*, 21; 361-369, 1976

[11] NIST/SEMATECH, *Engineering Statistics e-Handbook*, 2006. www.iel.nist.gov/dv898/ handbook (Accessed: 2015).

[12] Nwankwojike B. Nduka, Agunwamba C. Jonah, Odukwe A. Okay, Application of Response Surface Modeling in the Performance Optimization of a Palm Nut-Pulp Separator, (2012) *International Review of Mechanical Engineering (IREME)*, 6 (2), pp. 236-244.

[13] R. H Myer, D.C. Montgomery, *Response Surface Methodology: Process and Product Optimization using Designed Experiment*, (Wiley- Interscience Publication, New York, 2002)

[14] S. Schmidt, and R. A Launsby, *Understanding Industrial Designed Experiments* (3rd Edition, Air Academy Press, 1991).

[15] G. W. Oehlert, *Design and Analysis of Experiment: Response Surface Method and Design*. (Wiley, 2000).

[16] D. C. Montgomery, *Design and Analysis of Experiments: Response Surface Method and Design*, (John Wiley and Sons Inc, New Jersey, 2005)

[17] M. Y. Noordin, V. C. Venkatech, S. Sharif, S. Elting, A. Abdullah, Application of Response Surface Methodology in describing the the performance of coated carbide tools when turningA1511045 Steel. *Journal of Material Processing Technology*: 145, pp. 45-58, 2004

[18] T. E. Capobianco, J. D. Splett, H. K. Iyer, Eddy current Probe sensitivity as a function of coil Construction Parameters, *Research in Nondestructive Evaluation*, Vol.2, pp 169-186, 1990.

[19] A. H. Taieb, S. Msahli, F. Sakli, A New Approach for Optimizing Mechanical Clothing Tactile Comfort, *Journal of advanced Research in Mechanical Engineering*, Vol.1, pp.43-51, 2010.

[20] I. D. Nwachukwu and K.J. Simonyan. Some Engineering Properties of Cassava Tuber related to its peeling Mechanization. *Umudike Journal of Engineering and Technology (UJET)*. Vl/ 1.No.1.pp 12-24, 2015.

[21] D. B. Brooker, F. W. Bakker-Arkema, C. W. Hall. *Drying Cereal Grains. Westport:* (Avi Publishing Co. Inc. pp. 265, 1974).

[22] N. Teter, Paddy Drying Manual. *Agricultural Services* Bulletin No. 70, FAO, Rome. Pp. 123, 1987

[23] A. Parra-Coronado, G. Fischer, J. H. Camacho-Tamayo. Development and quality of pineapple guava fruit in two locations with different altitudes in Cundinamarca, Colombia. *Bragantia* (2015)

[24] M. A. Del Nobile, S. Chillo, P. M. Falcone, J. Laverse., S. Pati . A. Baiano, Textural Changes of Canestrello Pugliese Measured During Storage *J. F. ENG*, 83:621-628.(2007)..

[25] I. D. Nwachukwu, and K. J. Simonyan. Some Engineering Properties of Cassava Tuber related to its peeling Mechanization. *Umudike Journal of Engineering and Technology* (JET), Vl/ 1.No.1.pp 12-24, 2015.

[26] C. C. Egbeocha, S. N. Asoegwu, and N. A .A. Okereke.. A Review on Performance of Cassava Peeling Machines in Nigeria . *Futo Journal Series (FUTOJNLS)* Volume-2, Issue-1, pp- 140 – 168, 2016.

[27] S. O. Isaac, B. N. Nwankwojike, O. Ogbonnia, (). Performance Optimization of a Multistage Centrifugal Pump for Heavy End Recovery Using Desirability Function Approach. *International Journal of Oil, Gas and Coal Engineering,* 3(6): 66-76, 2015. http://www.sciencepublishinggroup.com/j/ogc

[28] Ihaddadene, N., Erani, P., Cristofolini, L., Baleani, M., Viceconti, M., Fatigue-Fractured Surfaces of Acrylic Bone Cements, (2015) *International Review of Civil Engineering (IRECE)*, 6 (1), pp. 25-30.
doi:https://doi.org/10.15866/irece.v6i1.6556

[29] Muslim, A., Ardy, S., Syaubari, S., Response Surface Methodology-Based Model and Optimization of CO2 Absorption Using Methyldiethanolamine Activated by Piperazine, (2017) *International Review on Modelling and Simulations (IREMOS)*, 10 (4), pp. 296-302.
doi:https://doi.org/10.15866/iremos.v10i4.10703

Authors' information

John C. Edeh is an academic researcher in the Department of Mechanical Engineering at Michael Okpara University of Agriculture, Umudike, Nigeria. He holds B. Eng. M. Eng. Ph. D degrees (Nigeria) in design and production engineering. He is an author of over twenty journals articles and his research interests are machine design and development, material, modeling and optimization. Dr. Edeh is a registered Engineer in Nigeria and a member of many professional bodies.

Bethrand N. Nwankwojike is an Associate Professor of Mechanical Engineering Department at Michael Okpara University of Agriculture, Umudike, Nigeria. He holds B. Eng. M. Eng. Ph. D degrees in mechanical and industrial engineering/management and authored over fifty journals articles and three patents. His research interests are systems design, development, modeling and optimization. Engr. Dr. Nwankwojike is a registered Engineer in Nigeria and a member of many professional bodies.

Fidelis I. Abam is an Associate Professor of of Mechanical Engineering Department at Michael Okpara University of Agriculture, Umudike, Nigeria. He holds a PhD degree in energy and power technology from the University of Nigeria and a Master's degree in thermo-fluid engineering from University of Lagos, Nigeria. His research interests are: exergy and environment, renewable energy system, power plant engineering and machine design.

International Review of Mechanical Engineering (I.RE.M.E.), Vol. 12, N. 10
ISSN 1970 - 8734
October 2018

Aerodynamics Analisys of the Wingtip Fence Effect on UAV Wing

Setyo Hariyadi S. P.[1, 2], Sutardi[2], Wawan Aries Widodo[2], Muhammad Anis Mustaghfirin[3]

Abstract – *Winglets have an important effect in the use of aircraft and of unmanned aerial vehicle (UAV). The expected effect in winglet usage is the increase of the lift coefficient and the decrease of the drag coefficient. These aspects play a very important role in determining aerodynamic performance. Many researches have been done in order to determine the most effective winglet designs to further explore the effects on aircraft and unmanned aerial vehicle (UAV). Based on that fact, in this study the use of winglet on UAV is discussed. This research has been conducted using a simulation software with turbulent model k-ω SST. The freestream velocity used is 10 m / s (Re=2.3 × 10⁴) with an angle of attack (α) = 0°, 2°, 4°, 6°, 8°, 10°, 12°, 15°, 16°, 17° and 19°. Model specimens are airfoils Eppler 562 with and without winglet. Winglet used in this study are wingtip fences with forward and rearward configuration. From the research, it has been found that the addition of winglet can minimize vorticity magnitude behind the wing especially forward wingtip fence. Forward wingtip fence results in a smaller vorticity area than plain wing and rearward wingtip fence although the vorticities increase with the increase of the angles of attack. In addition, the forward wingtip fence can prevent the formation of tip vortex better than the rearward one.* ***Copyright © 2018 Praise Worthy Prize S.r.l. - All rights reserved.***

Keywords: *Airfoil, Winglet, Wingtip Fence, Eppler 562, Lift Coefficient, Drag Coefficient*

Nomenclature

α	Angle of attack
C	Chordline
y	Wall normal coordinate
y^+	Normalized y by inner variables, $y^+ \equiv yU_\tau/\nu$
C_{DT}	Drag total coefficient, include drag pressure dan viscous drag
C_L	Lift coefficient
C_f	Skin friction coefficient, $C_f \equiv 2\tau_w/(\rho(U_0)^2)$
U	Mean velocity in the streamwise direction
U_τ	Friction velocity $U_\tau \equiv (\tau_w/\rho)^{0,5}$
V_∞	Free stream velocity
$-\overline{u'u'}$	Turbulent Reynolds Stress
K	Turbulent kinetic energy
F_1	Blending function
S	Modulus of the mean rate-of-strain tensor
F_2	The blending function for the turbulent eddy viscosity in the SST model
ω	Specific dissipation rate

I. Introduction

There are several things that allow to minimize drag and to increase the lift on the use of aircraft and unmanned aerial vehicle (UAV), including a good wing design, wingtip devices / winglet, boundary layer suction and others [1]-[29].

Winglets have an advantage in terms of reducing the occurrence of vortex tip and they can reduce the area that is not effective because of the movement of the flow from the lower to the upper side of the wing. This is the concern of many researchers to continuously explore so as to provide space for research on the application of winglet that can produce significant drag reduction.

Kontogianis, et al. [1] have studied the optimization of UAV aerodynamic design on the wing; horizontal stabilizer, vertical stabilizer and aileron are name of the part aircraft or unmanned aerial vehicle. Wing airfoil use Eppler 420 with Re = 1.3×10⁵ – 2.4×10⁵. Plain wing with wingtip fence has resulted in a better performance than plain wing with blended winglet, hoerner, and elliptical winglet. The effect is clearly presented and it provides a comparison of the flow field of the baseline and the final wingtip region. It is obvious that the wingtip vortex strength is greatly reduced by the use of the specially designed winglet. Design modifications result has improved the performance of 7.7%. Gavrilovic, et al. [2] have compared the effects of using various types of winglets, namely blended winglet, wingtip fence, maxi winglet and spiroid winglet on NACA 64412 airfoil wing. With an increase in lift, the increase in wingtip vortices strength will increase as well as induced drag on the plane. Using winglet vortices intensity and induced drag can be reduced. This performance is very important when landing and taking off because it reduces runway distance as needed. With this winglet the speed of climbing will also increase.

Hariyadi, et al [3] have performed a simulation using the airfoil type NACA 43018 by adding a winglet in the form of forward wingtip fence and rearward wingtip fence. In the study it has been found that the addition of a

https://doi.org/10.15866/ireme.v12i10.15517

winglet has been able to increase C_L/C_D value up to 22.9% for forward wingtip fence type at α=2°.

Kontogianis et al [4] have performed a numerical study on the airfoil E420 ATLAS IV UAV wing with Re = 10^5 – 3×10^5. The consideration of selecting an Eppler in type airfoil is that it has a low *Re* airfoil, and high lift characteristic. In this study it has been found that the addition of a winglet can reduce drag coefficient by 2.8% and it can increase C_L/C_D by 80% at low attack angle and 22% in operational region. Hariyadi, et al. [5] have used Eppler 562 wing airfoil in order to compare rearward wingtip fence with cant angle 90° and 75°. Lift produced by the wing with the wingtip fence is better than the plain wing starting at an α=8°. Lift to drag ratio of rearward wingtip with 90° has better performance than plain wing and rearward wingtip fence with cant angle 75°. However, rearward wingtip fence with 75° has a smaller vorticity magnitude area than plain wing and rearward wingtip fence cant angle 90°. Hariyadi, et al. [6] have compared the plain wing Eppler 562 with the forward wingtip fence cant angle 90° and 75°. Forward wingtip fence with cant angle 90° provides better aerodynamic performance than forward wingtip fence cant angle 75 and plain wing. The better performance starts from the α=6°. The vorticity magnitude produced by forward wingtip fence with cant angle 90° is also better than the forward wingtip fence cant angle 75 and plain wing. This is characterized by a narrower vorticity magnitude than others. Gölcük, et al. [7] have combined several parameters on the UAV wing, including cant angle, sweep angle, taper ratio, toe angle and twist angle.

Cant angle has a significant effect on lift coefficient, drag coefficient and lift force, while taper ratio has a big effect on lift to drag ratio. The obtained improvement in aerodynamic performance has reached 8.32% from plain wing. The use of winglets reduces vorticity magnitude on both the yz and xy axes. In this research, an airfoil Eppler 562 has been used with an endwall attached to the wall and a wingtip fence added at tip with forward and rearward variation. Numerical simulations have been made to study details on how big the influence of wingtip fence addition is to reduce induced drag with various angles of attack.

II. Methodology

II.1. Mathematical Model

The Reynolds-averaged Navier-Stokes (RANS) equation [30]-[31] for a steady state incompressible flow is given by:

$$\nabla \cdot \bar{u} = 0 \tag{1}$$

With the turbulent Reynolds Stress term, $-\overline{u'u'}$, the equation becomes:

$$\nabla \cdot \overline{uu} = -\nabla\left(\frac{p}{\rho}\right) + \upsilon\nabla^2 + \nabla \cdot (-\overline{u'u'}) \tag{2}$$

Menter, et al [8] have defined Shear- Stress Transport (SST) κ–ω model, where κ is the turbulent kinetic energy and υ_t is the turbulence viscosity. The turbulent Reynolds stress is modeled as:

$$-\overline{u'u'} = \upsilon_t(\nabla\bar{u} + \nabla\bar{u})^T - \frac{2}{3}K\delta \tag{3}$$

Therefore the turbulent kinetic energy κ and the specific dissipation rate ω of the SST model are given:

$$\frac{\partial K}{\partial t} + \bar{u}_i\frac{\partial K}{\partial x_i} = \widetilde{P_K} - \beta^* K\omega + \frac{\partial}{\partial x_j}\left[(\upsilon + \sigma_K\upsilon_t)\frac{\partial K}{\partial x_j}\right] \tag{4}$$

$$\begin{aligned}\frac{\partial K}{\partial t} + \bar{u}_i\frac{\partial \omega}{\partial x_i} = \alpha S^2 - \beta\omega^2 + \frac{\partial}{\partial x_j}\left[(\upsilon + \sigma_K\upsilon_t)\frac{\partial K}{\partial x_i}\right] \\ + (1 - F_1)2\alpha_d\frac{1}{\omega}\frac{\partial K}{\partial x_j}\frac{\partial \omega}{\partial x_j}\end{aligned} \tag{5}$$

The last term on the right side of equation (5) is known as cross diffusion term [9]. Menter [10] has demonstrated that introducing cross diffusion term in the ω equation, the free stream dependency of the κ–ω model is reduced. The blending function F_1 is defined as:

$$F_1 = \tanh(arg_1^4) \tag{6}$$

$$arg_1^4 = \min\left[\max\left(\frac{\sqrt{k}}{\beta^*\omega y}; \frac{500\upsilon}{y^2\omega}\right); \frac{4\rho\sigma_{\omega 2}k}{CD_{k\omega}y^2}\right] \tag{7}$$

where y is the distance to the nearest surface:

$$CD_{k\omega} = \max\left(2\rho\sigma_d\frac{1}{\omega}\frac{\partial K}{\partial x_j}\frac{\partial \omega}{\partial x_j}; 10^{-10}\right) \tag{8}$$

$CD_{k\omega}$ is the positive portion of the cross diffusion term. The turbulent eddy viscosity is formulated as follows:

$$\upsilon_t = \frac{\alpha_1 k}{\max(\alpha_1\omega; SF_2)} \tag{9}$$

$$S = \sqrt{2\overline{S_{ij}}\,\overline{S_{ij}}} \tag{10}$$

where S is the modulus of the mean rate-of-strain tensor S_{ij}:

$$S_{ij} = \frac{1}{2}\left(\frac{\partial u_i}{\partial x_j} + \frac{\partial u_j}{\partial x_i}\right)$$

$$F_2 = \tanh(arg_2^2) \tag{11}$$

F_2 is the blending function for the turbulent eddy viscosity in the SST model:

$$arg_2^2 = \max\left(\frac{\sqrt{k}}{\beta^*\omega y}; \frac{500\upsilon}{y^2\omega}\right) \tag{12}$$

In the SST model the production of turbulence kinetic energy is limited in order to prevent the build-up of turbulence in stagnation regions defined as:

$$\widetilde{P_K} = (\upsilon_t S^2; 10\beta^* K\omega) \tag{13}$$

Assuming that ϕ represents the set of closure constants for the SST model and ϕ_1 and ϕ_2 represent the constants from the standard κ–ω and κ–ε models respectively [8]:

$$\phi = F_1\phi_1 + (1 - F_1)\phi_2 \tag{14}$$

The constants ϕ are calculated using a blend between the constants ϕ_1 (κ–ω) and ϕ_2 (κ–ε).

The constants applied in the ϕ_1 (κ–ω) are equal to:

$$\begin{gathered}\beta = 0.075, \beta^* = 0.09, \sigma K = 0.5, \sigma\omega = 0.5,\\ \sigma d = 0.856, \alpha = 5/9\end{gathered} \tag{15}$$

The constants applied in the ϕ_2 (standard κ–ε) are equal to:

$$\begin{gathered}\beta = 0{,}0828, \beta^* = 0.09, \sigma K = 1, \sigma\omega = 0.856, \sigma d\\ = 0.856, \alpha = 0.44\end{gathered} \tag{16}$$

II.2. Computational Fluid Dynamics

This research has been conducted using numerical simulation of Ansys 17 with turbulent model *k-ω SST*.

The k-ω SST model which is developed by Menter [11] is a turbulent model that combines k-ω standard, which is stable and accurate to be used in the area near the wall and k-ε model which has the advantage to be used in free stream. Turbulent model *k-ω SST* for 3D RANS equations with transient time dependent has also been used by Sunil [12], Rostane [13] and Saad [14]. The used freestream velocity is 10 m/s (Re=2.3 × 10^4) with angles of attack (α)=0°, 2°, 4°, 6°, 8°, 10°,12°, 15°, 16°, 17° and 19°.

Model specimens are airfoil E562 with and without winglet (plain wing). Winglet to be used is wingtip fence with addition of forward and rearward design. Reynolds number flow is based on chord and free stream velocity with chord length of 20 cm. Figs. 1 depict the dimension of the model and Fig. 2 shows a simulation domain and the boundary conditions used in the simulation. The winglet modeling dimensions mounted on the tip of the wing are shown in Fig. 3 [15].

In the numerical simulation, geometry, meshing and boundary types for specimens are constructed. After making geometry, the next step is to do the meshing process and to determine the boundary type. The geometry meshing process is done on plain wing. The geometry and the meshing shapes are shown in Fig. 5. In Figs. 4 it is shown that around the wing surface a quadriateral element is used. Whereas, in areas far from the wing surface triangular elements are used. The selection of this element considers the rate of convergence (or even lack of convergence), the solution accuracy and the CPU time required.

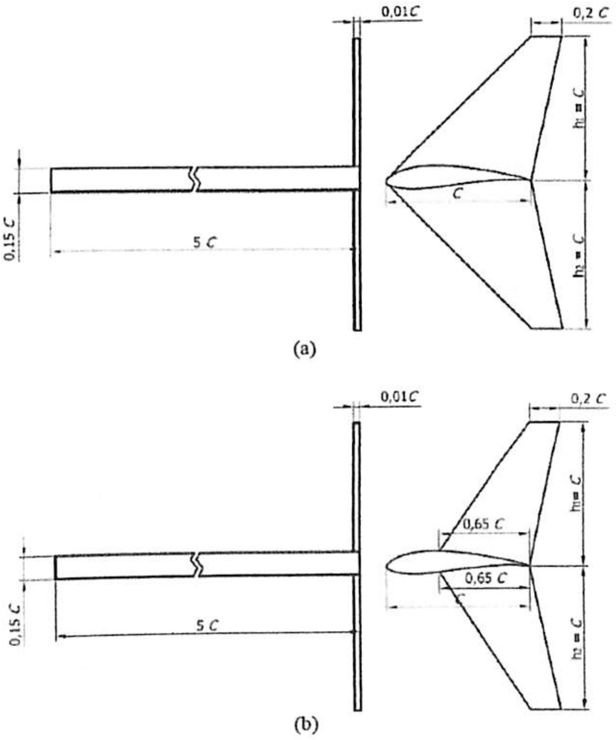

Figs. 1. Dimension of the model (a) Forward Wingtip Fence (b) Rearward Wingtip Fence

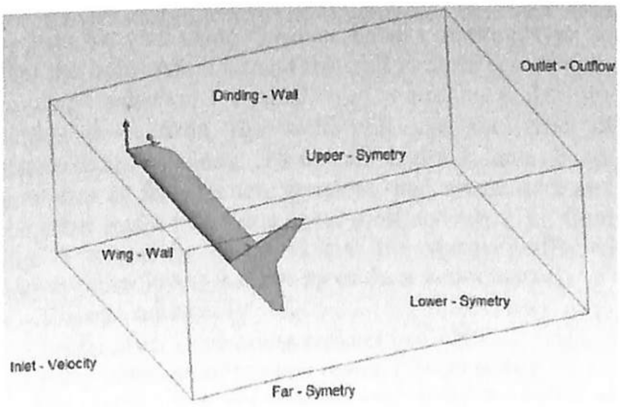

Fig. 2. Domain simulation and boundary conditions

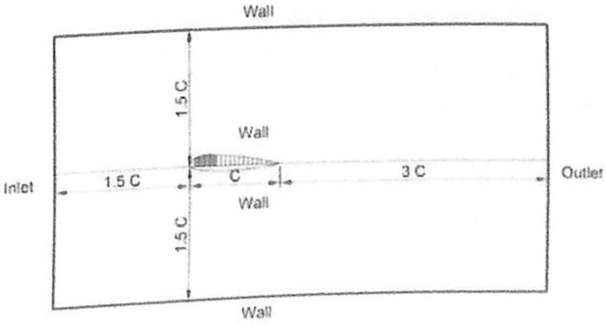

Fig. 3. Modeling dimensions [15]

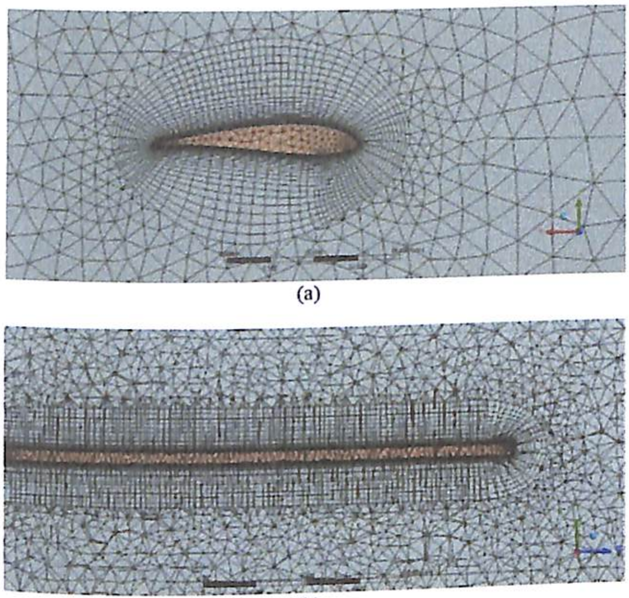

(a)

(b)

Figs. 4. Geometry and meshing: (a) Side View (b) Section View

This model uses air as a working fluid with $(\rho) = 1.17\ \mathrm{kg/m^3}$, viscosity $(\mu) = 1.86 \times 10^{-5}\ \mathrm{Ns/m^2}$.

The type and properties of the material are used according to the conditions of the environment, i.e. at 30°C and 1 atm pressure. The intensity of turbulence in this numerical modeling is set to 0.8% at the inlet and the length scale at the inlet side is 0.024 m. The *k-ω SST* turbulence model is used in this study. The solution uses second order for pressure, turbulent kinetic energy, momentum, and turbulent dissipation rate. The convergence criterion is set at 10^{-5}, and the transient mode is used for solver.

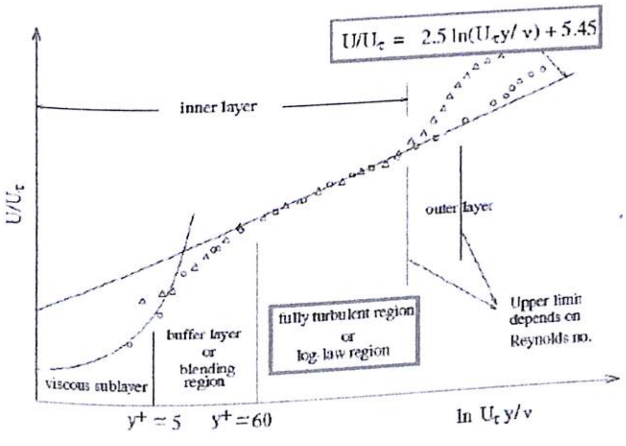

Fig. 5. Subdivisions of near-wall region[21]

II.3. *Grid Independence and y+Calculation*

Simulation study requires the accuracy of data both in preprocessing and post processing. A grid independence is needed in order to determine the level and the structure of the best and the most efficient grid in order to approximate actual modeling results. Grid Independence is a method to determine that the results are not influenced by the number of grids. It should be understood that the use of the number of elements in numerical modeling affects very significantly the results.

The optimum number of grids results in good accuracy with the minimum number of elements as possible. In addition, most of the optimal grid size result if the difference C_D between two candidate grid size is approximatelly 2% [16]. In this grid independence test, the division of the number of meshing into 6 types, then from this type of meshing the smallest value of each meshing will be searched by comparing the Numeric C_D graph. The C_D value of the independent grid is shown in Table I. Table I shows the meshing variation of the grid independence of the 3-dimensional test model on the Reynolds number of 2.34×10^4.

TABLE I
GRID INDEPENDENCE ANALYSIS OF 3 DIMENSIONAL MODEL PLAIN WING E362

Meshing Type	*Cells Number*	*Inflation Layer*	C_D	y^+	*Skewness Average*
Meshing A	367075	40	0,86	2,1	0,346
Meshing B	469620	40	0,88	1,4	0.347
Meshing C	569233	40	0,90	0,8	0,343
Meshing D	685063	40	0,92	2,1	0,334
Meshing E	768003	40	0.90	0.8	0,351
Meshing F	875962	40	0.91	1.4	0,348

In order to obtain more accurate results in the near wall region, it is essential to calculate y^+ for each meshing. The y^+ calculation is based on the calculation of flat plate boundary layer theory [17]. In addition to the calculation of y^+, inflation layer is required for the area around the wall using the quadrilateral meshing type so that the information around the wall is more accurate. In order to calculate the number of minimum nodes, the farther area from the wall will use the type of tetrahedrons meshing. Near-wall regions have larger gradients in the solution variables, and momentum and the other scalar transports occur most actively [18]; from Fig. 5 it can be observed that the viscosity-affected region (inner layer) is made up of three zones, namely:

- Viscous sublayer ($y^+<5$)
- Buffer layer or blending region ($5<y^+<30$)
- Fully turbulent or log-law region ($y^+<30$ to 60)

The wall y^+ is a non-dimensional distance similar to local Reynolds number, often used in numerical method to describe quality of mesh for a particular flow. Values of y^+ close to the lower bound ($y^+ \approx 30$) are most hoped for wall functions whereas $y^+ \approx 1$ are most hoped for near-wall modeling [19]. In this study, in order to obtain the best result y^+ is less than 1 as done in Kontogiannis research [4]. From four grid types as shown in Table I, it can be concluded that the grid type (meshing type) C is the best choice in this simulation since the obtained value of y^+ is minimum. Table I also shows the result of simulation study of Eppler 562 to obtain C_D. Based on Table I, it can be seen that the meshing C is the option number of grid size. Besides C_D and y^+, it is necessary to see the effect of different mesh on the coefficient of friction [11]. Fig. 7 shows that each mesh gives a different influence on the coefficient of friction.

In Fig. 6, it looks Mesh A with the smallest number of nodes giving the friction coefficient with the most difference value compared to the other mesh. At Ansys, mesh quality with high skewness values are not recommended. Generally, it is tried to keep the maximum skewness of mesh volume <0.95 [20].

From Table I, it can be seen that the mesh quality of the model is acceptable.

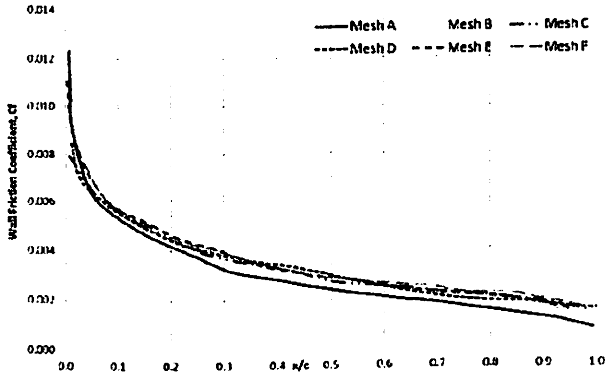

Fig. 6. Mesh effect on wall friction coefficient

In order to ensure that the iteration results get the desired convergence, the mesh used is compared to the C_L and C_{DT} results with the Turanoguz [22] research at freestream velocity 45 m/s. The comparison results appear in Fig. 7 and Fig. 8.

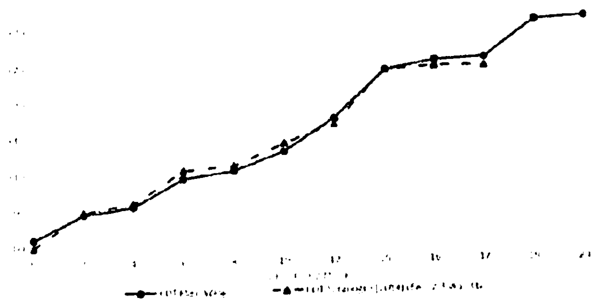

Fig. 7. Comparison of C_{DT} research with Turanoguz [22] research at freestream velocity 45 m/s (Re=2,358 × 10^6)

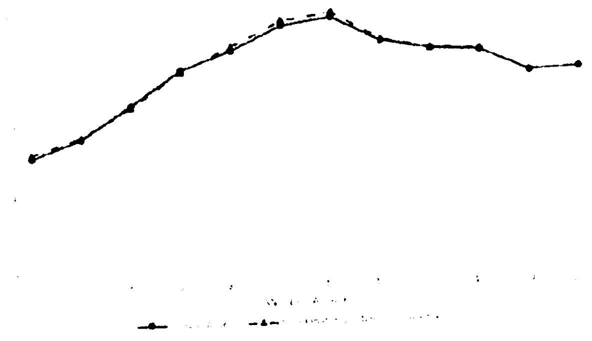

Fig. 8. Comparison of C_L research with Turanoguz [22] research at freestream velocity 45 m/s (Re = 2,358 × 10^6)

III. Results and Discussions

III.1. Vorticity Magnitude

The visualization of the vorticity magnitude contour on the yz plane (Figs. 9) shows the distribution of vorticites around the wing. The vorticity field comparison between the results in plain wing, plain wing with forward wingtip fence and plain wing with rearward wingtip fence shows that there is a significant difference in vorticity magnitude distribution. The vortex area width and vorticity magnitude size are major indications of a fluid leap from the lower surface to the upper surface of the wing. Figs. 9 show the comparation of vorticity magnitude area of plain wing, forward wingtip fence cant angle 90°, and rearward wingtip fence cant angle 90° taken at 1C distance behind trailing edge (x=2C) and at the angles of attack α=0 °, α=12°, α=17°, and α=19°. At α=0°, the effect of the winglet is less visible, so the phenomenon of vortex tip is not so formed and the results of the visualization cannot be so distinguishable. In α=12°, α=17°, and α=19°, the phenomenon of the tip vortices is more visible, so the difference in tip vortex formation on airfoil without winglet and airfoil with winglet fence can be distinguished. At α=0° to α=12°, plain wing produces a larger vortex tip compared to airfoil with wingtip fence. Plain wing has higher vorticity intensity than the other ones. This higher intensity can be seen through the magnitude of the contours formed on the plain wing in the tip section. At the tip of the wing, the maximum vorticity value that occurs is between $10s^{-1}$-$30s^{-1}$. Maximum vorticity in the tip on the wing with forward wingtip fence cant angle 90°, and rearward wingtip fence cant angle 90° has value $10s^{-1}$-$30s^{-1}$ but has a smaller area and most have vortices $(0\text{-}10)s^{-1}$. This shows that at α=0° to α=12° the use of forward and rearward wingtip fence cant angle 90° can reduce the effect of tip vortex that interferes with fluid flow. At α=17° in Fig. 9(g), wing Eppler 562 with forward wingtip fence cant angle 90° has vorticity of tip vortex smaller than wing Eppler 562 without winglet.

It can be seen that wing Eppler 562 with forward wingtip fence cant angle 90° at α=17° has vorticities with magnitudes up to 10 s^{-1}, while wing Eppler 562 without winglet produces higher vorticity magnitude at the wing tip area about $(10\text{-}30)s^{-1}$. Plain wing produces a wider vorticity area than wing with wingtip fence. It can be seen that the wake in wing with rearward wingtip fence is larger when compared with the wake in airfoil without winglet. This is due to the leakage of flow at the corner leading edge in the front of the rearward wingtip fence.

At α=19° in Fig. 9(h), wing with forward wingtip fence has a smaller vorticity magnitude of tip vortex than vorticity magnitude wing without winglet. It can be seen that wing Eppler 562 with forward wingtip fence cant angle 90° at angle α=19° has dominant contour with value around $(0\text{-}10)s^{-1}$, while wing Eppler 562 without winglet has a higher vorticity of about (10-30) s^{-1}. Plain wing has a wider range than wing with wingtip fence.

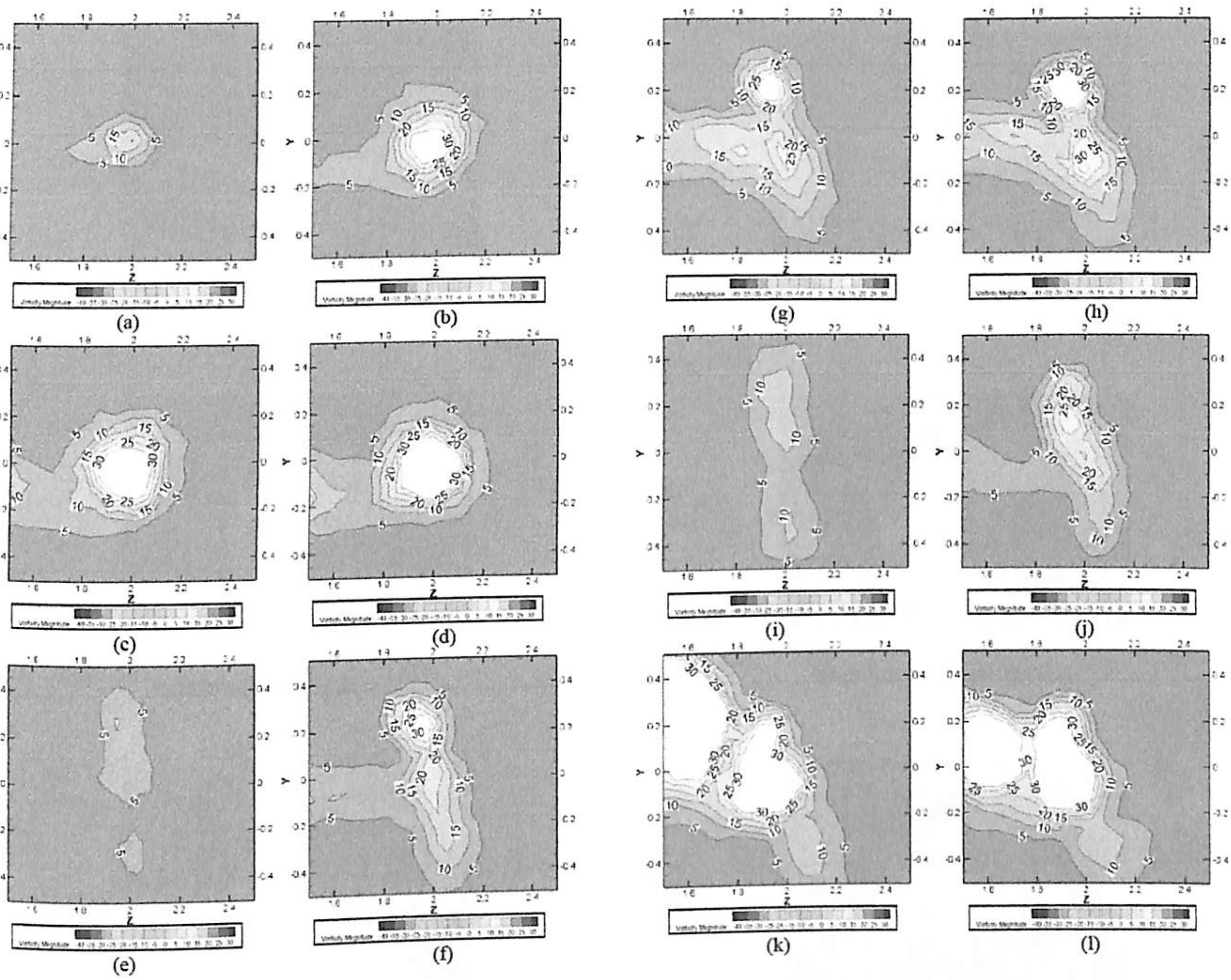

(a) (b) (g) (h) (c) (d) (i) (j) (e) (f) (k) (l)

Figs. 9. Vorticity Magnitude (s^{-1}) on the yz plane (a) Plain Wing $\alpha=0^\circ$ (b) Plain Wing $\alpha=12^\circ$ (c) Plain Wing $\alpha=17^\circ$ (d) Plain Wing $\alpha=19^\circ$ (e) Forward Wingtip Fence $\alpha=0^\circ$ (f) Forward Wingtip Fence $\alpha=12^\circ$ (g) Forward Wingtip Fence $\alpha=17^\circ$ (h) Forward Wingtip Fence $\alpha=19^\circ$ (i) Rearward Wingtip Fence $\alpha=0^\circ$ (j) Rearward Wingtip Fence $\alpha=12^\circ$ (k) Rearward Wingtip Fence $\alpha=17^\circ$ (l) Rearward Wingtip Fence $\alpha=19^\circ$

For wing with rearward wingtip fence, it can be seen that wake large enough when compared with wing without winglet. This is due to the leakage of flow at the leading edge right at the front of the rearward wingtip fence. In addition, this indicates that the higher the angle of attack is, the larger tip vortex will be formed. From the above analysis, it can be seen that vorticity magnitude for wing without winglet is concentrated at one location; on the contrary, vorticity magnitude for the wing with forward wingtip fence and rearward wingtip fence vorticities are splitted into two regions.

The use of forward wingtip fence is more effective than the rearward one because the coverage of large magnitude of vorticity area is smaller. Rearward wingtip fence is effective up to $\alpha=12^\circ$ if the magnitude coverage area of vorticity in tip vortex is considered. In Figs. 10, the comparison of vorticity magnitude on the xy axis is shown.

Vorticity magnitude development increases with the increase of the angle of attack. This is indicated by the increase in vorticity magnitude at $\alpha=12^\circ$ and $\alpha=17^\circ$ in the plain wing, forward wingtip fence and rearward wingtip fence.

Plain wing produces the greatest vorticity magnitude compared to the forward wingtip fence and rearward wingtip fence. With the use of the wingtip fence it is shown that the strength of the vorticity magnitude decreases faster than the plain wing.

III.2. Velocity Pathline Structure

Fig. 11(a) is a visualization of a velocity pathline on an airfoil with $\alpha=17^\circ$ and $\alpha=19^\circ$, for plain airfoil. The visualization of the pathline shows that the flow on the midspan is distributed evenly across the span and tends to follow the contour of the body up to its trailing edge.

The pathline at the wingtip shows the fluid leaps from the lower surface to the upper surface and then combines with the flow from the leading edge. The combination of the two streams causes a rotating motion from the leading to the trailing edge. As the angle of attack increases, the width of the rotating motion is wider as shown in Fig. 11(b). The rotating motion has downward velocity component or to the wing section which is often referred to as downwash velocity.

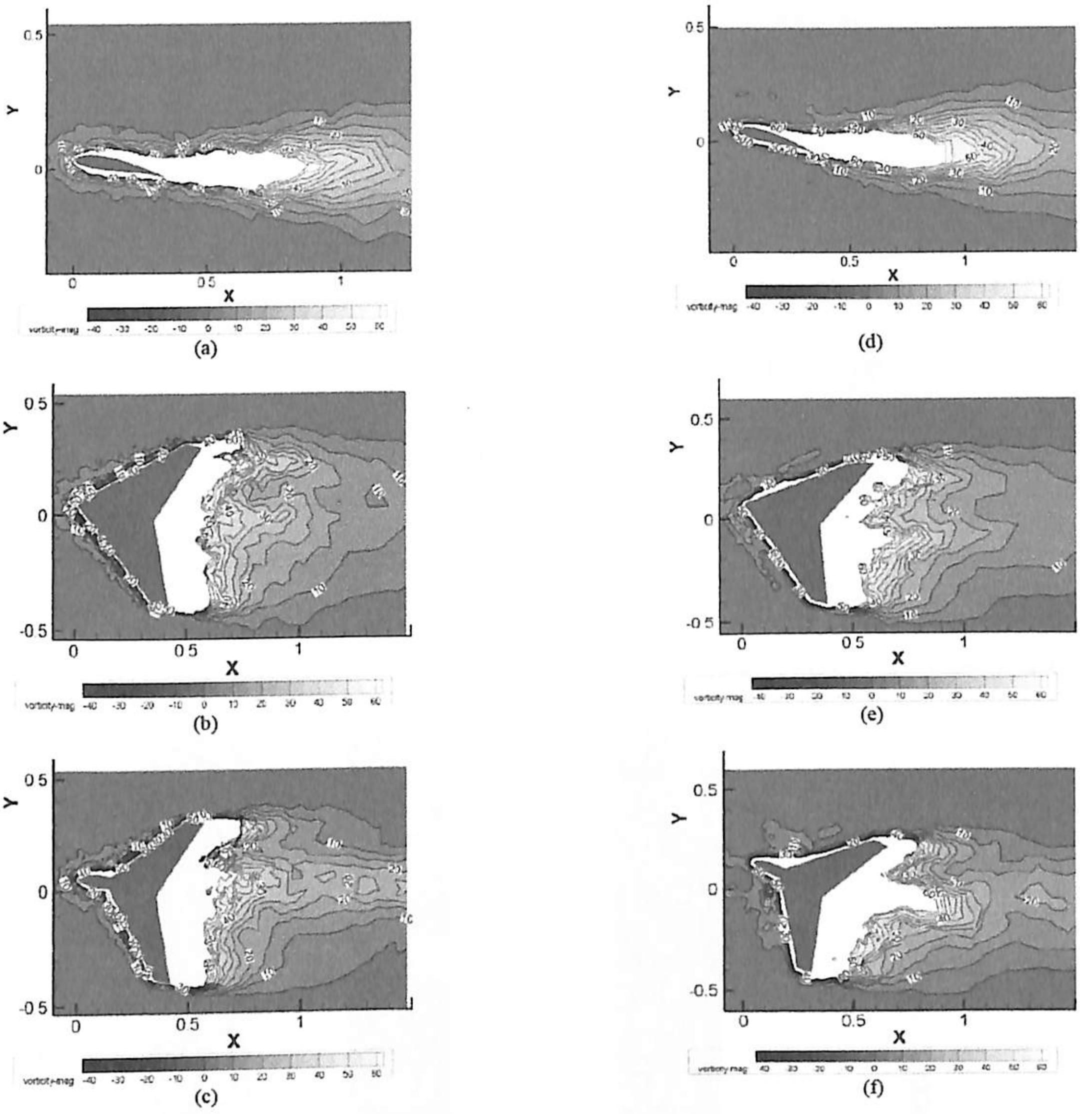

(a) (b) (c) (d) (e) (f)

Figs. 10. Vorticity Magnitude (s^{-1}) on the xy plane. (a) Plain Wing $\alpha=12°$ (b) Forward Wingtip Fence $\alpha=12°$ (c) Rearward Wingtip Fence $\alpha=12°$ (d) Plain Wing $\alpha=17°$ (e) Forward Wingtip Fence $\alpha=17°$ (f) Rearward Wingtip Fence $\alpha=17°$

Fig. 11(c) shows the wing with the addition of forward wingtip fence at $\alpha=17°$. At the midspan, fluid flow follows the surface of the wing body.

For wing with forward wingtip fence, the airflow leaps from the lower surface can be avoided so the flow at the wingtip is not disturbed and it can follow the wing surface up to the trailing edge. Behind the midspan, it can be seen the initial formation of trailing edge vortices indicated by the pathline deflection to the spanwise direction.

As the angle of attack increases to $\alpha=19°$ (Fig. 11(d)), the fluid flow in the midspan can follow the surface of the wing. Likewise, the fluid flow near the wingtip can follow the wing surface because there is no airflow from the lower surface to upper surface. The formation of a trailing vortex behind the midspan of the wing has a significant effect to the airflow at the midspan (Fig. 11(d))

Fig. 11(e) shows the wing with rearward wingtip fence at $\alpha=17°$. It shows that the airflow leap from the lower surface affects the airflow in the mid span. With the increasing angle of attack to $\alpha=19°$ (Fig. 11(f)), the fluid flow in the mid span has been affected by the leakage from lower surface to the upper surface passing through the front of the wingtip more significantly. This irregular flow pattern meets the trailing edge vortices behind the mid span.

III.3. Turbulence Intensity

In Fig. 12(a), the turbulence intensity of the plain wing at $\alpha=16°$ is shown. On the wingtip area, hight turbulence intensity widens, due to the leakage of the fluid flow at the leading edge of the wingtip and slightly shifting towards the trailing edge. At the midspan area, turbulence intensity increases on leading edge while on the trailing edge, high turbulence intensity area decreases.

In Fig. 12(b), the turbulence intensity of wing with forward wingtip fence at $\alpha=16°$ is shown.

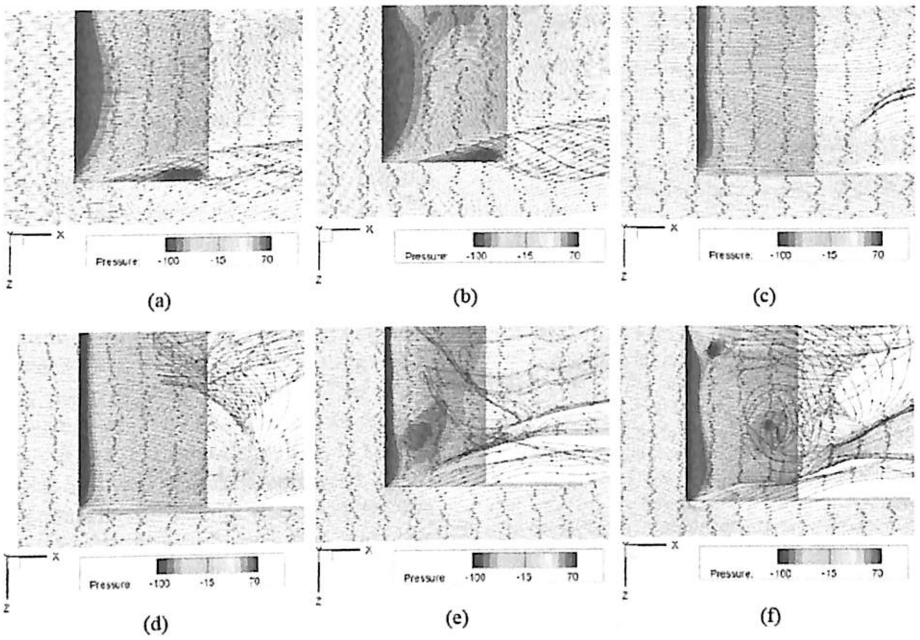

(a) (b) (c)

(d) (e) (f)

Figs. 11. Velocity Pathline Structure (a) Plain Wing α=17° (b) Plain Wing α=19° (c) Forward Wingtip Fence α=17° (d) Forward Wingtip Fence α=19° (e) Rearward Wingtip Fence α=17° (f) Rearward Wingtip Fence α=19°

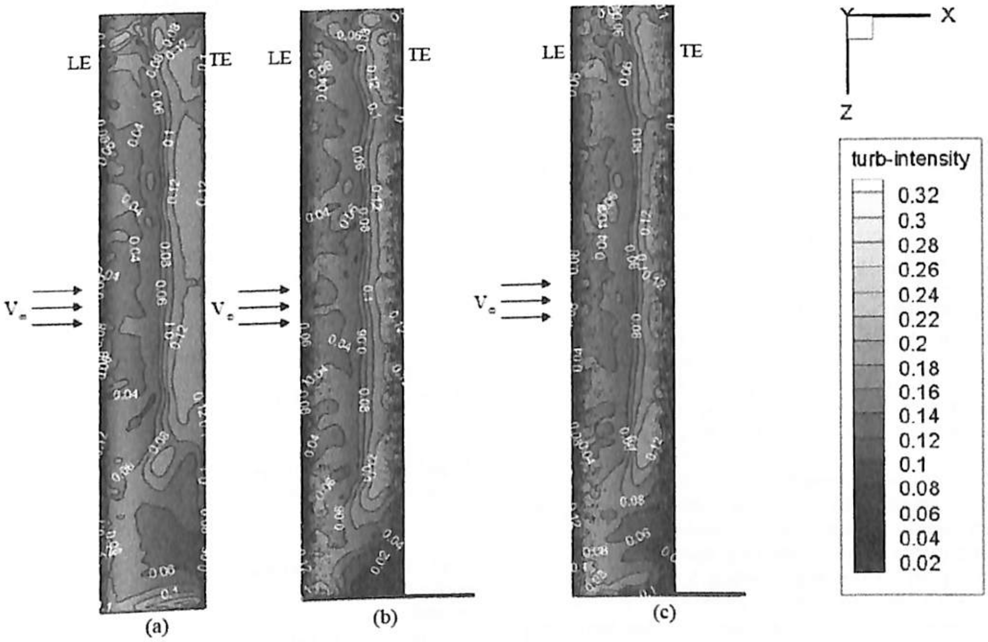

(a) (b) (c)

Figs. 12. Turbulent Intensity Contour (LE = Leading Edge, TE = Trailing Edge) (a) Plain Wing α=16° (b) Forward Wingtip Fence α=16° (c) Rearward Wingtip Fence α=16°

At the wingtip, there is a decrease in turbulence intensity compared to plain wing. This shows that fluid flow leakage from the lower surface to the upper surface on the wingtip can be properly retained by the forward wingtip fence. This is marked by the narrowing of the high turbulence intensity area.

In Fig. 12(c), the turbulence intensity of wing with rearward wingtip fence at α=16° is shown. On the wingtip, the area with high turbulence is expanding, due to the leakage of fluid flow at the leading edge corner of the wingtip. Low turbulence intensity at wingtip area is no longer seen because the fluid flow jump tends to the rearward wingtip fence area.

IV. Conclusion

Vorticity magnitude increases with the increase of the angles of attack. With the addition of a winglet, the vorticity magnitude of the plain wing can be distributed into smaller size and reduced intensity. This is due to the function of the winglet to prevent the fluid jump from the lower surface to the upper surface. With the increasing angle of attack to α = 19°, the vorticity magnitude area behind the plain wing with rearward wingtip fence has increased rapidly and wider than plain wing. This phenomenon can be explained by looking at the streamline of the corner leading edge. The fluid flow in the midspan has the effect of the leakage from lower surface to the upper surface passing through the leading edge of the wingtip becomes more apparent. Wing with forward wingtip fence results in a much narrower size vorticity magnitude than plain wing and rearward wingtip fence. Forward wingtip fence succeeds in reducing "jump" of the fluid flow from the lower surface to the upper surface although the vorticity magnitude area increases as the angle of attack increases. This study uses the minimum speed used in UAV. In future studies it would be better to use the maximum speed on UAV.

The type of meshing used can be compared using structural meshing (quadriateral mesh) which covers the entire model. However, it will increase the elements used. The use of turbulence models can also be compared with the other turbulence models, for example k-ε Standard, k-ε RNG or k-ε Realizable.

Acknowledgements

This work was supported by Grant from Sepuluh Nopember Institute of Technology due to sponsored this paper.

References

[1] Kontogiannis, Spyridon G., Ekaterinaris, John A., Design, Performance Evaluation and Optimization of a UAV. Science Direct. *Aerospace Science and Technology*. Volume 29, Issue 1, August 2013. Pages 339-350.
doi: http://dx.doi.org/10.1016/j.ast.2013.04.0025

[2] Gavrilovic, Nikola N. Boško P. Rašuo; George S. Dulikravich. Vladimir B. Parezanović, Commercial Aircraft Performance Improvement Using Winglet. *FME Transaction* Vol. 43, No 1, 2015.

[3] Hariyadi. Setyo., Sutardi. Aries Widodo. Wawan, Numerical Study of Aerodynamic Analysis on Wing Airfoil NACA 43018 with the addition of Forward and Rearward Wingtip Fence, 2016 *AIP Conference Proceedings 1778*, 030011.
doi: 10.1063/1.4965745

[4] Kontogiannis, S. G., Mazarakos, D. E., Kostopoulos, V., ATLAS IV Wing Aerodynamics Design : Form Conceptual Approach to Detailed Optimization. Elsevier Science Direct : *Aerospace Science and Technology*. Volume 56, September 2016, Pages 135-147.
doi: http://dx.doi.org/10.1016/j.ast.2016.07.002

[5] Hariyadi. Setyo., Sutardi. Aries Widodo, Wawan, Numerical Study Of Flow Characteristics Around Wing Airfoil Eppler 562 with Variations Of Rearward Wingtip Fence. *AIP Conference Proceedings 1983*. 020011 (2018).
doi: 10.1063/1.5046207

[6] Hariyadi, Setyo., Sutardi, Aries Widodo, Wawan. Drag reduction analysis of wing airfoil E562 with forward wingtip fence at cant angle variations of 75° and 90°. *AIP Conference Proceedings 2001*, 050003 (2018).
doi: 10.1063/1.5049994

[7] Gölcük. A. I.. D. F. Kurtulus. Winglet Design and Analysis for Low-Altitude Solar-Powered UAV. *Int. J. Sustainable Aviation*, Vol. 3, No. 1, pp. 64-86, 2017.

[8] Menter, F. R.. Kuntz. M.. Langtry. R.. Ten Years of Industrial Experience with the SST Turbulence Model. *Proceedings of the 4th International Symposium on Turbulence, Heat and Mass Transfer*, pp. 625-632, 2003.

[9] Miranda, Wendel Rodrigues, André Luiz Tenório Rezende, RANS Models Applied In A Flow Over A Rounded Edge. *22nd International Congress of Mechanical Engineering (COBEM 2013)*, November 3-7, 2013. Ribeirão Preto. SP. Brazil, pp. 8689-8697. 2013.

[10] Menter. F. R., Influence of Free Stream Values on k-ω Turbulence Model Predictions, *AIAA Journal*, Vol. 30, No. 6, pp. 1657-1659, 1992.

[11] Fluent Inc. *FLUENT 6.3. User Guide*, 2007

[12] Sunil. A., Tide. P., An Investigation on Suppression of Vortex Instabilities for Flow Past a Bluff Body Using a Passive Device. (2017) *International Review of Mechanical Engineering (IREME)*, 11 (2). pp. 132-137.
doi: https://doi.org/10.15866/ireme.v11i2.10833

[13] Rostane, B., Aliane, K., Abboudi. S., Three Dimensional Simulation for Turbulent Flow Around Prismatic Obstacle with Rounded Downstream Edge Using the k-ω SST Model. (2015) *International Review of Mechanical Engineering (IREME)*, 9 (3), pp. 266-277. doi: https://doi.org/10.15866/ireme.v9i3.5719

[14] Ahmed, S., Nazari, A., Numerical Analysis of Boundary Layer Separation Control. (2015) *International Review of Mechanical Engineering (IREME)*, 9 (1), pp. 90-96.
doi: https://doi.org/10.15866/ireme.v9i1.4490

[15] Mulvany, Nicholas J., Li Chen, Jiyuan Y. Tu, Brendon Anderson. *Steady State Evaluation of Two Equation RANS Turbulence Models for High Reynolds Number Hydrodynamic Flow Simulations, Final Report*. Defence Science and Technology Organisation. Departement of Defence, Australian Goverment, 2004

[16] Anderson. J. D., Jr., *Computational Fluid Dynamics*, Mc-Graw Hill. New York. 1995

[17] White. Frank M., *Fluid Mechanics 7th ed.*, Mcgraw-Hill. 2009

[18] Fluent 6.2 Documentation File. ANSYS Manual, 2006.

[19] A. Gerasimov. Modeling *Turbulent Flows with FLUENT*, Europe, ANSYS, Inc. 2006.

[20] Salim .M. Salim, S.C. Cheah, Wall y+ Strategy for Dealing with Wall-bounded Turbulent Flows. Proceedings of the International *MultiConference of Engineers and Computer Scientists 2009*, March 18 - 20. 2009, Hong Kong. Vol II IMECS, 2009.

[21] ANSYS Meshing. Meshing Quality Apendix A, 2009.

[22] Turanoğuz. Eren. Design Of A Medium Range Tactical UAV And Improvement Of Its Performance By Using Winglets, 2015 *International Conference on Unmanned Aircraft Systems (ICUAS)*, 2015.

[23] Manzoor, M., Maqsood. A., Hasan. A., Quadratic Optimal Control of Aerodynamic Vectored UAV at High Angle of Attack. (2016) *International Review of Aerospace Engineering (IREASE)*. 9 (3). pp. 70-79.
doi:https://doi.org/10.15866/irease.v9i3.8119

[24] Alias, M., Mohd Rafie, A., Wiriadidjaja, S., Two Dimensional Numerical Study of Aerodynamic Characteristic for Rotating Cylinder at High Reynolds Number, (2016) *International Review of Aerospace Engineering (IREASE)*, 9 (6). pp. 208-215.
doi:https://doi.org/10.15866/irease.v9i6.10774

[25] Alsahlani. A., Rahulan, T., A Mathematical Model of a Conceptual Design Approach of High Altitude Solar Powered Unmanned Aerial Vehicles, (2017) *International Review of Aerospace Engineering (IREASE)*. 10 (4), pp. 196-206.
doi:https://doi.org/10.15866/irease.v10i4.11774

[26] Aziz, M., Elsayed. A., CFD Investigations for UAV and MAV Low Speed Airfoils Characteristics. (2015) *International Review of Aerospace Engineering (IREASE)*, 8 (3), pp. 95-100.
doi:https://doi.org/10.15866/irease.v8i3.6212

[27] Bousson, K., Gameiro. T., A Quintic Spline Approach to 4D Trajectory Generation for Unmanned Aerial Vehicles. (2015) *International Review of Aerospace Engineering (IREASE)*, 8 (1). pp. 1-9.
doi:https://doi.org/10.15866/irease.v8i1.4780

[28] Belhadri. K., Kouadri. B., Zegai. M., Adaptive Neural Control Algorithm Design for Attitude Stabilization of Quadrotor UAV. (2016) *International Review of Automatic Control (IREACO)*. 9 (6). pp. 390-396.
doi:https://doi.org/10.15866/ireaco.v9i6.9919

[29] Carloni, G., Bousson, K., A Nonlinear Control Method for Autonomous Navigation Guidance, (2016) *International Review of Civil Engineering (IRECE)*, 7 (4), pp. 102-113. doi:https://doi.org/10.15866/irece.v7i4.10757

[30] Kasyanov, P.O., Toscano, L., Zadoianchuk, N.V., Topological properties of strong solutions for the 3D Navier-Stokes equations, (2014) *Solid Mechanics and its Applications*, 211, pp. 181-187.

[31] Kasyanov, P.O., Toscano, L., Zadoianchuk, N.V., A criterion for the existence of strong solutions for the 3D Navier-Stokes equations, (2013) *Applied Mathematics Letters*, 26 (1), pp. 15-17.

Authors' information

[1]Sepuluh Nopember Institut of Technology, Aviation Polytechnic of Surabaya, Indonesia, Jemur Andayani I/73 Wonocolo Surabaya 60236 Indonesia.

[2]Mechanical Engineering Department, Faculty of Industrial Technology, Sepuluh Nopember Institut of Technology, Jl. Arief Rahman Hakim, Surabaya 60111 Indonesia.

[3]Shipbuilding Institute of Polytechnic Surabaya, Indonesia.

Setyo Hariyadi S. P. received Bachelor Degree and Master Degree from Mechanical Engineering Department, Faculty of Industrial Technology Sepuluh Nopember Institute of Technology Surabaya Indonesia. Currently, he is continuing his Doctoral Degree in the same department with the field of Energy Conversion Engineering. Areas of interest are aerodynamics, drag reduction, CFD and fluid mechanics. He works as a lecturer at Aircraft Engineering Aviation Polytechnic of Surabaya.
E-mail: hudzaifahsetyo@gmail.com

Sutardi received a Bachelor Degree from the Mechanical Engineering Department, Faculty of Industrial Technology Sepuluh Nopember Institute of Technology. He obtained Master Degree and Doctoral Degree from Memorial University of Newfoundland, St. Johns, Canada. Currently he teaches at the Mechanical Engineering Department Faculty of Industrial Technology Sepuluh Nopember Institute of Technology Surabaya Indonesia in Fluid Mechanics, Turbulent Flow, Viscous Fluid Flow, Cooling Technique, and Turbo Machinary. The research areas involved are drag reduction methods, the study of boundary layer characteristics for several surfaces, the study of simulation methods and the visualization of fluid flow.
E-mail: sutardi@me.its.ac.id

Wawan Aries Widodo received Bachelor Degree, and Master Degree from from Mechanical Engineering Department, Faculty of Industrial Technology Sepuluh Nopember Institute of Technology Surabaya Indonesia. He obtained Doctoral Degree from the Marine Engineering Department, Faculty of Marine Technology Sepuluh Nopember Institute of Technology Surabaya Indonesia. Currently he teaches at Mechanical Engineering Department, Faculty of Industrial Technology Sepuluh Nopember Institute of Technology Surabaya Indonesia in Fluid Mechanics, Introduction to Mechanical Engineering, Power Generation System, and CFD. The research areas are aerodynamics, passive flow control, CFD, simulation method study and fluid flow visualization.
E-mail: wawanaries@me.its.ac.id

Muhammad Anis Mustaghfirin received Bachelor Degree, and Master Degree from from Mechanical Engineering Department, Faculty of Industrial Technology Sepuluh Nopember Institute of Technology Surabaya Indonesia. He obtained Doctoral Degree from the Mechanical Engineering Department, Saga University, Japan. Currently, he teaches at Marine Engineering, Shipbuilding Institute of Polytechnic Surabaya Indonesia in Fluid Machine, Finite Element Methode, Cooling Technique, and CFD. The research areas are Thermodynamics, CFD, and Heat Transfer.
E-mail: mustaghfirin@gmail.com

ise Worthy Prize

International Review of Mechanical Engineering (I.RE.M.E.), Vol. 12, N. 10
ISSN 1970 - 8734
October 2018

Self-Consistent Approach in Elasto-Viscoplasticity of Heterogeneous Materials

E. Boulhafa, R. Kouddane, H. Ouadfel

Abstract – *The objective of this work is to describe the Elasto-viscoplastic behavior of heterogeneous polycrystalline materials by a simple and operational self-consistent approach. This approach is based on the solution of the viscoelastic inclusion problem that has been confirmed by Hashin's results. In this paper, the case of polycristal, whose behavior contains, locally, a nonlinear viscous part, is studied. The linearization of this behavior is done through tangent tensor. As an initial step, the 1-site solution is studied. In order to study an isotropy induced by some topological effects, an extension to the N-site solution is performed. Finally, some results of the model are presented. In order to test the capability of the present model to reproduce certain phenomena observed experimentally, cyclic loadings results are also presented.*

Keywords: *Viscoelastic, Inclusion, Self-consistent, 1-Site, N-Site, Interaction Tensor*

Nomenclature

	Constraint deviating tensor
	Macroscopic constraint deviating tensor
	Macroscopic Constraint rate deviating tensor
g	Constraint rate deviating tensor of grain g
	Tensor homogeneous to Constraint deviating tensor
	Tensor homogeneous to Constraint rate deviating tensor
	Strain rate tensor
	Macroscopic strain rate tensor
	Interaction tensor
	Tangent Modulus tensor
	Tensor related to tensor of elastic constants
	Hardening matrix
	Tensor of elastic constants
	Error related to strain rate
	Shear modulus
	Coefficient of viscosity
	Slip system
s	Normal to the slip plane
s	Slip direction on the slip system
s	Resolved cission
s	Reference constraint
s	Plastic slip rate
0	Reference sliding velocity
	Coefficient of sensitivity to the velocity
eq	Macroscopic equivalent constraint
g	Volumic fraction

I. Introduction

The role of the different scales in the mechanics of materials is now well established. At the material level, the characteristic scale of interest is the one of microstructural heterogeneities and defects. The mechanics and physics of these multiphasic microstructures is generally considered the main mechanism describing the behavior of the material response. The understanding of the behavior, evolutions and the mechanical response at the microstructural scale is therefore critical. It is now well understood that even very small scales and thin interfaces can influence a macroscopic behavior. Multi-scale methods have emerged to link small and large scales in solid mechanics. Nonlinear homogenization of heterogeneous materials has been one of the first multi-scale approaches, but it has quickly proved to be insufficient to address more complex microstructures, non-linear behaviors, and to describe local phenomena in microstructures. In order to achieve these goals, multi-scale numerical methods have been developed in recent decades. The first work in homogenization goes back to the work of Voigt [1], followed by the models of Sachs [2], Reuss and Taylor [3]. Although the Voigt and Reuss bounds have been developed for composites, the Sachs and Taylor models have been proposed for polycrystals.

The growing interest in composites during the 20th century has motivated important developments in homogenization. The most notable contribution has been the one of Eshelby [4], whose attention has been focused on the elastic solution for ellipsoidal inclusion.

This theme, later called micromechanics, has been formally established by Hill [5]. For years, several authors have approached the problem of inclusion for

https://doi.org/10.15866/ireme.v12i10.15586

different purposes [6]-[8] such as:

- modeling the behavior of polycristal
- calculation of stress concentrations
- Initiation of damage

Gilormini [9] has done a review of the work performing on these problems. Progress in homogenization of heterogeneous materials has been provided by Kroner [10], Hashin and Shtrikman [6], Hill [5], Mori and Tanaka [11]..., among others. The first steps towards extensions to the nonlinear case have been developed by Hill [5] or Hutchinson [12].

The behaviors discussed included elasto-plasticity, non-linear elasticity and viscoelasticity. More recently, several important contributions have been made by Nemat-Nasser [13], Ponte Castaneda [14], Suquet [15], or Zaoui [16], among others. In recent years, major advances have been made in the introduction of numerical methods in homogenization approaches, particularly to remove the locks associated with complex nonlinear behaviors in heterogeneous materials, as well as to provide usable models. in structural calculations for engineers.

Thus, "numerical" homogenization methods have been proposed, where the Self-consistent scheme comes down to the evaluation of mechanical interactions between inclusion and an equivalent homogeneous medium and it has been successful in obtaining the effective properties at a low concentration. In order to determine the effective properties, only the volumic fraction of the constituents of the inhomogeneous medium has been introduced.

Nevertheless, the discrete mechanical interactions cannot be taken into account because there is no distinction between phases. In order to take into account such kind of effects, N-Site Self-consistent model has been proposed.

In this paper, the main aim is to describe the Elasto-viscoplastic behavior of a polycristal. First, linear viscoelastic behavior has been considered as a basic example in the development of the interaction models between the grain and its environment.

Then, the application to the case of heterogeneous materials has been developed and the extension to non-linear behavior has been exposed. Two formulations have been developed; the 1-site formulation where the topological effects are neglected and the N-site formulation that makes possible to take into account a certain anisotropy induced by a certain topology of the grains. A cluster has been developed to account for a better description of the interaction of a grain with its neighbors.

II. Micromechanical Modeling

II.1. *Approximate Homogenization Scheme*

The aim of this study is to propose a simple method of homogenization [17], [18]. It has been assumed that the behavior of the aggregate is isotropic and a Maxwell law [19] approximates it:

$$\dot{\bar{S}}_{ij}(t) = 2\mu^0 \bar{D}_{ij}(t) - \frac{\mu^0}{\eta^0(t)}\bar{S}_{ij}(t) \tag{1}$$

where $\bar{D}$ and $\bar{S}$ are respectively the macroscopic strain rate and the macroscopic constraint deviating tensor, η^0 and μ^0 are mechanical characteristics of matrix (Fig. 1).

The viscosity $\eta^0(t)$ has been taken as an internal parameter depending on the history of the deformation.

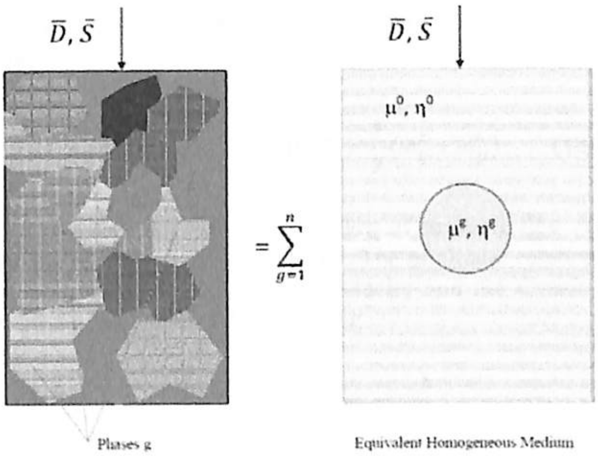

Fig. 1. Modeling of a Polycristal

For each phase g, the following interaction law [20], [21] describes the interaction with the matrix:

$$\dot{S}^g_{ij} - \dot{\bar{S}}_{ij} + \frac{\mu^0}{\eta^0(t)}(S^g_{ij} - \bar{S}_{ij}) = 3\mu^0(\bar{D}_{ij} - D^g_{ij}) \tag{2}$$

with local law:

$$\dot{S}^g_{ij}(t) + \frac{\mu^g}{\eta^g}S^g_{ij}(t) = 2\mu^g D^g_{ij}(t) \tag{3}$$

The scheme of calculation of the parameter η^0 is as follows: the macroscopic strain rate $\bar{D}_{ij}$ is known; at time t, both $\bar{S}_{ij}(t)$ and $S^g_{ij}(t)$ are assumed to be known for each grain g of the polycristal $(g = 1..N)$; the parameter $\eta^0(t)$ is adjusted in order to satisfy the self-consistent condition:

$$\langle D_{ij} \rangle = \bar{D}_{ij} \tag{4}$$

where $\langle \cdot \rangle$ represents the average volume. Satisfying exactly the condition of self-consistent on the five components of the deformation velocity is not generally possible, since only the scalar η^0 can be adjusted.

In the numerical scheme, η^0 is calculated in such a way that the relative error E is minimal:

$$E = \left\| \langle D_{ij} \rangle - \bar{D}_{ij} \right\| / \left\| \bar{D}_{ij} \right\| \tag{5}$$

where the norm $\|\cdot\|$ is defined by:

$$\bar{\sigma}_{eq} = \left(\frac{3}{2} \bar{S}_{ij} \bar{S}_{ij} \right)^{\frac{1}{2}} \tag{6}$$

In all applications considered here, this error does not exceed a few hundredths. Under certain circumstances, the self-consistent condition is exactly satisfied (example of traction or compression). Thanks to isotropy and incompressibility, if the condition of self-consistent is satisfied for one component, it will be satisfied for the others. Moreover, if this condition is satisfied for all $t \geq 0$ it follows immediately from the law of interaction (2) that the self-consistent condition will also be for constraints:

$$\langle S_{ij} \rangle = \bar{S}_{ij} \tag{7}$$

$\eta^0(t)$ is determined as well as $\dot{\bar{S}}_{ij}(t)$ and $\dot{S}^g_{ij}(t)$; $\bar{S}_{ij}(t + \Delta t)$ and $S^g_{ij}(t + \Delta t)$ could be calculated in an incremental manner. The asymptotic values of $\eta^0(t)$ are given by:

$$\lim_{t \to 0} \eta^0(t) = \eta^* \text{ with } \frac{1}{\eta^*} = \sum_{g=1}^{N} f_g \frac{1}{\eta^g} \tag{8}$$

$$\lim_{t \to \infty} \eta^0(t) = \eta^* \text{ with } \sum_{g=1}^{N} f_g \frac{5\eta^*}{3\eta^* + 2\eta^g} = 1 \tag{9}$$

For the numerical simulations, the shear modulus $\mu^g = \mu$ is taken as uniform and it is equal to 240 MPa.

II.2. Constitutive Law of Polycristal

Regarding elastoplastic materials, it is well known that the behavior is of an incremental nature [22], [33]. Following, the viscous nature of its behavior will be taken into account [22]. The time parameter that will intervene in relations constitutes a useful variable for the description of the physical or mechanical quantities and it will naturally correspond to the physical time. As in some models [23] and [24], it is assumed that the plastic slip rate $\dot{\gamma}^s$ on a slip system s is related to the resolved scission τ^s on this system by a power law:

$$\tau^s / \tau_0^s = \left(\dot{\gamma}^s / \dot{\gamma}^0 \right)^m \tag{10}$$

The parameter m is the coefficient of sensitivity to the velocity. τ^s is related to the Cauchy constraint deviating tensor S_{ij} by the relation:

$$\tau^s = m^s_{ij} S_{ij} \text{ with } m^s = b^s \otimes n^s \tag{11}$$

n^s and b^s are respectively the normal slip plane and the slip direction on the slip system. τ^s_0 and $\dot{\gamma}^0$ represent respectively the reference constraint and the reference sliding velocity. The anelastic deformation velocity Tensor D^{an}_{ij} is related to the microscopic shear rates by:

$$D^{an}_{ij} = \sum\nolimits_s R^s_{ij} \dot{\gamma}^s \text{ with } R^s_{ij} = \frac{1}{2}(m^s_{ij} + m^s_{ji}) \tag{12}$$

Using the relations above, the law of anelastic flow of the single crystal can be deduced. The nonlinear relation between anelastic deformation velocity and the Cauchy stress deviator gives following law:

$$D^{an}_{ij} = \dot{\gamma}^0 \sum\nolimits_s R^s_{ij} \left(\frac{R^s_{kl} S_{kl}}{\tau^s_0} \right)^{\frac{1}{m}} \tag{13}$$

The variation of τ^s_0 as a function of time characterizes the intra-crystalline microscopic hardening and the variations of R^s_{ij} are related to changes in the orientations of the crystal lattice.

Locally, the law of behavior is given by the equation (tangent viscoplastic behavior):

$$S_{ij} = A_{ijkl} D_{kl} - H_{ijkl} \dot{S}_{kl} + S'_{ij} \tag{14}$$

where $A_{ijkl}(r)$ and $S'_{ij}(r)$ are dependent on the position r. Each grain $A_{ijkl}(r)$ and $S'_{ij}(r)$ depends on the microscopic hardening and orientation of the grain.

The main approach is as follows: a macroscopic strain rate $\bar{D}_{ij}$ is imposed on the polycristal in order to know the local strain rate gradient. The macroscopic constitutive law is represented by the tangent viscoplastic behavior:

$$\bar{S}_{ij} = A^0_{ijkl} \bar{D}^{an}_{kl} + S'^0_{ij} \tag{15}$$

$\bar{D}^{an}_{ij}$ is the macroscopic non-elastic strain rate. The following constitutive law governs the macroscopic elastic behavior:

$$\dot{\bar{S}}_{ij} = C^0_{ijkl} \bar{D}^e_{kl} \tag{16}$$

By combining the two last equations, the law of macroscopic Elasto-viscoplastic behavior can be drawn:

$$\bar{S}_{ij} = A^0_{ijkl}\bar{D}_{kl} - H^0_{ijkl}\dot{\bar{S}}_{kl} + S'^0_{ij} \tag{17}$$

with:

$$H^0_{ijkl} = A^0_{ijmn}(C^0_{mnkl})^{-1}$$
$$B^0_{ijkl} = (H^0_{ijkl})^{-1}$$
$$S''^0_{ij} = B^0_{ijkl}S'^0_{kl}$$

It can be noted the analogy of this last application with that used for the linear viscoelastic material. Taking into account the results of the previous section, the following law is obtained:

$$D_{ij} = \bar{D}_{ij} + \Gamma^*_{ijkl}(\tilde{S}'_{kl} - \tilde{B}_{ijkl}S_{kl}) \tag{18}$$

with:

$$\tilde{B}_{ijkl}(r) = B_{ijkl}(r) - B^0_{ijkl}$$
$$\tilde{S}'_{ij}(r) = S''_{ij}(r) - S''^0_{ij}$$

Compared to the different solutions of the integral equation (18), the self-consistent approach in the case of linear elasticity is a reasonable compromise between systematic statistical methods and uniform field approximations. The systematic statistical methods are difficult to implement and they are not necessarily justified with respect to the simplifications used to describe single crystal. The uniform field approximations systematically neglect any heterogeneity including intergranular. In the presented modeling approach, the polycristal is considered to be single-phase and it consists of grains of different crystallographic orientations. Since the correlation between the grain orientations is weak, authors are close to the hypothesis of the perfect disorder in the material and the 1-Site self-consistent scheme is a suitable homogenization tool. A first approximation is obtained by assuming that the Elasto-viscoplastic behavior is uniform in each grain, which, obviously, ignores the intra-granular heterogeneities, which, under certain circumstances, appears in the grain. Under these conditions, the uniformity hypothesis of D_{ij} in each grain can be written in the form:

$$D_{ij}(r) = \sum\nolimits_g D^g_{ij}\Delta_g(r) \tag{19}$$

where Δ_g is the characteristic function of the grain g defined by:

$$\Delta_g(r) = 1 \text{ if } r \in V_g \text{ else } 0$$

D^g_{ij} is the uniform strain rate in V_g. Similarly D^{gan}_{ij} is assumed uniform in V_g. Since A_{ijkl} and S'_{ij} depend on D^{an}_{ij}, it is:

$$A_{ijkl}(r) = \sum\nolimits_g A^g_{ijkl}\Delta_g(r)$$
$$S'_{ij}(r) = \sum\nolimits_g S'^g_{ij}\,\Delta_g(r)$$

The combination of the equations above results in:

$$D^g_{ij} = \bar{D}_{ij} + \Gamma^{gg}_{ijkl}(\tilde{S}''_{kl} - \tilde{B}_{klmn}S_{mn})^g + \\ + \sum\nolimits_{g \neq g'} \Gamma^{gg'}_{ijkl}M^{g'}_{kl} \tag{20}$$

where:

$$\Gamma^{gg'}_{ijkl} = \frac{1}{V_g}\int_{V_g}\int_{V_{g'}} \Gamma_{ijkl}(r - r')drdr'$$
$$M^{g'}_{ij} = (\tilde{S}''_{ij} - \tilde{B}_{ijkl}S_{kl})^{g'}$$

II.3. Self-Consistent Scheme 1 Site

The expression (20) constitutes a system of unknowns D^g_{ij} whose rank is equal to the number of grains considered. If the polycristal is not very heterogeneous, then the contribution of terms such as:

$$\Gamma^{gg'}_{ijkl}(\tilde{S}''_{kl} - \tilde{B}_{klmn} : S_{mn})^{g'}$$

Taking $\tilde{B}_{ijkl} = 0$ and $\tilde{S}''_{kl} = 0$ the following interaction equation is obtained:

$$\dot{S}^g_{ij} - \dot{\bar{S}}_{ij} + B^0_{ijkl}(S^g_{kl} - \bar{S}_{kl}) = \\ [(\Gamma^I_{ijkl})^{-1} + C^0_{ijkl}](D^g_{kl} - \bar{D}_{kl}) \tag{21}$$

This law of interaction is similar to the law (2); in fact, it takes into account an instantaneous elastic response and a delayed viscoplastic relaxation. Moreover, when the elasticity is neglected $C^0_{ijkl} \to +\infty$ this same law is identical to the one obtained by Molinari et al. [25] in their viscoplastic formulation in large deformations. In Figs. 2 and 3, the equivalent strain-stress curves for tension and compression tests is presented. The results are compared with the ones of the viscoplastic Lin and Taylor model. The self-consistent model predicts constraints below that obtained by the Lin model. It can be observed that Lin-Taylor models overestimate equivalent stresses for both tension and compression cases.

This model does not take into account mutual interactions between grains: intergranular accommodation is no longer ensured. Moreover, the model presented here (tangent formulation) yields results that are in good agreement with those obtained by Molinari [26] for viscoplasticity.

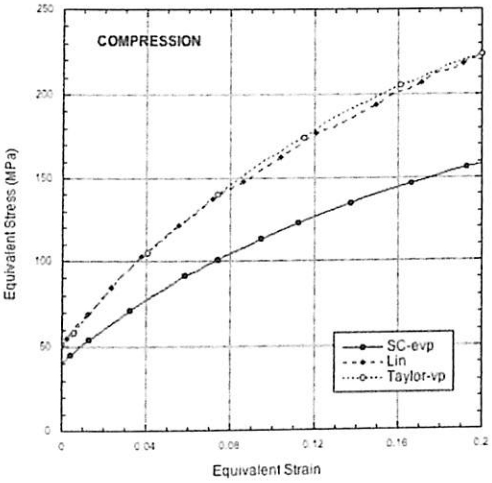

Fig. 2. Evolution of stress as a function of deformation in case of compression.

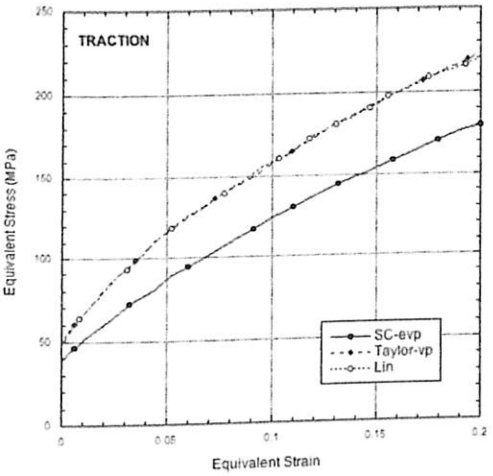

Fig. 3. Evolution of stress as a function of deformation in case of tension

II.4. Self-Consistent Scheme N Site

In this part, the solution of (20) is approached by a self-consistent solution of cluster type by limiting the sum not to the grain itself but also to its first neighbors.

Taking into account that the representative volume is formed of n grains and that the cluster is formed of n_c grains (see Fig. 4), the set of grains g' which interact with the grain g is characterized by I_g^c :

$$I_g^c = \{g' \ / \ V_{g'} \in \text{Cluster attached } to \ V_g\}$$

The whole space is covered by reproducing the representative volume by periodicity. Reference may be made to [27] to see how the representative volume is constructed. In the presented case, the situation will be simpler, since the cells are in the form of identical spheres. For illustration, the situation will be commented in a two-dimensional case so as not to complicate the writing of the equation (20). The representative volume consists of 16 grains (1, 2 ... 16) of spherical shape (Fig. 4).

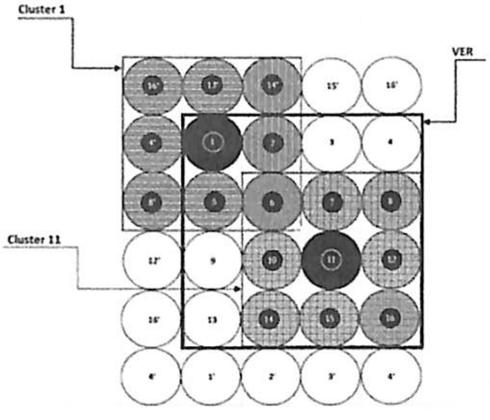

Fig. 4. Representative volume (16 grains) and cluster (9 grains)

For the cluster associated with Grain 11, all cluster elements are included in the representative volume. Following, equation (20) is written for grain 11:

$$\begin{aligned} D_{ij}^{11-11} &= \bar{D}_{ij} + \Gamma_{ijkl}^{11-11} M_{kl}^{11} + \Gamma_{ijkl}^{11-6} M_{kl}^{6} + \\ &+ \Gamma_{ijkl}^{11-7} M_{kl}^{7} + \Gamma_{ijkl}^{11-8} M_{kl}^{8} + \Gamma_{ijkl}^{11-10} M_{kl}^{10} + \\ &+ \Gamma_{ijkl}^{11-12} M_{kl}^{12} + \Gamma_{ijkl}^{11-14} M_{kl}^{14} + \\ &+ \Gamma_{ijkl}^{11-15} M_{kl}^{15} + \Gamma_{ijkl}^{11-16} M_{kl}^{16} \end{aligned} \tag{22}$$

For the cluster associated with grain 1, some of the cluster elements are outside the representative volume. The condition of periodicity makes it possible to define the external elements. This gives:

$$\begin{aligned} D_{ij}^{1-1} &= \bar{D}_{ij} + \Gamma_{ijkl}^{1-1} M_{kl}^{1} + \Gamma_{ijkl}^{1-2} M_{kl}^{2} + \Gamma_{ijkl}^{1-5} M_{kl}^{5} \\ &+ \Gamma_{ijkl}^{1-6} M_{kl}^{6} + \Gamma_{ijkl}^{1-8'} M_{kl}^{8} + \Gamma_{ijkl}^{1-4'} M_{kl}^{4} + \Gamma_{ijkl}^{1-16'} M_{kl}^{16} \\ &+ \Gamma_{ijkl}^{1-13'} M_{kl}^{13} + \Gamma_{ijkl}^{1-14'} M_{kl}^{14} \end{aligned} \tag{23}$$

By writing equation (20) for all grains, a system of equations is obtained, in order to determine the different rates of deformation D_{ij}^{g}.

III. Cyclic Load

In order to test the capability of the model to reproduce certain phenomena observed experimentally, authors tried to simulate the response of the polycristal to a cyclic loading.

The mechanical characteristics of the polycristal are the same as for monotonic loadings. The phenomenon of attachment of the small cycle in the large cycle has been systematically examined by [28] on several materials and it can be considered as a general phenomenon. For this purpose, a cyclic test is carried out in tension-compression with controlled deformation.

After stabilization, a cycle of lower amplitude is realized during a transient and then returned to normal loading. It can be observed that the small cycle always remained attached to the branch of the large cycle at which it was made. In other words, after discharging and compression flow, the pre-existing state at the start of the discharge is not forgotten, since the embedded cycle returns almost exactly to this point without exceeding it, then taking a path very close to Transitional period. This phenomenon is repeated in all cases. Everything happens as if the material has memorized the mini-maxi of the previous load. Unlike the phenomenological model [29], this phenomenon is well reproduced by the self-consistent model [30], (Fig. 5).

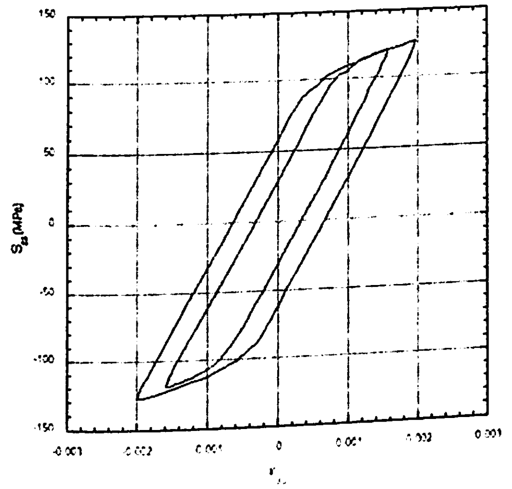

Fig. 5. Snapping the small cycle in the great cycle - Symmetrical amplitude

IV. Conclusion

The linear viscoelastic self-consistent scheme, based on the approximation of the global behavior by Maxwell law and where the viscosity η^0 is taken as a parameter depending on the history of the deformation, seems to give a reasonable approach to the problem of homogenization. In this paper, it has been shown how it is possible to:

- Extend the model to cases of polycrystalline materials and
- Applied the 1-Site tangent formulation for different loadings.

The results of the presented Elasto-viscoplastic model confirm those given by the viscoplastic self-consistent approach [25]. For grains having a spherical shape presenting a periodical network, an extension to the (N-sites) analysis has been performed. It has been shown that this approach, unlike the one of 1-Site, makes it possible to take an anisotropy induced by a particular topology of the grains [31], [32]. Finally, this approach shows the capability of the model to reproduce certain phenomena observed experimentally, in particular the attachment of a small cycle in a large cycle during cyclic loading.

References

[1] W. Voigt. *Wied Ann.*, 38 (1889).

[2] G. Sachs 1928. *Z. Verein Deut Ing.* Vol. 72, p. 734

[3] G. I. Taylor. 1938. Plastic Strain in Metals *J. Inst. Metals.* Vol. 62. p. 143

[4] J. D. Eshelby, 1957, The Determination of the Elastic Field of an Ellipsoidal Inclusion, and Related Problems *Pro. Roy. Soc.* A241. p.376.

[5] R. Hill. 1965, A self-consistent mechanics of composite materials, *J. Mech. Phys. Sol.*, Vol. 13, p. 89.

[6] Z. Hashin, the inelastic inclusion problem. *International Journal of Engineering Science.* Vol. 7. pp. 11-36, 1969.

[7] G. J. Weng, a self-consistent relation for the time-dependent creep of polycrystals. *International journal of plasticity.* Vol. 9. pp. 181-198, 1993.

[8] P. Gilormini, F. Montheillet, deformation of an inclusion in a viscous matrix and induced stress concentrations. *Journal of the Mechanics and Physics of Solids*, Vol. 9. pp. 97-123, 1986.

[9] P. Gilormini, *Le problème de l'inclusion en viscoplasticité. Application à l'amorçage de l'endommagement,* Ph.D. dissertation, Université de Grenoble, France, 1985.

[10] E. Kroner, 1961, *Acta. Met.*, Vol. 9, p. 155

[11] Mori, T., & Tanaka, K., 1973. Average stress in matrix and average elastic energy of materials with misfitting inclusions. *Acta Metall.*, 21(5). 571–574.

[12] J. W. Hutchinson. Elastic-plastic behaviour of polycrystalline metals and composites. 1970, *Proc. Roy. Soc.*, A319. p. 247

[13] Nemat Nasser. 1996. *Journal of Applied Mechanics*, vol. 63, issue 2, p. 561

[14] Castañeda, P. P., Suquet, 1997. Nonlinear Composites. *Advances in Applied Mechanics*, Volume 34, 171–302.

[15] M. Suquet. 1987, Springer-Verlag. *Homogenization techniques for composite media*, 193-278.

[16] A. Zaoui, 1972, *Thèse d'Etat*, Paris

[17] J. Mars, F. Dammak and A. Dhieb, Homogenous Numerical Models for Porous Hyper elastic Materials, *Inter. J. on Adv. Mat. and Tech.* Vol 3, No 1 2015.

[18] Nikhilesh Chawla and Yu-Lin Shen. Mechanical Behavior of Particle Reinforced Metal Matrix Composites, *Advanced engineering materials*, 3, no. 6, 2001.

[19] Wilhelm Flugge, *Viscoelasticity*, Second revision Edition, Springer-Verlag Berlin Heidelberg GmbH 1975.

[20] R. Kouddane, A. Molinari, G. R. Canova, Self-consistent modeling of heterogeneous viscoelastic and elasto-viscoplastic materials, *MECAMAT91*. 1993.

[21] R. Kouddane. *Approche auto-cohérente en élastoviscoplasticité des matériaux hétérogènes*. Ph.D. dissertation, Université de Metz, France, 1994.

[22] Laghzale, N., Bouzid, A., Analytical Modelling of Elastic-Plastic Interference Fit Joints, (2016) *International Review on Modelling and Simulations (IREMOS)*. 9 (3), pp. 191-199. doi: https://doi.org/10.15866/iremos.v9i3.8703

[23] J. W. Hutchinson, Bounds and self-consistent estimates for creep of polycrystalline materials, *Proc. of the Royal Society of London*, 1976, A384. Page 101-127.

[24] R. J. Asaro, A. Needleman, texture development and strain hardening in rate dependent polycrystals, *Acta metallurgica*, Vol. 33. No. 6, pp 923-953, 1985.

[25] A. Molinari, G. R. Canova and S. Ahzi, a self-consistent approach of the large deformation polycrystal viscoplasticity, *Acta metallurgica*, Vol. 35. No. 12 pp. 2983-2994, 1987.

[26] A Molinari, S Ahzi, R Kouddane, on the self-consistent modeling of elastic-plastic behavior of polycrystals, *Mechanics of Materials*, Vol. 26. pp. 43-62, 1997.

[27] M. El Mouden, M. Cherkaoui, A. Molinari, M. Berveiller, the overall elastic response of materials containing coated inclusions in a periodic array, *International Journal of Engineering Science*, Vol. 36. pp. 813-829, 1998.

[28] R. Kouddane, N. Zouhal, GR. Canova, A. Molinari, Complex loading of viscoplastic materials: micro-macro modelling, *Materials Science and Engineering* A175, pp. 31-36, 1994.

[29] M Berveiller, O Fassi-Fehri and A Hihi, The problem of two plastic and heterogeneous inclusions in an anisotropic medium,

International Journal of Engineering Science, Vol. 25. N° 6. pp. 691-709. 1987.

[30] J. L. Chaboche. D. Nouailhas. P. Paulmier and H. Policella. Cyclic inelastic constitutive equations and their impact on the fatigue life predictions, *International Journal of Plasticity*. Vol. 35. pp. 44–66. 2012.

[31] E. Boulhafa. R. Kouddane. H.Ouadfel. Estimation of the effective magnetic permeability of polycristals using a self-consistent scheme. *Proc. of international conference on electronic engineering and renewable energy*. 2018.

[32] Pavlou. D.. An Approximate Method for Stress Analysis in Butt Joints of FRP Pipelines. (2017) *International Review of Mechanical Engineering (IREME)*. 11 (2). pp. 108-113. doi: https://doi.org/10.15866/ireme.v11i2.11072

[33] Hamadache. H.. Amirat. A.. Chaoui. K.. Effect of Diamond Ball Burnishing on Surface Characteristics and Fatigue Strength of XC55 Steel. (2015) *International Review of Civil Engineering (IRECE)*. 6 (6). pp. 156-164. doi:https://doi.org/10.15866/irece.v6i6.8201

Authors' information

Mathematics. Computer Science and Mechanic team. National School of Applied Sciences University Mohammed I. Oujda. Morocco.

Elmahdi Boulhafa received his engineer degree in mechanical engineering in 2010 at the Mohammadia School of Engineers (EMI). Rabat. Morocco. Since 2012 until today. he is an engineer of maintenance in a thermal power plant in Morocco. Head of mechanical service. he is presently pursuing his PhD program in mathematics. computer science and mechanic team at National School of Applied Sciences University Mohammed I. Oujda. Morocco. on the theme "Effective permeability of a three-phase with embedded inclusions. self-consistent approach".

Redouane Kouddane received the Master's degree in Science and Technology in Mechanics from the University of Metz. France. in 1987. and the Ph.D. in Mechanical Engineering from the University of Metz. in 1994. In 1999. he joined the Mechanical Engineering Department of Clemson University. (SC) USA. as a visiting scientist. where he worked on the creep and growth of Zircaloy under irradiation. Since September 1999. he has been working at the National School of Applied Sciences of Oujda. His current research interests include mechanics. structural calculus. micro-macro transitions. and laws of behavior. Pr. Kouddane has developed a micro-mechanical model in elasto-viscoplasticity of heterogeneous materials (Kouddane's Model). He has several contributions in the field of mechanics but also in the field of design and integrated production.

Hamza Ouadfel did the preparatory classes at Hight School Louis Le grand in France before joining the Hight School of Mines in Nancy where he obtained his engineer degree in civil engineering and mining. After that. he joined the University of Waterloo to get a PhD in Civil Engineering. Researcher post doc at Aston University in Birmingam (UK). then at the Technological Institute of Georgia (USA) he worked on the numerical simulation of granular media with the discrete element method and the application from simulation results to the development of constitutive laws for these environments. Pr. Ouadfel is the author of a 2D-3D finite element code to simulate ellipsoid-shaped grains and several publications. He is also head of various modules and co-supervisor of research at the National School of Applied Sciences where he teaches since September 2001. He is also a founding member of the research team: Mathematics. Computer Science and Mechanics.

Praise Worthy Prize

International Review of Mechanical Engineering (I.RE.M.E.), Vol. 12, N. 10
ISSN 1970 - 8734
October 2018

Effects of the Variation of Organic Carbon Rate on the Biogas Production During Anaerobic Digestion

Abdelhay Laabyech[1], Samir Men-la-yakhaf[1], Fatima Kifani-Sahban[1],
Kamal Gueraoui[1,3], Imane Wahby[2]

Abstract – *In this work, in the anaerobic digestion of effluent from wastewater treatment plant (WWTP) of paper pulp mill has been studied, because they contain organic carbon. The biogas production at the WWTP of Kenitra varies from a day to another depending on the concentration of organic carbon rate present in the effluent. For that reason, the effects of the initial organic carbon contained in effluent on the biogas production during anaerobic digestion have been simulated. Therefore, the production of biogas is estimated by using different input, assuming that the initial organic carbon rate in the effluent varies from zero to 5kg/m^3 and by using the proposed approach by the mathematical model that describes the real behavior of the digesters. Results have showed that the biogas production increases as a function of carbon organic rate up to 2.5kg/m^3, then it tends to stabilize. The stabilization of biogas production observed above 2.5kg/m^3 might be correlate with reactions occurring during hydrolysis, acidogenesis and methanogenesis steps.* ***Copyright © 2018 Praise Worthy Prize S.r.l. - All rights reserved.***

Keywords: *Biogas Production, Dissolved Organic Matter, Liquid Effluent, Anaerobic Digestion, Numerical Model*

Nomenclature

θ_i	Organic carbon (kg/m^3)
θ_{aq}	Aqueous organic carbon (kg/m^3)
θ_{Ba}	Acidogenic biomass carbon (kg/m^3)
θ_{Bm}	Methanogenic biomass carbon (kg/m^3)
θ_{Ac}	Acetate carbon (kg/m^3)
θ_{CH_4}	Methane carbon (kg/m^3)
θ_{CO_2}	Carbon dioxide carbon (kg/m^3)
h_i	First-order hydrolysis rate constant of cellulose (day^{-1}), i =1, 2, 3. i=1: fast, i=2: medium and i=3: slow
Y_A	Mass of acidogenic biomass formed per mass of carbon utilized (kg/kg)
Y_M	Mass of methanogenic biomass formed per mass of acetate utilized (kg/kg)
D_A	Death rate constant for acidogenic biomass (day^{-1})
D_M	Death rate constant for methanogenic biomass (day^{-1})
H_{Sa}	Half saturation constant for acidogenic biomass (kg/m^3)
H_{Sm}	Half saturation constant for methanogenic biomass (kg/m^3)
λ_a	Maximum growth rate constant for acidogenic biomass (day^{-1})
λ_m	Maximum growth rate constant for methanogenic biomass (day^{-1})
Y_{CH_4}	Methane carbon formation yield coefficient (kg/kg)
Y_{AC}	Acetate carbon formation yield coefficient (kg/kg)

I. Introduction

The industrial sector in Morocco presents a socio-economic benefit, while biodegradable waste (liquid, solid or gaseous) from chemical industrial branches is polluting and it poses enormous ecological and environmental problems.

Indeed, paper pulp mills are part of industries that require the use of chemical substances in their process [1]. The liquid effluent discharged from these industries is loaded with various pollutants, such as organic matter [2]-[3], which requires physical, chemical and/or biological treatment before being released into the receiving environment [4]-[5].

The latter case is relative to anaerobic digestion where organic matter is converted into energy in the form of methane by bacteria in the absence of oxygen [6].

Anaerobic digestion is therefore a form of valorization of biomass, renewable energy production that can replace fossil fuels (natural gas, coal, oil), control pollution and reduce emissions [7]. The anaerobic digestion process comprises four main phases (hydrolysis, acidogenesis, acetogenesis and methanogenesis); the instability of one of these steps may easily breakdown the process [8]. In this work, the anaerobic digestion of liquid effluent from

https://doi.org/10.15866/ireme.v12i10.15399

the paper pulp mill has been studied, due to the fact that they contain organic carbon with a rate that varies from one day to another [9]. The mathematical model, developed previously (El Fadel, Findikakis and Leckie [10]; Vavilin and al., 2002 [11]; Men-La-Yakhaf and al., 2014 [12]), has been used to examine the daily biogas production for organic carbon rate up to 5 kg/m^3. The objective has been the one to examine the evolution of biogas production by the variation of the initial organic carbon rate in the liquid effluent, in order to highlight its inhibitory role on the production of intermediate products, particularly aqueous carbon, acetates, and biogas.

II. Biogas Production

II.1. Steps of Anaerobic Digestion

In presence of microorganisms under conditions of pH, temperature, humidity, agitation and in the absence of oxygen, the organic matter undergoes anaerobic digestion (AD), which comprises four biochemical fundamental steps: hydrolysis, acidogenesis, acetogenesis and methanogenesis (Fig. 1) [13].

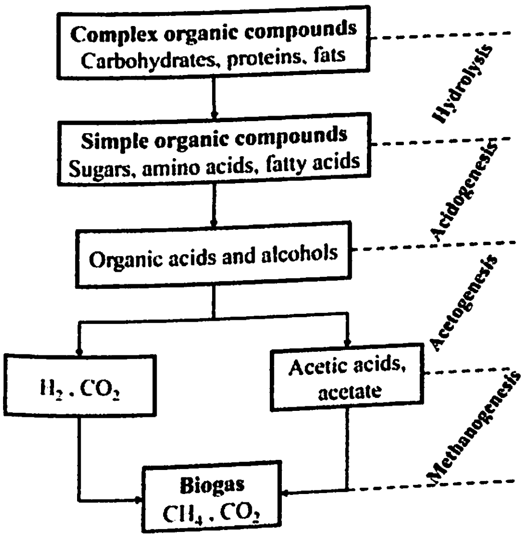

Fig. 1. The biochemical fundamental steps of AD

In the first step, the hydrolysis, complex molecules (cellulose, lipids, proteins...) are cleaved into simpler molecules (amino acids, sugars and fatty acids) [14].

Some hydrolysis products are used in the methanogenesis phase. In acidogenesis, the abovementioned products are transformed into organic acids, such as propionic acid, butyric acid, alcohols, hydrogen, carbon dioxide, water, etc. During acetogenesis, the produced compounds are degraded into acetic acid, carbon dioxide and hydrogen [14]. In the last step, the methanogenesis, acetic acid is converted into methane and carbon dioxide, and carbon dioxide and hydrogen are converted into methane by microorganisms [15]-[16].

II.2. Conditions of Anaerobic Digestion

Anaerobic digestion is a complex process that depends on several physico-chemical and biological parameters that need to be controlled, in order to provide specific conditions for the growth of microorganisms in order to ensure successful anaerobic digestion, such as : temperature, pH, agitation and concentration of volatile fatty acids.

- Temperature: in order to operate under optimal conditions, it is important to consider the type of microorganism present in the process, because the temperature affects the growth of microorganisms. Microorganisms are classified according to the range of temperature at which they can grow: Psychrophilic , with optimal growth temperatures under 10°C; Mesophilic, with growth temperatures ranging from 20 to 40°C and an optimum growth temperature at about 35°C; and Thermophilic, with optimal growth temperature above 50°C [17]-[18].
- pH: pH plays a significant role in the anaerobic digestion process. Acid-forming bacteria prefer a pH above 5.0 and methane-forming bacteria prefer a pH above 6.2. In anaerobic environment, the pH tolerance range is between 6 and 8 [19], with an optimum between 6.8 and 7.2 [17]-[18].
- Agitation: in order to improve the digestion process, the agitation of the contents of the digester is necessary because it allows to balance the distribution of the substrates in order to ensure the microorganisms contact with the substrates and also to keep a uniform temperature in the digester [18]-[20].
- Volatile fatty acid: During the anaerobic process, the production of a high concentration of volatile fatty acids during the hydrolysis and the acidogenesis steps can inhibit the methanogenesis step and methane production [21].

III. Methodology

The effect of initial organic carbon rate on the biogas production has been simulated by using the approach proposed by the mathematical model, while assuming that initial organic carbon rate varies from 0 to 5 kg/m^3.

The digester in question is a continuous one with a capacity of 1200m^3 and treats 4500m^3 of effluent per day.

The simulation results are shown in Figures 3 to 10 and their analysis is discussed in Part IV.

III.1. Model of Biogas Production

The used mathematical model is a numerical one with fundamental biochemical-physical aspects, which allows to model the production and transfers of biogas and heat in waste [10]. It is based on the use of the Monod model for microbial growth. The equations describe the ecosystem dynamics of waste degradation comprised by the hydrolysis of precursor components of biogas production, the use of aqueous carbon by acidogenic microorganisms, the birth and decomposition of acidogenic and methanogenic biomass, and finally the production of methane and carbon dioxide from acetate produced by acidogens (Fig. 2) [10]-[22], [27][28].

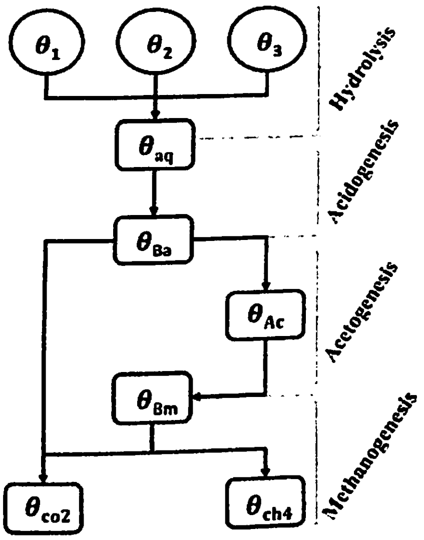

Fig. 2. Schematic diagram of the mathematical model

III.2. Equations of the Model

Organic carbon:

$$\frac{d\theta_i}{dt} = -\sum_{i=1}^{3}\left(h_i\theta_i\right) \tag{1}$$

Aqueous organic carbon:

$$\frac{d\theta_{aq}}{dt} = \sum_{i=1}^{3}\left(h_i\theta_i\right) - \left[\left(\frac{\lambda_a}{Y_A}\right)\left(\frac{\theta_{aq}}{H_{Sa}+\theta_{aq}}\right)\theta_{Ba}\right] \tag{2}$$

Acidogenic biomass carbon:

$$\frac{d\theta_{Ba}}{dt} = \left[\left(\frac{\lambda_a \cdot \theta_{aq}}{H_{Sa}+\theta_{aq}}\right) - D_a\right]\cdot\theta_{Ba} \tag{3}$$

Methanogenic biomass carbon:

$$\frac{d\theta_{Bm}}{dt} = \left[\left(\frac{\lambda_M \cdot \theta_{ac}}{H_{Sa}+\theta_{Ac}}\right) - D_m\right]\cdot\theta_{Bm} \tag{4}$$

Acetate carbon:

$$\begin{aligned}\frac{d\theta_{Ac}}{dt} = Y_{Ac}\cdot&\left[\left(1-Y_A\right)\left(\frac{\lambda_A}{Y_A}\right)\left(\frac{\theta_{aq}}{H_{Sa}+\theta_{aq}}\right)+D_a\right]\cdot\\ &\theta_{Ba} - \left[\left(\frac{\lambda_m}{Y_M}\right)\left(\frac{\theta_{Ac}}{H_{Sm}+\theta_{Ac}}\right)\right]\cdot\theta_{Bm}\end{aligned} \tag{5}$$

Methane carbon:

$$\begin{aligned}\frac{d\theta_{CH_4}}{dt} = Y_{CH_4}\cdot&\left[\left(1-Y_M\right)\left(\frac{\lambda_M}{Y_M}\right)\cdot\right.\\ &\left.\left(\frac{\theta_{Ac}}{H_{Sm}+\theta_{Ac}}\right)+D_a\right]\cdot\theta_{Bm}\end{aligned} \tag{6}$$

Carbon dioxide carbon:

$$\begin{aligned}\frac{d\theta_{CO_2}}{dt} = \left(1-Y_{Ac}\right)\cdot&\left[\left(1-Y_A\right)\left(\frac{\lambda_A}{Y_A}\right)\cdot\right.\\ &\left.\left(\frac{\theta_{aq}}{H_{Sa}+\theta_{aq}}\right)+D_a\right]\cdot\theta_{Ba}+\left(1-Y_{CH_4}\right)\cdot\\ &\left[\left(1-Y_M\right)\left(\frac{\lambda_M}{Y_M}\right)\left(\frac{\theta_{Ac}}{H_{Sm}+\theta_{Ac}}\right)\right]\cdot\theta_{Bm}\end{aligned} \tag{7}$$

III.3. Equations Usage

Eqs. (1) and (2) represent the hydrolysis of organic matter where complex molecules are cleaved into simpler one. Eqs. (3) and (4) are based on the Monod Model for Microbial Growth [22], they represent the growth and the death of acidogenic and methanogenic biomass. Eq. (5) represents the production of acetate. The obtained aqueous carbon is metabolized by the acidogenic biomass to give acetate. Eq. (6) represents the production of methane. The generated acetate is metabolized by the methanogenic biomass to produce methane. Eq. (7) represents the production of carbon dioxide. The aqueous carbon obtained is metabolized by the acidogenic biomass in order to give carbon dioxide and the acetate generated is metabolized by the methanogenic biomass in order to produce carbon dioxide.

III.4. Method of Resolution

The biogas production equations, from (1) to (7), established according to the mathematical model, do not admit analytical solutions. Hence, the use of numerical methods appears obligatory. Authors have chosen to use the Runge-Kutta second order method in order to transform the system of differential equations into a numerical model written in FORTRAN language. The simulation results, based on the mathematical model, are given in Figs. 3 to 10 [23].

IV. Results and Discussion

The plots in Fig. 3 show that during the hydrolysis step, the organic carbon rate decreases with time. During this step, literature [15]-[16] states that the macromolecules are reduced to monomers and the degradation kinetics depends on the nature of the substrate (proteins, carbohydrates, lipids). The plots in

Fig. 4 show that aqueous carbon rate, as a function of time, begins by increasing, then goes to a maximum, before decreasing. The aqueous carbon content depends on the initial organic carbon rate. Indeed, the more the organic carbon rate is high, the more aqueous carbon is obtained (Figs. 3 and 4). The decrease of aqueous carbon is explained by its transformation by microorganisms into volatile fatty acids (acetate, propionate...), alcohols, carbon dioxide and hydrogen [15]-[16]. The acetate that is produced in the acidogenesis and acetogenesis steps is shown, for each initial organic carbon rate, in Fig. 5.

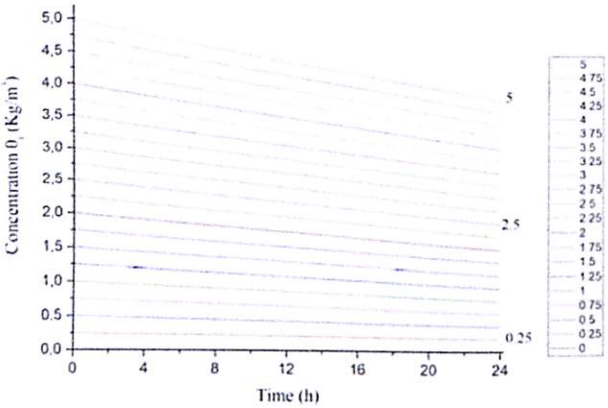

Fig. 3. Profiles of organic carbon as a function of time

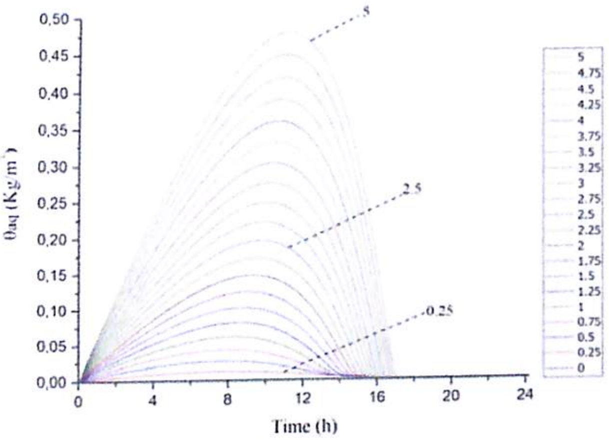

Fig. 4. Profiles of aqueous carbon as a function of time

The plots indicate that as a function of time, acetate productions initially increase and then decrease after reaching a maximum value for initial organic carbon rate below 3.75 kg/m^3. Beyond this range, acetate production, after the exponential increase between 8 and 17 hours, knows a stabilization followed by a slight decrease in production as a function of time. On the plots in Fig. 6, the stagnation phase noticed for each acetate concentration coincides with the one where acidogenic biomass carbon production (θ_{Ba}) increases linearly (this range is hatched on the graph). As the acetate production is proportional to the products of both hydrolysis/acidogenesis steps and those phases occur faster than the methanogenesis step [7], in this case a high concentration of initial organic carbon may lead to an accumulation of the products of the hydrolysis/acidogenesis steps. Then, the stagnation noticed for acetate concentrations may be due to the accumulation of the volatile fatty acid generated by hydrolysis/acidogenesis steps, and this can inhibit the anaerobic digestion process [24].

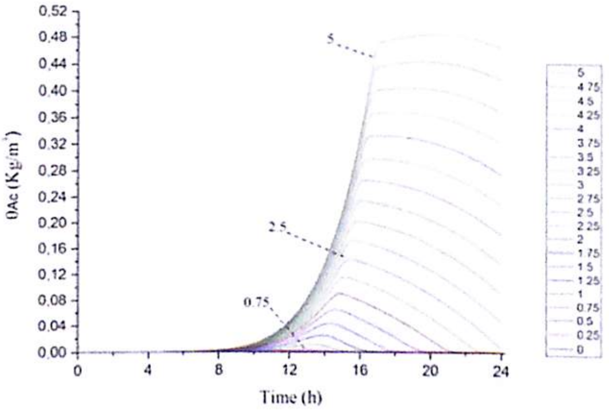

Fig. 5. Profiles of acetate content as a function of time

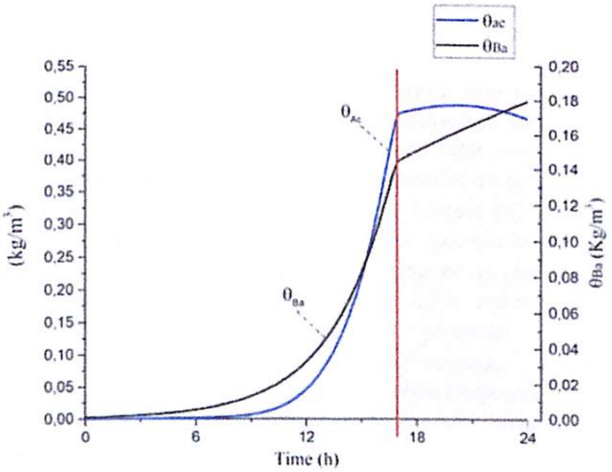

Fig. 6. Area corresponding to the stagnation of acetate for a given initial organic carbon rate

The accumulations of methane and carbon dioxide productions, from the earlier steps, for the different initial organic carbon rates are shown in Figs. 7 and 8.

The sum of methane and carbon dioxide productions represents the biogas production (Fig. 9). The plots in these figures indicate that the accumulations of these gas increase with time and also by the rise of the initial organic carbon rate in the effluents.

The biogas plot as a function of time (Fig. 9) indicates that biogas production increases as a function of organic carbon rate.

The biogas production is still low at low carbon rates and insensitive to it above 2.5 kg/m^3. This is clearly highlighted in the plot of Fig. 10. Indeed, above 2.5 kg/m^3, biogas production tends to stabilize. This may be explained by the inhibitory effect of a high concentration of the volatile fatty acid generated in acidogenesis step [7]-[21].

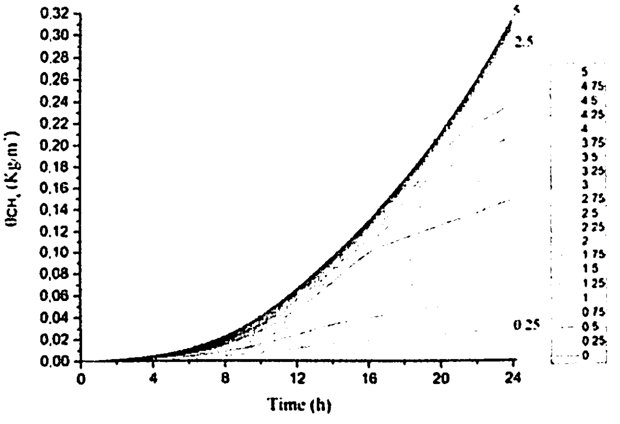

Fig. 7. Cumulative productions of methane as a function of time

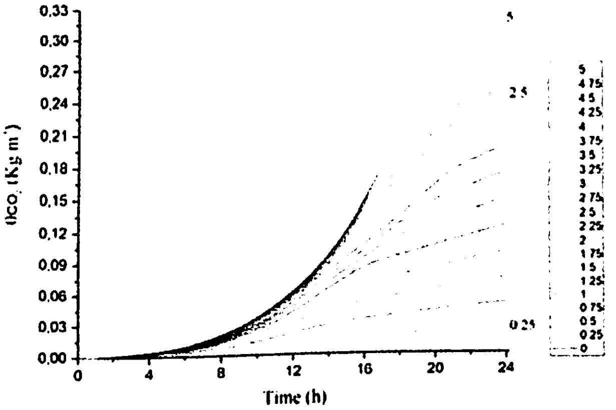

Fig. 8. Cumulative productions of carbon dioxide as a function of time

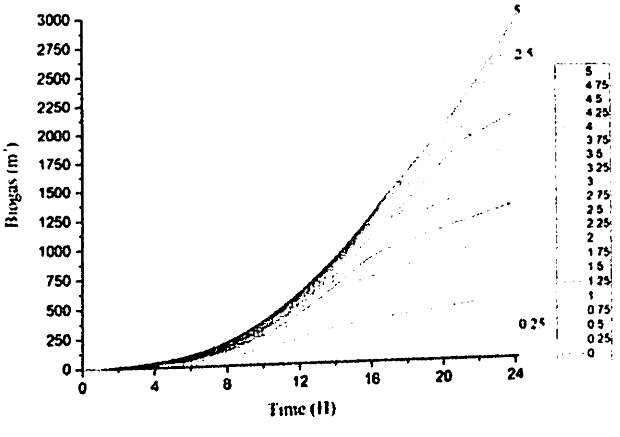

Fig. 9. Cumulative productions of biogas as a function of time

In order to overcome this disadvantage, an optimal value of the organic carbon concentration is necessary [25].

Furthermore, the results of the simulation of the biogas production (Fig. 9) agree with the experimental results of Sun, M-T et al. [26], but not in the high carbon concentrations. Indeed, in the presented simulation, biogas production stabilizes while in the work of Sun, M-T et al. [26] it falls drastically.

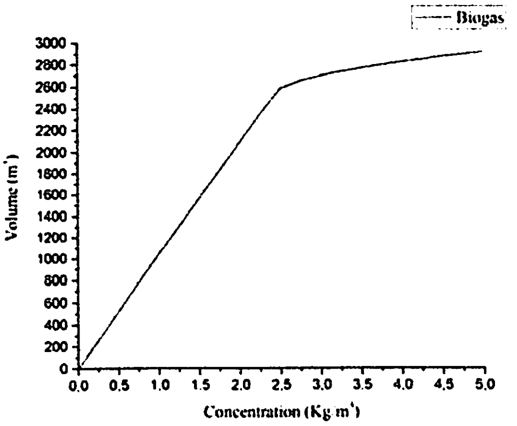

Fig. 10. Volume of biogas production as a function of organic carbon

V. Conclusion

The biogas production by anaerobic digestion of liquid effluents from the pulp and paper mill of Kenitra depends on the initial organic carbon rate present in the effluents. This dependence is highlighted by the results obtained via the approach proposed by the mathematical model and it is consistent with the experimental work in the literature. At an initial organic carbon rate variation between 0 to 5 kg/m^3, the biogas production has been very low for low initial organic carbon rates and it has stabilized above 2.5 kg/m^3. The stabilization of the accumulations of methane and carbon dioxide production is due to the inhibitory effect of the accumulation of products from the hydrolysis and acidogenesis phases. In order to overcome this disadvantage and to optimize the anaerobic digestion process to promote biogas production, an optimal initial organic carbon concentration must be chosen. This work responds to the objective set by highlighting, by numerical simulation, the effect of organic carbon concentration on biogas production.

References

[1] C. Rodriguez, A. Alaswad, Z. El-Hassan, A.G. Olabi. Mechanical pretreatment of waste paper for biogas production. *Waste Management*, Vol. 68, pp. 157-164, 2017.

[2] A. do Carmo Precci Lopes, et al., Biogas production from thermophilic anaerobic digestion of kraft pulp mill sludge, *Renewable Energy*, 2017.

[3] H. Dhar, P. Kumar, S. Kumar, S. Mukherjee, Atul N.Vaidya. Effect of organic loading rate during anaerobic digestion of municipal solid waste. *Bioresource Technology*, Vol. 217, pp. 56-61, 2016.

[4] S. Q. Aziz, H. A. Aziz, M. S. Yusoff, M. Bashir, M. Umar. Leachate characterization in semi-aerobic and anaerobic sanitary landfills: a comparative study. *Journal of Environmental Management*, Vol. 91, pp. 2608-2614, 2010.

[5] H. Vashi, O.T. Iorhemen, J.H. Tay, Aerobic granulation: A recent development on the biological treatment of pulp and paper wastewater. *Environmental Technology & Innovation*, 2017.

[6] T. Xie, S. Xie, M. Sivakumar, L.D. Nghiem, Relationship between the synergistic/antagonistic effect of anaerobic co-digestion and organic loading. *International Biodeterioration & Biodegradation*, Vol. 124, pp. 155-161, 2017.

[7] D. Li, S. Liu, L. Mi, Z. Li, Y. Yuan, Z. Yan, X. Liu, Effects of

feedstock ratio and organic loading rate on the anaerobic mesophilic co-digestion of rice straw and pig manure. *Bioresource Technology*, 2015.

[8] M. C. Nelson, M. Morrison, Z. Yu, A meta-analysis of the microbial diversity observed in anaerobic digesters, *Bioresour Techn*, Vol. 102, pp. 3730–3739, 2011.

[9] R. Toczyłowska-Mamińska, Limits and perspectives of pulp and paper industry wastewater treatment – A review, *Renewable and Sustainable Energy Reviews*. Vol. 78, pp. 764–772, 2017.

[10] M. El Fadel, A. N. Findikakis et al, Numerical Modeling of Generation and Transport of Gas and Heat in Landfills I. Model Formulation. *Waste Management and Research*, Vol. 14, pp. 483-504, 1996.

[11] V. A. Vavilin, S. V. Rytov, L. Ya. Lokshina, Distributed Model of Solid Waste Anaerobic Digestion. *Wiley periodical Incpp*, pp. 66-73, 2002.

[12] S. Men-La-Yakhaf, K. Gueraoui, M. Driouich, New numerical and mathematical code reactive mass transfer and heat storage facilities of argan waste, *Advanced Studies in Theoretical Physics*, Vol. 8, no.10, pp. 485 – 498, 2014.

[13] R. Kadam, N.L. Panwar, Recent advancement in biogas enrichment and its applications, *Renewable and Sustainable Energy Reviews*, Vol. 73, pp. 892-903, 2017.

[14] A. Reungsang, S. Sittijunda, C. Sreela-or. Methane production from acidic effluent discharged after the hydrogen fermentation of sugarcane juice using batch fermentation and UASB reactor. *Renewable Energy*, Vol. 86, pp. 1224-1231, 2016.

[15] K. F. Adekunle, J. A. Okolie, A Review of Biochemical Process of Anaerobic Digestion, *Advances in Bioscience and Biotechnology*, Vol. 6, pp. 205-212, 2015.

[16] R. Chandra, H. Takeuchi, T. Hasegawa, Methane Production from Lignocellulosic Agricultural Crop Wastes: A Review in Context to Second Generation of Biofuel Production. *Renewable and Sustainable Energy Reviews*, Vol.16, pp. 1462-1476, 2012.

[17] J. A. Ogejo, Z. Wen ,J. Ignosh, E. Bendfeldt, E. R. Collins, Biomethane technology. *Virginia Cooperative Extencion. Publication*, pp. 442–881, 2009.

[18] Yadvika, Santosh , T. R. Sreekrishnan , S. Kohli , V. Rana, Enhancement of biogas production from solid substrates using different techniques-a review. *Bioresource Technology*, Vol. 95, pp.1–10, 2004.

[19] E. Jankowska, J. Chwialkowska, M. Stodolny, P. O. -Popiel, Volatile fatty acids production during mixed culture fermentation–The impact of substrate complexity and pH, *Chemical Engineering Journal*, Vol. 326, pp. 901-910, 2017.

[20] R. Kigozi, A. Aboyade, E. Muzenda, Biogas production using the organic fraction of municipal solid waste as feedstock, *Int'l Journal of Research in Chemical, Metallurgical and Civil Engg*, Vol. 1, 2014.

[21] I. Siegert, C. Banks, The effect of volatile fatty acid additions on the anaerobic digestion of cellulose and glucose in batch reactors. *Process Biochemistry*, Vol. 40, pp. 3412–3418, 2005.

[22] J. Monod, The growth of bacterial cultures. *Annual Review of Microbiology III*, 1949.

[23] Men-la-yakhaf, S., Gueraoui, K., Maaouni, A., Driouich, M., Numerical and Mathematical Modeling of Reactive Mass Transfer and Heat Storage Installations of Argan Waste, (2014) *International Review of Mechanical Engineering (IREME)*, 8 (1), pp. 236-240.
doi: https://doi.org/10.15866/ireme.v8i1.1265

[24] S. Babel, K. Fukushi, B. Sitanrassamee. Effect of acid speciation on solid waste liquefaction in an anaerobic acid digester, *Water Res*, Vol. 38, pp. 2417-2423, 2004.

[25] M. E. Montingellia, S. Tedesco, A.G. Olabi, Biogas production from algal biomass: A review, *Renewable and Sustainable Energy Reviews*, Vol. 43, pp. 961–972, 2015.

[26] M. T. Sun, X. L. Fan, X. X. Zhao, S. F. Fu, S. He, M. R. K. Manasa, R. B. Guo, Effects of organic loading rate on biogas production from macroalgae: performance and microbial community structure, *Bioresource Technology*, 2017.

[27] Alhassan, M., Abdulmumeen, N., Garba, M., Isah, A., Full 42 Factorial Experimental Design of Biogas Production from Cow Dung, (2016) *International Review of Chemical Engineering (IRECHE)*, 8 (1), pp. 4-7.
doi:https://doi.org/10.15866/ireche.v8i1.8107

[28] Alhassan, M., Odigure, J., Evaluation of a Prototype Biodigester for the Production of Organic Fertilizer from Cow Dung, (2016) *International Review of Chemical Engineering (IRECHE)*, 8 (1), pp. 1-3.
doi:https://doi.org/10.15866/ireche.v8i1.6332

[29] Mohcine, A., Gueraoui, K., Men-la-yakhaf, S., Mathematical and Numerical Modeling of the Valorization of Household Waste in Morocco Based on the Model of Brooks, (2017) *International Review of Civil Engineering (IRECE)*, 8 (1), pp. 19-24.
doi:https://doi.org/10.15866/irece.v8i1.11046

Authors' information

[1]Team of Modeling and Simulation of Mechanical and Energetic, Physical Department, Faculty of Sciences, Mohammed V University, 4 Av IBN BATTOUTA, B.P. 1014 RP, Rabat, Morocco.

[2]Laboratory of Botanical, Mycology and Environment. Department of Biology, Faculty of Sciences, Mohammed V University, 4 Av IBN BATTOUTA, B.P. 1014 RP, Rabat, Morocco.

[3]Département de Génie Mécanique, Université d'Ottawa, Ottawa, Canada, K1N 6N5.

Abdelhay Laabyech was born in Morocco, in 1991. He received his undergraduate degree in Master in Mechanical and Energetic from Mohammed V University in 2016. Member of the research team: Modeling and Simulation of Mechanical and Energetic (MSME), Physical Department, Faculty of Sciences, Mohammed V University, 4 Av IBN BATTOUTA, B.P. 1014 RP, Rabat, Morocco.
E-mail: abdelhay.laabyech@gmail.com

Praise Worthy Prize

International Review of Mechanical Engineering (I.RE.M.E.), Vol. 12, N. 10
ISSN 1970 - 8734
October 2018

Thermal Treatment of Morocco Sugarcane Bagasse Under Inert Atmosphere

M. Mahboub[1], K. Gueraoui[1,2], M. Taibi[1,4], I. Aberdane[1],
F. Kifani-Sahban[1], S. Men-La-Yakhaf[1], M. El Marouani[3]

Abstract – *The aim of this work is to thermally characterize bagasse waste derived from sugar cane in order to highlight their energy potential. The thermal behavior of bagasse powder has been examined by: Thermogravimetric, Differential Thermal Analysis and Differential Scanning Calorimetry, under inert atmosphere and with the heating rate of 10°C/min. The dimensional variations of sugar cane in pieces at 300 °C have also been followed and the physico-chemical analyzes of raw and heat-treated samples have been performed.* ***Copyright © 2018 Praise Worthy Prize S.r.l. - All rights reserved.***

Keywords: *Bagasse Powder, Bagasse Pastilles, Thermogravimetric, Differential Thermal Analysis, Differential Scanning Calorimetry, Dimensional Variations, Pyrolysis*

Nomenclature

BSP	Bagasse Powder
BS	Bagasse
DV	Dimensional variations
BSM	Piece of bagasse
TG	Thermogravimetric
DTA	Differential thermal analysis
DSC	Differential Scanning Calorimetry
EDX	Microanalysis X
IR	Infrared radiation
BSPR	Bagasse Raw Powder
SEM	Electronic scanning microscope
ATG	Thermogravimetric analysis
DTG	Derivative mass loss
BSPT	Bagasse treated powder
BSMT	Piece of bagasse treated
BSMR	Piece of raw bagasse
JCPDS	Joint committee on Powder diffraction standards
ATR	Attenuated Total Reflectance (cm^{-1})
T	Temperature (°C)
V_0	Initial volume (mm^3)
V	Sample volume
J	Jacobian
ν	Valence vibration
δ	Vibration of deformation in the plane
γ	Vibration of deformation out of the plane
ε_1	Vector displacement the Width
ε_2	Vector displacement the Length
ε_3	Vector displacement the Thickness
T_g	Temperature of glassy transition
Exo	Exothermic
Δx	Variation following width
Δy	Variation following length
Δz	Variation following thickness
x_i / x_f	Initial width/Final width
y_i / y_f	Initial length/Final length
z_i / z_f	Initial thickness/Final thickness
C	Carbon
O	Oxygen
N	Nitrogen
H	Hydrogen
Si	Silicon
Al	Aluminum
Mg	Magnesium
K	Potassium
H(mw)	Heat Flow (mW)
d (Å)	Distance between atomic (Å)
V	Vector displacement
HV	High ventricular
LV	Left ventricular
$(\vec{i}, \vec{j}, \vec{k})$	Direct and fixed orthonormal

I. Introduction

Renewable energies are a good alternative to fossil ones. Nevertheless, the worldwide production of energy by renewable energies is not able to cover the totality of the energy needs and the recourse to fossil fuels remains consequently unavoidable [1]. For several years, Morocco has developed the valorization of renewable energies. The solar and the wind energies are more developed than the biomass one [2]. Moreover, several parks have already been equipped with the installations providing energy and they are already operational. The biomass, in particular, urban waste is developed in order to be used as biogas [3]. However, the valorization of the

https://doi.org/10.15866/ireme.v12i10.16097

organic-mass waste resulting from the sugar industries remains limited. Indeed, bagasse, which is a byproduct of the sugar extraction from sugar cane, is stored on the production sites. The production of bagasse does not stop rising because of the demand of sugar, as well as the increase of the production of sugar cane [4]. In 2011, of the 320 000 tons produced bagasse rose by [5], only 10% is valorized by combustion in the manufacturing process of sugar, the undeveloped part of bagasse is correspond to 121 GWh. Therefore, The good sense is the benefit from the bagasse stored on the production sites. This is the reason why; in this work, authors are interested, before proposing an adequate energy valorization of bagasse, to carry out a physico-chemical and thermal characterization of the bagasse. The aim of this study, mainly focuses on the area of the "Gharb" of Morocco, which has enormous fields dedicated to the planting of sugar cane [6].

II. Experimental Part

II.1. Materials

The bagasse of sugar cane comes from the city of Machraa Bel Ksiri situated in the 'Gharb' region in Morocco (Figs. 1). The bagasse is washed with distilled water, dried in at 100°C. The bagasse is then ground in a knife mill and finally sieved. The size grading to the physico-chemical and thermal characterizations is between 180 µm and 500 µm. The elementary and rough analyses are specified in Table I. The analysis EDX (paragraph 2) made on the powder and on the pieces of bagasse are in Table II.

TABLE I
ELEMENTAL ANALYSIS OF THE BAGASSE IN MOROCCO

Parameter	Size
Elemental analysis	
% C	58.14
% O	37.20
% H	3.36
% N	6,28
Approximate analysis	
% Ash	4.25
% Humidity	5.35

TABLE II
EDX QUANTIFICATION OF BSP (RAW) AND BSMT (TREATED)

		Zone 1	Zone 2	Zone 3	Zone 4
Powder	% C	62.71	70.00	61.48	52.24
	% O	22.84	27.34	13.73	20.60
	% Si	4.28	1.05	10.61	25.24
	% K	3.28	0.95	7.33	1.33
	% Al	2.28	0.65	6.85	0.58
	% Mg	-	-	-	-
Pastilles	% C	60.40	50.69	59.66	61.49
	% O	38.48	42.15	38.98	37.34
	% Si	0.21	3.34	0.47	0.77
	% K	0.32	0.62	0.42	0.18
	% Al	0.26	2.96	0.21	0.05
	% Mg	0.33	0.23	0.26	0.17

II.2. Electronic Scanning Microscope

The microscopic characterization of the bagasse extracted from sugar cane before and after heat treatment are made through scanning electron microscopy (SEM), JEOL JSM-IT100 with field coupled to the Dispersive microanalysis by Energy of X-ray (EDX or microanalysis X). The pressure inside the surrounding wall is 31 Pa (LV) and 71 Pa (HV) and the energy of electrons is 20 keV. A very fine layer of platinum, some nanometers, is put down on every sample with a metal depositor JEOL JFC-2300HR in order to avoid any effect of load. The elemental analysis of the raw and the thermally treated bagasse at 300°C are given in Table II.

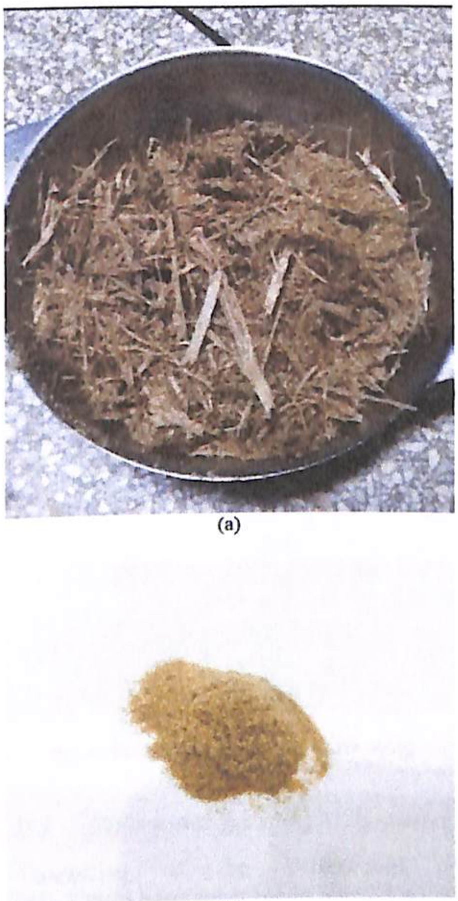

(a)

(b)

Figs. 1. Sample of the bagasse (a) at the origin and (b) in powder form after grinding

II.3. Dimensional Variations Measurements Methods

The measurements of the dimensional variations of the bagasse samples during their heat treatment have been made on pieces of length 18.5 mm, width 6 mm and of thickness 1.5 mm. The measures have been made in the main directions before and after treatment. The samples dimensions have been measured with 1/100 of precision in the principal directions before and after treatment. The essays are realized starting of the ambient temperature to the final temperature, the heating rate of 10°C/min and the flowing nitrogen of 60 cm^3/min. The total deformation corresponds to the volume variation of a material. In general, this variation can be represented by Jacobian of the transformation (noted J) [7]. Jacobian is the ratio of the sample volume (V) to the initial volume (V_0). In the mechanics of the continued mediums, Jacobian is as follows:

$$J = \frac{V}{V_0} \tag{1}$$

$$J = 1 + \operatorname{div} \vec{v} \tag{2}$$

$$J = 1 + \varepsilon_1 + \varepsilon_2 + \varepsilon_3 \tag{3}$$

where $\vec{v}$ is the vector displacement and ε_1, ε_2, and ε_3 are the deformations in the principal directions of the sample. Equation (1) leads to:

$$J = \frac{\Delta x}{x_i} \times \frac{\Delta y}{y_i} \times \frac{\Delta z}{z_i} \tag{4}$$

with:

$$\Delta x = x_f - x_i$$

$$\Delta y = y_f - y_i$$

$$\Delta z = z_f - z_i$$

The replacement of the displacement vector by its expression leads to:

$$\vec{v} = \Delta x \vec{i} + \Delta y \vec{j} + \Delta z \vec{k} \tag{5}$$

and:

$$\operatorname{div} \vec{v} = \frac{\Delta x}{x_i} + \frac{\Delta y}{y_i} + \frac{\Delta z}{z_i} \tag{6}$$

where $(\vec{i}, \vec{j}, \vec{k})$ is a direct and fixed orthonormal repository. Equations (2) and (6) lead to:

$$J = 1 + \frac{\Delta x}{x_i} + \frac{\Delta y}{y_i} + \frac{\Delta z}{z_i} \tag{7}$$

Comparing Equations (3) and (7), it is:

$$\varepsilon_1 = \frac{\Delta x}{x_i}$$

$$\varepsilon_2 = \frac{\Delta y}{y_i}$$

$$\varepsilon_3 = \frac{\Delta z}{z_i}$$

The detail and explanations of the demonstrations for the solution of Equations (1), (2) and (3) are given in [8].

II.4. Thermogravimetric and Differential Thermal Analysis

Thermogravimetric Analysis (TG) and Differential Thermal Analysis (DTA) of the bagasse powder from sugar cane were made by the type Simultaneous Thermal Analyzer 'LabsysTMEvo (1F)' and of mark SETARAM.

This device consists of a microbalance (TG) associated with a (DTA) sensor provided with a single cane, with an stove with metallic resistance being able to achieve 1600°C and of a multitasking software piloting the modules different (Fig. 2). The essays have been made starting from the ambient temperature at 600°C with the heating rate of 10°C/min under flowing nitrogen of 10 cm^3/min. The initial mass of the sample is about 6.79 mg and the particle size in the order of 1 mm.

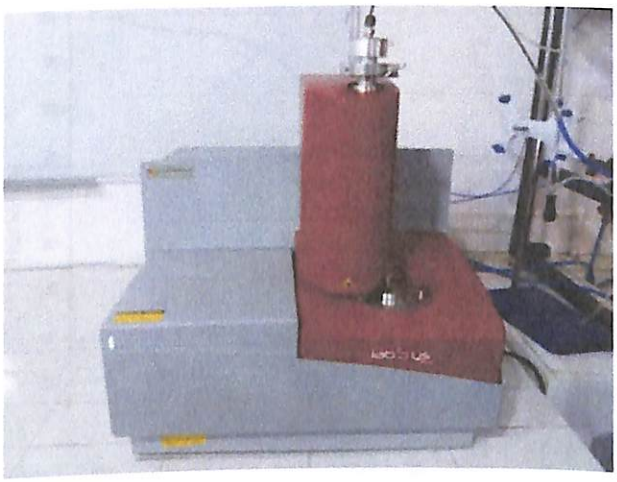

Fig. 2. Photograph of the ATG of the study

II.5. Differential Scanning Calorimetry

The measures of the Differential Scanning Calorimetry (DSC) have been made by SETARAM DSC 12. The essays have been realized under flowing nitrogen at a constant flow rate of 10 cm^3/min and at heating rate of 10°C/min. The initial mass of the sample is about 10 mg and the particle size in the order of 1 mm.

II.6. Procedures of Thermal Treatment of Fixed Bed

The thermal treatment of the bagasse of sugar cane powder and pieces has been made in a fixed bed under flowing of nitrogen of 60 cm^3/min with a heating rate of 10°C/min. In these conditions, the masses and the dimensions of samples are only known before and after the thermal request. The examined final temperatures vary between 200 to 300°C. The soaking time of the residue at this temperature of reaction has been 1 min.

The sample of the bagasse of sugar cane powder and the pieces treated thermally is respectively mentioned as

BSP and BSM. The fixed bed is a tubular furnace, Thermolyne 21100 type, used to ensure the heating of the sample in a facility consists of a quartz tube in the middle of which is placed a sample door and a thermocouple, that allows to control the temperature of the reaction. A temperature control system is connected to the thermocouple, that is placed inside the reaction tube. An alumine nacelle is used to obtain the mass of the sample (Fig. 3), after it is introduced into the oven. The temperature increases with a heating rate of 10°C/min the sample is kept at the reaction temperature for a fixed time (Fig. 4).

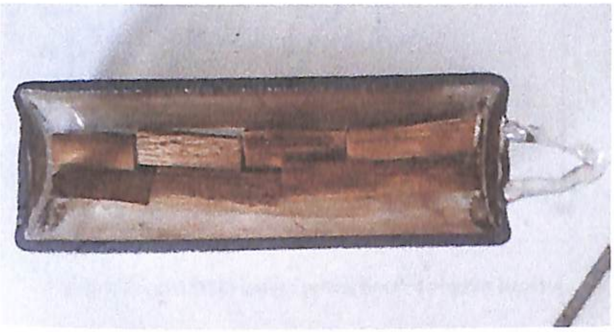

Fig. 3. Sample placed in the nacelle before treatment

Fig. 4. Picture of Thermolyne Tubular Furnace (21100 Furnace Tube)

III. Results and Discussion

This chapter presents the analysis and discussion of data gathered from the above experimental which started on 12/01/2018 and took two months.

III.1. Thermogravimetric Analysis

Fig. 5 shows mass loss (TG) and derivative mass loss (DTG) curves for sugarcane bagasse at 10°C/min under inert atmosphere. The TG curve indicates two different zones where the limit is situated in approximately of 150°C. Below this temperature, the mass loss is weak and beyond, the loss is brought up. The first zone is relative to the dehydration and the second one is relative to the proper pyrolysis. During the step of dehydration, the loss is at about 7 %. As of 150°C to 600°C, the mass loss is important and it represents 63 %. This loss is relative to the decomposition of the main constituents of the organic fraction of bagasse. This degradation is due to the volatile matter, condensed and not condensable substances. The sooty residue, obtained at 600°C represents 30 % of the initial mass of the sample [9]. The DTG curve highlights two well resolved peak and two shoulders. The first one whose maximum is situated at 70°C represents the speed of dehydration. The maximum of the second one is at 350°C preceded by two shoulders.

According to literature, the first shoulder could be generated by the decomposition of the lignin [10]. The second one, situated at 250 °C should correspond to the decomposition of hemicellulose [11] and peak should correspond to the decomposition of cellulose [12]. Other works have noted that the second shoulder could be generated by the decomposition of hemicellulose and the party of the lignin and that the peak should correspond to the decomposition of cellulose and the remaining lignin [13]. It can be noted, however, that at temperatures above 350°C, a last associated shoulder, according to Fisher et al (2003) [14], the final decomposition involves the aromatization process of lignin fraction leading to very low weight loss [15].

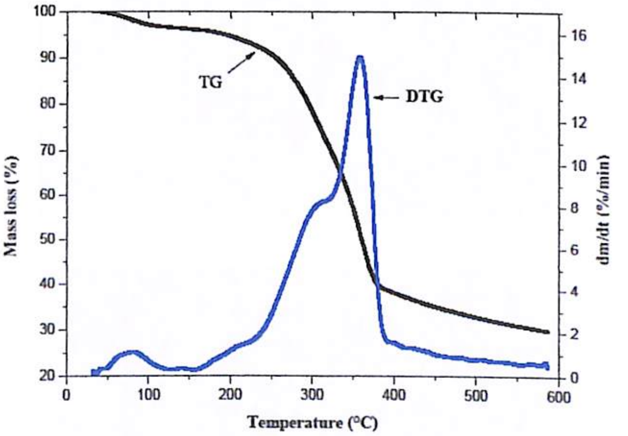

Fig. 5. TG and DTG curves gotten from of bagasse

III.2. Differential Thermal Analysis

The DTA curve of bagasse (Fig. 6) shows at first an endothermic peak followed by a maximum exothermic peak which is situated at 350°C [16]. The endothermic peak is associated to dehydratation. The DTA curve shows that the decomposition of bagasse in inert atmosphere is generally exothermic [17]. The layering of DTA and DTG curves of bagasse (Fig. 6) indicates that the maximum of the peak of DTG of bagasse coincides with the one of DTA [18], [19]. The origin of the exothermicity of the decomposition results from the training of the plastic phase amorphous as it extracted from X-ray and IR analysis [20] (paragraphs III.5 and III.6).

III.3. Differential Scanning Calorimetry

The curves in Fig. 7 concerning DSC thermogram of raw bagasse, show the existence of an endothermic peak followed by a wide exothermic one. The first one, below 160 °C corresponds to dehydratation [21]. As agreed with the DTA, DSC thermogram shows that the decomposition of bagasse of sugarcane is associated with exothermic flows of heat. This observation has been raised also by other works on the bagasse [22]. From the thermogram in Fig. 7, the temperature of glassy transition of the raw bagasse is situated at 182°C [23], [24].

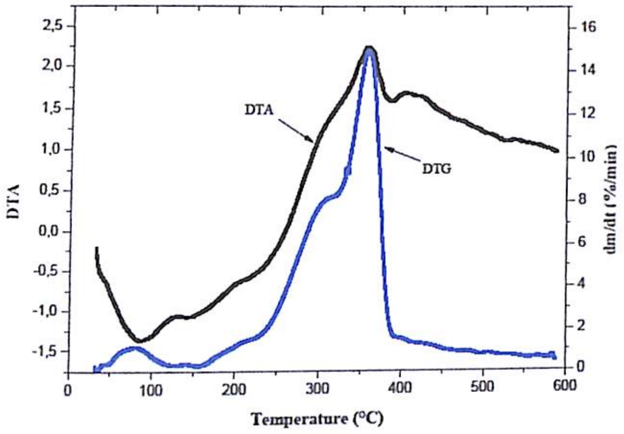

Fig. 6. DTA and DTG curves gotten from of powder bagasse

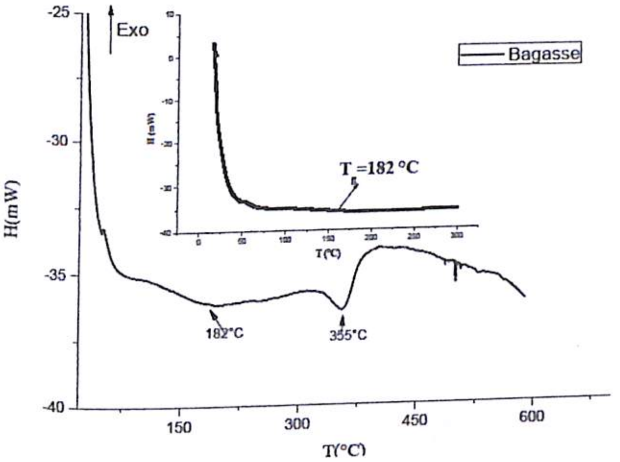

Fig. 7. DSC curves of bagasse

III.4. Dimensional Variations and Microscopic Characterization

The measurements of the dimensional variations accompanying the thermal decomposition of the bagasse and the characterization by scanning electron microscopy (SEM) are respectively given in Table III and in Figs. 8.

The measurements of the dimensional variations made on samples of bagasse at 300°C indicate that the material shrinks. The retreat is 13 and 5 % respectively in the longitudinal and transverse sense. The retreat and the formation of the plastic phase are highlighted by microscopy characterization with scanning (Figs. 8, 9).

Moreover, the comparison of fractographic taken before and after heat treatment at 300°C does not show modification of the anatomical structure of the bagasse.

Fractographic indicates that the decomposition leads to the training of an irregular porosity.

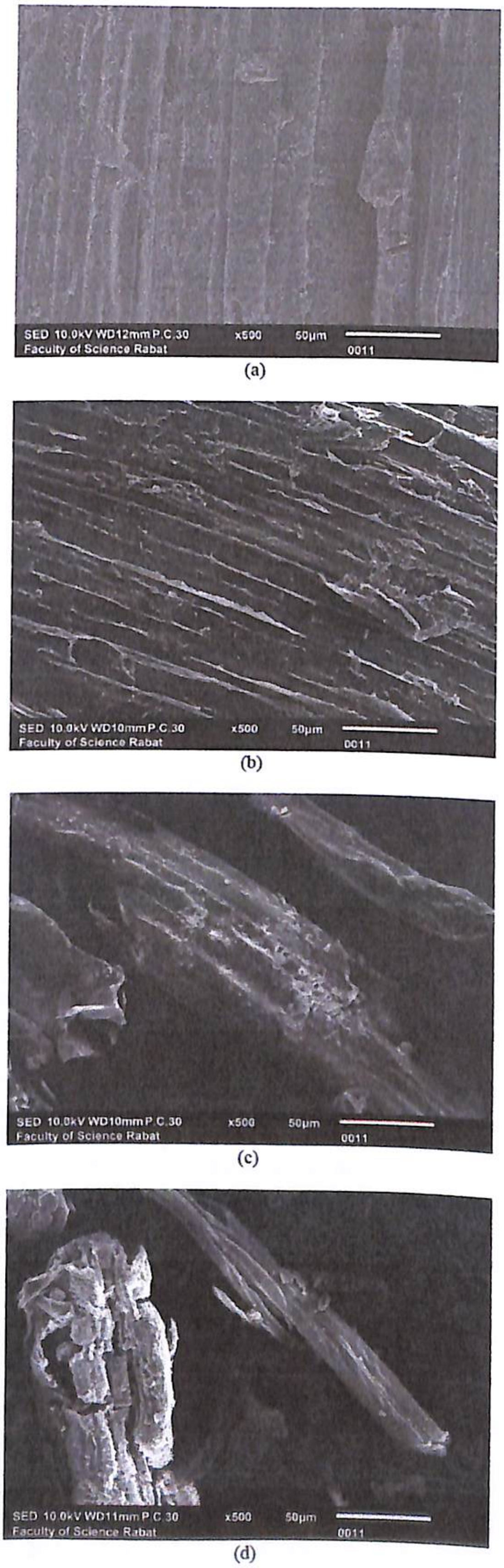

(a)

(b)

(c)

(d)

Figs. 8. Images taken by SEM of (a)-(b) samples Pastilles and (c)-(d) samples Powder, (a)-(c) raw and (b)-(d) Treated at T=300°C

Fig. 9. sample placed in the nacele after treatment

TABLE III
DIMENSIONAL VARIATIONS OF PASTILLES OF BAGASSE

		Width (mm)	Length (mm)	Thickness (mm)	J (Jacobian)
1	Before Treatment	6	18.5	1.5	0.437
	After Treatment	5	18	1	
2	Before Treatment	6	16.3	1.5	0.42
	After Treatment	5	15	1	

III.5. X-ray Diffraction Analysis

X-ray diffraction patterns of BSPR are given in Fig. 10.

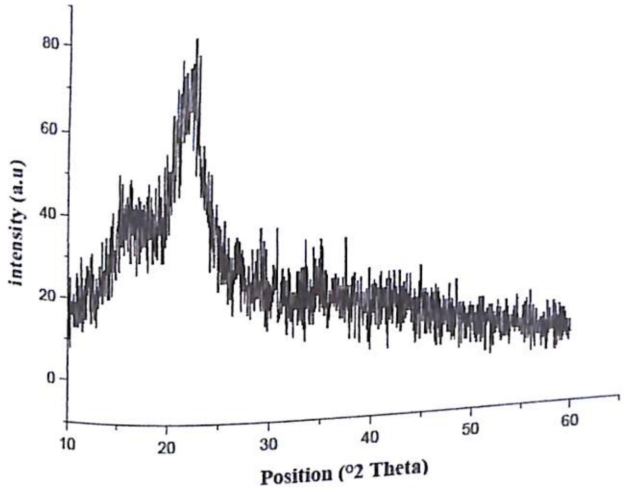

Fig. 10. X-ray patterns of the raw BSPR

The diffractogram does not exhibit a horizontal basic line. This shows that the major part of the matter is amorphous [17]. However, few diffraction peaks emerge from the basic line, indicating the presence of a small amount of crystalline matter of cellulose and hemicellulose. Table IV (Zahao and al. 2007) [25] groups the values of peak corresponding to native cellulose ($C_6 H_{12} O_6$), xylane dehydrate ($C_{10} H_{12} O_{9.2}$ H_2O) or dehydrated hemicellulose dehydrate and in the carbon. These peaks are identified in the JCPDF crystallographic data base [26]. A light travel of 2θ° towards the biggest values due to the loss of hemicellulose is noted in the diagram of BSPT (Fig. 11).

TABLE IV
BRAGG DIFFRACTION ANGLE (2θ°) AND RETICULAR DISTANCE

Position. [2θ°]	d (Å)	Corresponding compounds
18.4921	5.57122	Cel. N. et HCel
22.9887	4.49214.	Cel. N. et HCel
27.4209	3.77678	C
30.8246	3.36824	HCel
38.5353	2.71274	Cel. N. et HCel

Cel. N.: native cellulose, HCel: hemicellulose dehydrate, C: carbon

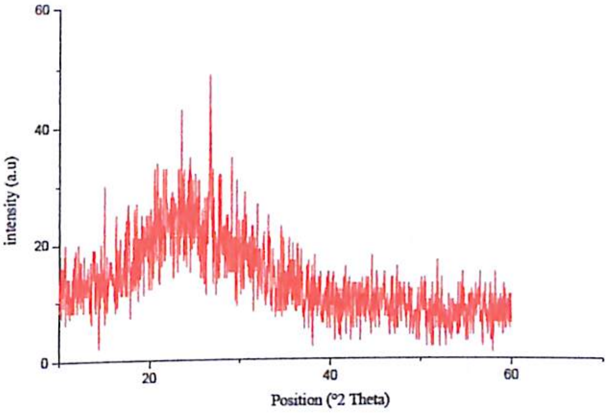

Fig. 11. X-ray patterns of the BSPT at 300°C

III.6. Infrared Analysis

III.6.1. Infrared Spectra of the Raw Bagasse of Sugarcane

Group vibrations (O-H):

The infrared spectra of the raw bagasse of sugarcane observed in Fig. 12 and Table V presents a wide and intense band centered at 3311cm^{-1}. This band corresponds to the stretching vibrations νass(O-H). The latter result from alcoholic and phenolic hydroxyl groups and aliphatic of the lignin and the polysaccharides (cellulose and hemicellulose) contained in the bagasse of sugarcane [27].

The shoulder observed at 1315 cm^{-1} is related to the vibration of deformation in plan δ(O-H) phenolic hydroxyl group [28]. The thin and the weak band at 613 cm^{-1} corresponds to the out-of-plane deformation γ(O-H) of primary and secondary aliphatic hydroxyl group and phenolic hydroxyl group [29].

Group vibrations (C-H):

The very low band observed at 3014 cm^{-1} is attributed in ν(C-H) of alkenes [30], [31]. The shoulder observed at 2916 cm^{-1} corresponds to the asymmetric vibrations of deformation in plane of νasCH3 of the aromatic methoxyl group (-O-CH3) [30], [31] and the asymmetric vibrations of deformation in plane of νasCH2 of the connection a C-H the cellulose appears in the form of fine and strong band towards 2843 cm^{-1} [32], [33]. The absorption of intensity average observed at 2078 cm^{-1} is attributed to the vibrations of symmetric strains of the groupings CH_3 and\or CH_2 (νsCH_3 et/ou νsCH_2). The C-H out-of-plane vibration (γ(C-H)) in the arocmatic pit causes the bands at 902 and 785 cm^{-1} [32], [33].

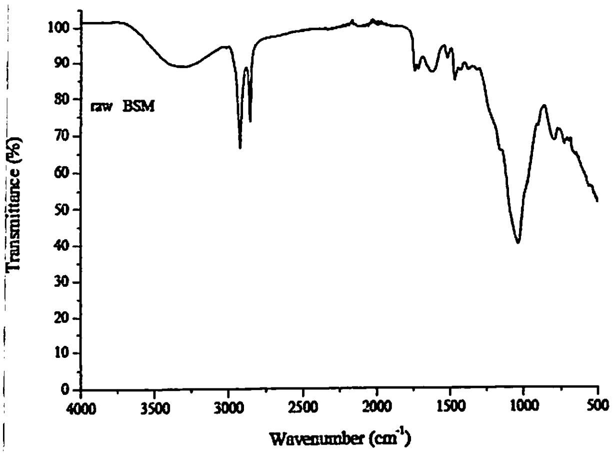

Fig. 12. Infrared spectra of raw BSM

TABLE V
FUNCTIONAL GROUPS AND CORRESPONDING BAND FREQUENCIES IN THE ATR SPECTRA OF THE RAW BAGASSE AND THE RESIDUE OBTAINED AT 300°C

ATR vibrational frequency (cm^{-1}) BSM	BSM T	*Functional groups*	
3311	-	υ(O-H) ass	
3014	-	υCH alkenes	
2916	-	$\upsilon^{as}CH_3$	υ(C-H)
2843	-	$\upsilon^{as}CH_2$	
2078	-	$\upsilon^{as}CH_3$ and/or $\upsilon^{s}CH_3$	
1740	-	υ(C=O)	
1709	1710		
1617	-	υ(C=C) aliphatic	
-	1595		
1506	-	υ(C=C) aromatic	
1457	1434		
-	1416	δ(O-H)	
1364	-	δCH_3 and / or δ(O-H)	
1315	-	δ(O-H)	
1155	-	υ(C-O)	
1038	1051		
902	-	γ(C-H)	
785	783		
613	552	γ(O-H)	

Group vibrations (C=O):

The fine and intense absorption observed at 1709 cm^{-1} is characteristic of stretching vibrations ν(C=O) of the ketones groups, carboxylic and/or esters acids of the present xylane in lignin and hemicellulose [34], [35], [36].

Stretching vibration ν(C=C) of the aliphatic and aromatic skeletal:

The stretching vibrations ν(C=C) in aliphatic chain cause the shoulder at about 1617 cm^{-1} while the skeletal ν(C=C) vibrations in aromatic ring are represented by four bands at about 1506 and 1457 cm^{-1} [37].

Stretching vibrations ν(C-O):

As for the stretching vibrations ν(C-O), their corresponding bands spread out of 1100 and 900 cm^{-1}.

The peak at 1100 cm^{-1} is assigned ν(C-O) to the secondary alcohol (-R2CH-OH) and/or aliphatic ether and primary alcohol (R-OH) [38], [39]. According to the analysis above, the main present functional groups in bagasse are aliphatic ether and cyclic, carboxyl, carbonyl and methoxyl groups, the secondary and primary aliphatic hydroxyl groups and phenolic hydroxyl groups [40]

III.6.2. Evolution Of Functional Groups During The Heat Treatment

Fig. 13 groups the infrared spectrum of raw bagasse and those treated under nitrogen at 300°C. The residue gotten is called BSMT. The infrared spectrum of BSMT, compared to the BSMR spectra, shows a bands broadening with decrease in intensity and a loss in resolution. In this temperature, only a few vibration remain. The thermal request leads to the degradation of the main constituents of raw bagasse. This degradation is translated by mass loss and it confirms the development of a plastic phase which confers on the material its amorphous character, as detected by diffraction of the X-ray and by SEM (Figs. 8, 13) [41], [42], [43].

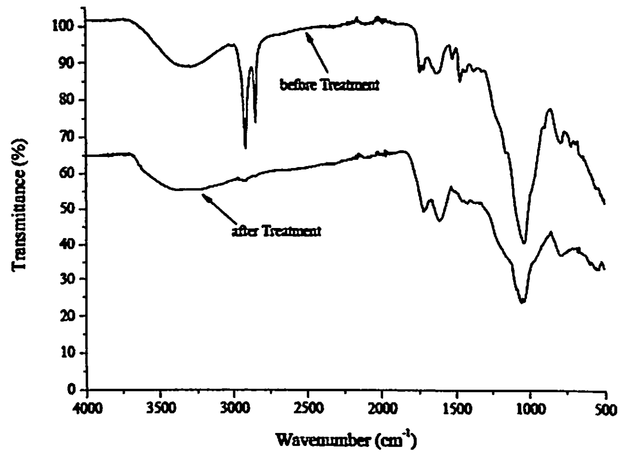

Fig. 13. Infrared spectra of raw bagasse and residue at 300°C

IV. Conclusion

The sugar cane bagasse of the Gharb of Morocco has been thermally treated under inert atmosphere of ambient temperature at 600°C. The thermal analysis indicates that the glassy transition of bagasse takes place at 182°C, that the mass loss begins at 70 °C and that the reaction is generally exothermic. The yield in char is at 30 %, the one of the condensable or non-condensable materials at 41 and 29 % respectively. The material requested thermally decreases in volume. SEM observation indicates the formation of a primary porosity in the treated material. The characterization by infrared spectroscopy highlights that bands relating to the various functional group present in the raw material undergo, once the treated material at 300°C, an extension, a decrease of their intensity and a loss of their resolution. The characterization IR and the X-ray spectroscopy (EDX) reveal that the material becomes amorphous after the heat treatment.

References

[1] M. K. Demirbas. M. F.. Balat. M.. and Balat. H. (2009). Potential contribution of biomass to the sustainable energy development. *Energy Conversion and Management* 50(7). 1746-1760.

[2] Pr. Afilal Mohamed Elamin *Potential of organic waste and energy recovery in Morocco.* The Hassan 2 Academy of Science and Technology. Ordinary Session on October 23. 2013

[3] Sarrouh. B.. Philippini. R., da Silva, S.. Lignocellulosic Bioethanol Production: Perspectives and Challenges. (2017) *International Review of Physics (IREPHY).* 11 (6). pp. 172-180.

[4] Annual Report 2015 COSUMAR Morocco. *Shared Confidence.* www.cosumar.co.ma

[5] The Minister of Agriculture. (2008) the sugar sector in Morocco. *Maghreb agriculture*, N°30. p.83.

[6] Department of Agriculture and Marine Fisheries-Strategy and Statistics Branch. (2014) *Strategic Note N°98.* Rabat. p12.

[7] F. Kifani-Sahban. A. Kifani. L. Belkbir, S. Bouhlassa, A. Zoulalian. J. Arauso and T. Cordero. Dimensional variations accompanying heat treatment of cellulose under inert atmosphere, *Thermochimica Acta* 307 (1997) 135-141.

[8] A. Kifani and F. Sahban , *Continuous Mechanics.* Publibook. Paris. France. (2014).

[9] Isa. K., Soe. M.. Rahim. M.. Abdullah. M., Ismail. K.. Ahmad, R.. Saad. S.. Characterization and Thermal Degradation of Rice Husk via TGA, (2014) *International Journal on Advanced Materials and Technologies (IREAMT).* 2 (4). pp. 102-106.

[10] J.-Y. Kim, S. Oh. H. Hwang, U.-J. Kim and J.W. Choi. Structural features and thermal degradation proprieties of various lignin macromolecules obtained from poplar wood (Populus albaglandulosa), *Polymer Degradation and stability* 98 (2013) 1671-1678.

[11] Kifani-Sahban et al.. 1996 . Study of the slow pyrolysis of Moroccan eucalyptus by thermal analysis *Thermochimica Acta*. 284 (1996). pp. 341-349

[12] Benoit Cagnon and al. 2009 .Contributions of hemicellulose. cellulose and lignin to the mass and the porous properties of chars and steam activated carbons from various lignocellulosic precursors. *Biosource Technology.* Volume 100. 292-298

[13] Fisher, T. Hajaligol. M.. Waymack, B., Kellogg. D.. 2003. Pyrolysis behavior and kinetics of biomass derived materials. *J. Anal. Pyrol.* 62. 331-349.

[14] Font. R.. Molto. J.. Galvez, A.. Rey. M. D.. 2009. Kinetic study of the pyrolysis and combustion of tomato plant. *J. Anal. Pyrol.* 85. 268-275.

[15] Saldarriaga. J., Pablos. A., Aguado. R., Amutio. M., Olazar. M.. Characterization of Lignocellulosic Biofuels by TGA. (2014) *International Review of Biophysical Chemistry (IREBIC).* 5 (4). pp. 95-98.

[16] Teixeira. J., Almeida. A.. Freitas. M.. Pilão. R., Neto. P., Pereira. I.. Ribeiro. A.. Ribeiro. A.. Pyrolysis of Cork Granules: Influence of Operating Variables on Char Yield. (2017) *International Review of Chemical Engineering (IRECHE).* 9 (1). pp. 16-22.

[17] Anil Kumar Varma. Prasenjit Mondal.. 2017. Pyrolysis of sugarcane bagasse in semi batch reactor: Effects of process parameters on product yields and characterization of products' *Industrial Crops and Products* 95. 704–717.

[18] Maiti. S., Dey, S.. Purakayastha, S.. Ghosh. B., 2006. Physical and thermochemical characterization of rice husk char as a potential biomass energy source. *Bioresour. Technol.* 97. 2065–2070.

[19] Zhutovsky. S., Kovler. K.. Chemical Shrinkage of High-Strength / High-Performance Cementitious Materials, (2018) *International* 10 (1). pp. 1-8. *Review of Chemical Engineering (IRECHE)*,

[20] J. G. Williams.. 1977. Fracture mechanics of polymers, *Polymer* vol. 17. no. 3, pp. 144–149. 1977. *Engineering & Science*,

[21] Kök, M. V., Pamir, R.. 2003. Pyrolysis kinetics of oil shales *Oil Shale* 20. 57–68. determined by DSC and TG/DTG.

[22] A. Gregorova, Application of differential scanning calorimetry to the caracterization of biopolymers. Chapter 1. *Intech.* (2013) 3-20. http://dx.doi.org/10.5772/53822.

[23] Suñol. J.. Fort. J.. Materials Developed by Mechanical Alloying and Melt Spinning. (2016) *International Review of Chemical Engineering (IRECHE).* 8 (6). pp. 121-125.

[24] Aouabdia, Y., Hamamda, S., Boubertakh. A., Precipitation Kinetics of the Hardening Phase in Two 6061 Aluminium Alloys. (2016) *International Review of Chemical Engineering (IRECHE).* 8 (4). pp. 70-75.

[25] Zhao. H., Kwak. J. H., and Wang. Y. (2007). Interactions between cellulose and N- methylmorpholine-N-oxide. *Carbohydrate Polymers* 67(1). 97-103.

[26] Aliaga. L., Alvarez. E., Bastos. I., Platt, G., Bolfarini. C., Characterization of Ni61.0Nb35.5B3.0Si0.5 Alloy in Fully Amorphous and Partially Crystallized Conditions. (2017) *International Review of Chemical Engineering (IRECHE).* 9 (3). pp. 49-54.

[27] M. Aldhure Atul V. and Ekhe J. D., Pyrolysis of purified kraft lignin in the presence of $AlCl_3$and $ZnCl_2$ *J. Environ. Chem. Eng.* 1 (2013) 844.

[28] Savy D. and Piccolo A., Physical–chemical characteristics of lignins separated from biomasses for second-generation ethanol *Biomass BioEnergy* 62 (2014) 58.

[29] Sun Y. –C., Xu J.-K., Xu F. and Sun R.-C., Efficient separation and physico-chemical characterization of lignin from eucalyptus using ionic liquid–organic solvent and alkaline ethanol solvent *Ind. Crops Prod.* 47(2013) 277.

[30] El Mansouri, N., Salvado, J., 2006. Structural characterization of technical lignins for the production of adhesives: application to lignosulfonate, kraft, soda-anthraquinone, organosolv and ethanol process lignins. *Ind. Crops Prod.* 24,8-16.

[31] Ibrahim, M, N. M., Zakaria, N., Sipaut, C. S., Sulaiman.O.. Hashim, R.. 2011. Chemical and thermal properties of lignins from oil plam biomass as a substitute for phenol in a phenol formaldehyde resin production. *Carbohydr. Polym.* 86. 112-119.

[32] Bykov.I., 2008. *Characterization of Natural and Technical Lignins Using FT-IR Spectroscopy* Masteris Thesis. Lulea University of Technology. Lulea, Sweden.

[33] Francisca Gleyciara Cavalcante Pinheiro A. Kelly Lima Soares. et al. 2017. Optimization of the acetosolv extraction of lignin from sugarcane bagasse for phenolic resin production. *Ind. Crops Prod,* Vol. 96, Feb. 2017, pp. 80-90

[34] Rodrigues Filho. G.. Monteiro. D. S., Meireles. C. D. S., Assuncao, R. M. N., Cerqueira. D; A.. Barud. H. S.. Ribeiro. S. J. L.. Messadeq. Y. (2008). Synthesis and characterization of cellulose acetate produced from recycled newspaper. *Carbohydrate Polymers*. 73. 74-82

[35] Wang Q.-B.. Zhang X.-L.. Xu D.-P. and Chen Q.-R.. Effect of Pre-oxidation on the Properties of Crushed Bituminous Coal and Activated Carbon Prepared Therefrom, *J. China Univ. Mining Technol.* 17(4) (2007) 494.

[36] Lu C.. Xu S., Wang M., Wei L., Liu S. and Liu C.. A temperature-programmed desorption and oxidation investigation of wear debris from carbon/carbon composite aircraft brakes. Carbon 45(1) (2007) 206.

[37] Pastor-Villegas J., Meneses Rodriguez J.M.. Pastor-Valle J.F.. Rouquerol J., Denoyel R. and Garcia Garcia M.. Adsorption–desorption of water vapour on chars prepared from commercial wood charcoals. in relation to their chemical composition, surface chemistry and pore structure. *J. Anal. Appl. Pyrol.* 88 (2010) 124.

[38] Saloua Sebbahi . Laila El Fakir , Soaud El Hajjaji 2015. Characterization of lignin and dervative chars by infrared spectroscopy. *Journal of Materials and Environmental Science* 6(9):2461-2468.

[39] Merad, L., Cochez. M., Jochem. F.. Ferriol, M., Bourson. P., Benyoucef. B.. Study of Reticulation RTM6 System by DSC and FTIR Spectroscopy, (2016) *International Review of Chemical Engineering (IRECHE).* 8 (6). pp. 130-135.

[40] Edalatmanesh, M., Sain. M., Liss. S.. Usage of Pulp and Paper Secondary Sludge for Biocomposite Production: FTIR and DSC Analysis. (2016) *International Review of Physics (IREPHY).* 10 (2). pp. 36-41.

[41] Sabbahi S., Ahmido A., Kifani-Sahban F., El Hajjaji S.. Zoulalian A., Preoxidation and Activation of the Lignin Char: Carbonization and Oxidation Procedures. *J. Eng.* 2014 (2014) Article ID 972897, 1.

[42] Kifani-Sahban F.. Kifani A., Belkbir L.. Zoulalian A., Arauso J., Cordero T., A physical approach in the understanding of the phenomena accompanying the thermal treatment of lignin.

Thermochim. Acta 298 (1997) 199.

[43] Yudhanto, F., Jamasri, J., Rochardjo, H., Physical and Thermal Properties of Cellulose Nanofibers (CNF) Extracted from Agave Cantala Fibers Using Chemical-Ultrasonic Treatment, (2018) *International Review of Mechanical Engineering (IREME)*, 12 (7), pp. 597-603.
doi: https://doi.org/10.15866/ireme.v12i7.14931

Authors' information

[1]Team of Modeling and Simulation in Mechanics and Energetic, Centre de l'énergie, Physical Department, Faculty of Sciences, Mohamed V University, Av Ibn Battouta, B.P. 1014, Rabat 10000, Morocco.

[2]Département de Génie Mécanique, Université d'Ottawa, Ottawa, Canada, K1N 6N5.

[3]Laboratory of Spectroscopy, Molecular Modeling, Materials, Nanomaterials, Water and Environment, (LS3MN2E-CERNE2D), Department of Chemistry, Faculty of Sciences, Mohamed V University, Av Ibn Battouta, B.P. 1014, Rabat 10000, Morocco.

[4]Laboratory of Mechanics, University Hassan II, Faculty Ain chock of Science, Casablanca, Morocco.

Moad Mahboub Born in Morocco.
Team of modelling and simulation in mechanics and energetics, Centre de l'énergie.
Member of the research team: Modelling and Simulation of Mechanical and Environment (MSME).
Faculty of sciences, Mohammed V University, Rabat-Agdal. B.P. 1014, Rabat, Morocco.
E-mail: mahb.moad@gmail.com

International Review of Mechanical Engineering (IREME)

Aims and scope

The ***International Review of Mechanical Engineering (IREME)*** is a peer-reviewed journal that publishes original theoretical and applied papers on all fields of mechanics. The topics to be covered include, but are not limited to:

inematics and dynamics of rigid bodies, vehicle system dynamics, theory of machines and mechanisms, vibration and balancing of achine parts, stability of mechanical systems, computational mechanics, advanced materials and mechanics of materials and tructures, plasticity, hydromechanics, aerodynamics, aeroelasticity, biomechanics, geomechanics, thermodynamics, heat transfer, efrigeration, fluid mechanics, energy conversion and management, micromechanics, nanomechanics, controlled mechanical ystems, robotics, mechatronics, combustion theory and modelling, turbomachinery, manufacturing processes, new technology rocesses, non-destructive tests and evaluation, new and important applications and trends.

Instructions for submitting a paper

he journal publishes invited tutorials or critical reviews; original scientific research papers (regular papers), letters to the Editor d research notes which should also be original presenting proposals for a new research, reporting on research in progress or scussing the latest scientific results in advanced fields; short communications and discussions, book reviews, reports from eetings and special issues describing research in any of the above thematic areas.
ll papers will be subjected to a fast editorial process.
y paper will be published within two months from the submitted date, if it has been accepted.

pers must be correctly formatted, in order to be published.
n ***Author guidelines*** template file can be found at the following web address:

www.praiseworthyprize.org/jsm/?journal=ireme

anuscripts should be sent on-line or via e-mail as attachment in .doc and .pdf formats to:

editorialstaff@praiseworthyprize.com

bstracting and Indexing Information:

AS Database
AB Abstracts
roQuest
ambridge Scientific Abstracts (CSA/CIG)
cademic Search Complete (EBSCO Information Services)
lsevier Bibliographic Database SCOPUS
dex Copernicus - IC Journal Master List 2017: ICV 121.78

Autorizzazione del Tribunale di Napoli n. 6 del 17/01/2007